Doctoral Dissertation

LOCAL SENSING AND IMAGING OF MAGNETIC NOISE FROM SUPERPARAMAGNETIC PARTICLES VIA DIAMOND NITROGEN-VACANCY CENTER PROBE

Thitinun Gas-osoth

Supervisor: Toshu An

Graduate School of Advanced Science and Technology
Japan Advanced Institute of Science and Technology
(Materials Science)

March, 2025

Abstract

Biological separations and various medical applications have achieved the use of magnetic particles, especially superparamagnetic particle microbeads such as magnetite (Fe_3O_4) layer covering the shell of the particle. Magnetite nanoparticles can be used to generate heat to destroy exotic cells in biomedical applications. In addition, its single magnetic domain creates varying magnetic noise in the surrounding area. Although the average field of randomly diffusing magnetic noise is zero, the magnetic noise projected vertically in both constructive and destructive directions is not completely zero in a plane layer. One of the most promising sensors to detect this magnetic noise is the nitrogen-vacancy (NV) center in diamonds, which is one of the most effective quantum sensors for magnetometry on a nanoscale scale.

In this research, we demonstrated the relaxometry imaging of a superparamagnetic core-shell particle, based on the longitudinal spin relaxation time T_1 measured at a proximal ensemble NV center in a diamond. The core-shell particle is covered by magnetite superparamagnetic materials over 200 - 300 nm thickness. The magnetic noise in GHz frequency is generated into the environment sample even without the external magnetic field. The NV spin populations reflected the unstable electron-phonon coupling, caused by the fluctuation noise in the environment, before relaxing to the thermal equilibrium of the mixed spin states. The relaxation imaging is achieved by a home-built confocal microscope which measures the fluorescence decay pixel by pixel. The different decay fluorescence is normalized revealing the contrast and mapping the relaxometry image of the magnetic noise around the core-shell particle. In the presence of the externally applied field, the magnetic field induced the magnetization of the particle along the axis of the NV. The local magnetic vector is analyzed to expose the stray field of a magnetic particle, resulting in the measurement of the magnetic B-H curve.

Finally, the discussion in this prospective research is to pave the way to develop new insight into stochastic sensing with NV centers in diamonds and broaden the horizon in biomedical, especially in NMR imaging in the future.

Keywords— relaxation time, relaxometry image, superparamagnetic, magnetic noise, magnetic fluctuation, NV center, magnetometry.

Acknowledgments

I would like to express my deepest gratitude to the wonderful people for their sacrifice and support for me. First, this endeavor would not have been possible without Assoc. Prof. Toshu An, thank you for giving me a kind recommendation and being patient throughout my doctoral course. He also provided a great opportunity and great experience to join research in his laboratory. I also benefited from the AFM experiment and the skills here under the training of Kunitaka Hayashi. He also helped me develop the relaxation imaging from a home-built confocal microscope used for this dissertation. In addition, he advised me more about laboratory safety and several mechanic skills in this laboratory. The authors thank Yifei Wang, Kasane Noda, and Takashi Kageyama for experimental support during my doctorate. I appreciated Dwi Prananto for his valuable techniques in the NV center experiments. Furthermore, I want to acknowledge Assoc. Prof. Akabori Masashi and his student members, Tauhidul Islam, Faysal Kabir for SQUID technical supports. I want to extend my thanks to Prof. Koyano Mikio and his student, Takumi Bizen for SQUID data analysis and Prof. Suzuki Toshi-kazu for recommendation on the EDS experiments. I am very grateful for the great opportunity to collaborate with Assist. Prof. Abdelghani Laraoui is a professor of the University of Nebraska-Lincoln, USA. I received many experiences with the wide-field NV center under his research conduct during 3 months of my minor research project. I also learned Python by myself while living in Nebraska. Thank you Miss Suvechha Lamichhane for Python coding and analysis. She exposed a good technique in Python line cut for a magnetic field analysis. Rupak Timalsina for taking care of me during the first week of staying in Nebraska. He helped me a lot with the preparations and discussions of the experiments. I truly appreciate one of my best Chinese friends, Tianlin Li, He always supports me in the dry transfer of tungsten disulfide, which took such a very long time for each. He allowed me to visit many places in Nebraska and Omaha visiting Warren Buffett's house. Without his support, my life in the US. would be in trouble. I want to thank Colonel Anurat Ingun, Ph.D., a former teacher who gave the best recommendation for leading the way of my life. He gave me very understandable advice and showed me "Actions Speak Louder Than Words", which has guided me to success since I was young. Thanks to Thai student fellows for their support during our studies at JAIST. Last but not least, I would like to thank the love and constant support from my family.

Contents

1 Introduction **1**
- 1.1 Background . . . 1
- 1.2 Organization . . . 3

2 Quantum Sensing of NV Center in Diamond **4**
- 2.1 Diamond Structure and Properties . . . 5
- 2.2 Optical Read Out and Spin Properties of NV Center . . . 6
  - 2.2.1 Optically Detected Magnetic Resonance (ODMR) . . . 7
  - 2.2.2 Spin Hamiltonian of Ground State NV Center . . . 9
- 2.3 Bloch Sphere . . . 14
- 2.4 Rabi Oscillation . . . 15

3 DC and AC Magnetic Sensing **18**
- 3.1 Continuous Wave ODMR . . . 18
- 3.2 Pulse ODMR . . . 19
- 3.3 Ramsey Interferometry . . . 20
- 3.4 Spin Echo and Coherence of NV Spin . . . 20
- 3.5 Noise Spectroscopy . . . 23
- 3.6 Decoherence Function . . . 24
- 3.7 Spin Relaxation Time . . . 25

4 Superparamagnetic Particles and Magnetic Fluctuation **28**
- 4.1 Néel Relaxation . . . 29
- 4.2 Relaxometry Imaging . . . 31

5 Sample Preparation and Experimental Setup **35**
- 5.1 NV Ensemble Diamond and Fabrication . . . 35
- 5.2 Superparamagnetic Core-Shell Particle . . . 37
- 5.3 Confocal Microscope . . . 39
- 5.4 Spin Relaxation Experiment and Imaging . . . 40

6 Relaxation Image of Conducting Magnetite Layer on a Superparamagnetic Core-Shell Particle 44
6.1 Experiment . . . 44
6.2 Results and Discussion . . . 46
6.2.1 Spin Relaxation affected by superparamagnetic core-shell particle . . . 46
6.2.2 Magnetic Stray Field Mapping of Superparamagnetic Core-Shell Particle . . . 50
6.2.3 The Magnetic Fluctuation Model in Ensemble NV Center in Diamond . . . 53
6.3 Conclusion . . . 56

7 Summary and Future Works 57
7.1 Summary . . . 57
7.2 Future Works . . . 58

A Magnetic Property of The Magnetic Particle 59
A.1 Magnetization Curve . . . 59
A.2 Temperature-Dependent Magnetization . . . 60

B SEM and EDS Results 62

C The Local Strain in The Diamond Chip 68

D Photoluminescence Quenching of The Superparamagnetic Core-shell Particles 70

E Particle Size Estimation 72

F NV-NV Interaction 74
F.1 NV Mesh Patterned Diamond . . . 74
F.2 Characteristic of Ensemble NV Diamond Probe . . . 74
F.3 NV-NV Interaction Results . . . 75

G NV-P1 Center Interaction 79
G.1 Nitrogen defect: P1 Center . . . 79
G.2 Double Electron-Electron Resonance . . . 79
G.3 Experimental Results . . . 80

H Widefield Nitrogen-Vacancy Magnetometry for The Magnetic B-H curve of The 2D Materials Estimation 82
H.1 Widefield Nitrogen-Vacancy Spectroscopy . . . 83

H.2 Widefield NV Image Processing 84
H.3 Magnetic Stray Field and The Magnetic field B-H curve of WS_2 86

I Instrument List **87**

List of Figures

2.1 Diamond structure with four possible orientations of NV centers in diamond. The blackball represents a carbon atom, the yellow one is a nitrogen atom and the white one is a vacancy. . 5

2.2 (a) Vibrational energy structure of NV center with photoluminescence transition absorption and emission. (b) Absorption and emission spectra with the photon side band and zero phonon line of NV^0 and NV^-. ((a) adapted from A. Alkauskas et al., [17] and (b) adapted from V. M. Acosta thesis [18]). . . 6

2.3 Schematic of the NV^- energy level. The illumination of a green laser with $\lambda = 532$ nm promotes the electron population from the ground state into the excited state. The electron-phonon coupling (zigzag line) relaxes to the lowest vibrational level of the excited state by the non-radiation process before returning to the ground state $m_s = 0$ and radiating a lower energy photon of 637 nm (red light). Meanwhile, the $m_s = \pm 1$ population mostly decays via a non-radiation through the metastable state by changing spin to $m_s = 0$, resulting in diminished fluorescence intensity. (b) dips of fluorescence intensity corresponding to ZFS of excited state and ground states of the NV structure. 7

2.4 (a) Diagram of a simple ODMR setup and a diamond sample on the XYZ piezo stage. (b) The fluorescence image of a single NV center in an electronic grade diamond. 8

2.5 (a) The pulse sequence of time-resolved fluorescence spin dependence. (b) Time-resolved fluorescence of a single NV between two initial states measured during 1 μs laser pulse. (c) The different fluorescent intensity between two states, $m_s = 0$ and $m_s = -1$, indicates fluorescence contrast and equilibrium state after 0.50 μs. 9

2.6 (a) The continuous laser and MW excitation in the CW-ODMR experiment. (b) Fluorescence spectrum of a single NV center from ODMR experiment as the function of microwave frequency. The result depicted that the fluorescence intensity reduces at the transition frequency of the $m_s = -1$ and $m_s = +1$ separated by the Zeeman energy. (c) Fluorescence spectrum from ensemble NV center when the magnetic field is applied along one of the NV axes. 11
2.7 (a) The C_3v symmetry model of the NV center with an external magnetic vector with θ angle respect to the NV axis. (b) The simulation of Zeeman splitting compared with the ODMR experimental result by varying the magnetic field at $\theta = 74 \pm 1^{\circ}$. 12
2.8 The Fluorescence spectrum as a function of microwave frequency recorded from CW-ODMR experiment. (a) Without a magnetic field applied, ($B_{app} = 0$), fluorescence drops at the transition frequency, 2.87 GHz when the electrons transition to $m_s = \pm 1$ sublevels. (b) In the presence of a magnetic field, the magnetic vector projection angle is $\theta = 74 \pm 1^{\circ}$ with various magnitudes. The $m_s = -1$ and $m_s = +1$ are separated because of the Zeeman effect. 13
2.9 (a) The PL intensity and (b) the effective lifetime as a function of B with different angles. (adapted from J.-P. Tetienne et al[46]). 14
2.10 The Bloch sphere geometrically represents the Bloch vector of spin state lie on the equator of the sphere corresponding to the rotation and phase angle. The superposition states ($\theta = \pi/2$) are located in both x- and y-axis depending on the angle φ. . 15
2.11 Rabi Oscillation protocol. (a) The pulse sequence for the Rabi experiment. The 3 μs green laser initializes the spin state to polarize at $m_s = |0\rangle$. Before starting the microwave, the delay time can be around a hundred ns up to several μs to ensure that the majority population will become polarized. Subsequently, a resonant microwave pulse with a varied duration (τ) starts continuously. The 300 ns width photon counter can be read at the initial state as the reference, and the signal's counter also starts with a read-out laser pulse to reflect the residual probability of $m_s = |0\rangle$ state. (b) The Bloch vector of the spin state rotates after $\omega_R \cdot \tau = \pi/2$ and π pulses for the superposition and $m_s = |1\rangle$ states, respectively. (c) The Rabi oscillation result measured on a single NV center, corresponding to (b) 17

3.1 (a) The Ramsey pulse sequence. (b) The Ramsey fringes are depicted by the fluorescence intensity plotting with free evolution time. The FID is proportional to the exponential decay as the function of the electron spin precession (adapted from E. O. Schafer-Nolte [67]). (c) The geometrical dynamic of Ramsey interferometry in Bloch sphere. The phase accumulation, φ, is pick up during the free evolution time, τ. 21
3.2 (a) The spin echo pulse sequence improved from Ramsey protocol by adding a π-pulse in the middle. (b) Spin echo result from an NV ensemble diamond under the magnetic field $B_{NV} \approx 31$ mT along one of NV axes. The data is fit by Eq. 3.4, reveals the periodic revival corresponding to Larmor frequency of ^{13}C nuclear spin and coherent time T_2. (c) Bloch sphere demonstrated each step of spin echo. 22
3.3 Power spectral density at different autocorrelation time for example, magnetization autocorrelation time from Néel relaxation τ_N and filter functions of Spin Echo and T_1 relaxometry protocols. (Adapted from E. Schäfer-Nolte [76]). 24
3.4 (a) The $T1$ relaxation sequence once a laser is started to polarize the NV spin to the excited state then turned off and wait by varying the dark time τ. Without a π-pulse, the relaxation time is detected from the excited state, on the other hand, a π-pulse is applied to measure T_1 relaxation from the ground state. (b) The Bloch sphere demonstrates the vector of T_1 relaxation decays respected to different initial states along the longitudinal axis (c) The T_1 relaxation result of an ensemble NV diamond as a function of time-varying and fit by $Ae^{-(\tau/T_1)^n} + B$. 26

4.1 The hysteresis of the magnetic materials. Superparamagnetic properties can be saturated as well as ferromagnetic materials but, do not exhibit coercivity and remanent magnetization after demagnetization. (adapted from A. Ven al ainen [99]). . 29
4.2 (a) Schematic representation of the coercivity-particle relations. The single-domain magnetic particles exhibit the superparamagnetic property with zero coercivity after removing the magnetic excitation. (adapted from A. Akbarzadeh et al, [89]). (b) The Néel relaxation mechanism - the magnetic moment orientation rotates inside the particle core along the easy axis (dash line) and causes magnetic fluctuation during domain flipping. 30

4.3 (a) The experimental setup with AFM cantilever and Fe_3O_4 particles while engaging to a shallow NV diamond. (b) the pulse sequence for T_1 relaxometry imaging. (c)-(e) Relaxometry images result by fixing each dark time τ. (f)-(h) Simulated imaging respected to (c)-(e), respectively. (adapted from D. Schmid-Lorch et al. [107]) 32
4.4 (a) The AFM topography image of aggregates of maghemite nanoparticles on a glass coverslip. (b) Relaxometry image corresponding to the different wait times τ. (c) ODMR spectrum at three different positions related to the markers in (a). (d) T_1 relaxation curves corresponding to the positions in (a). (d) AFM probe with nano ensemble NV diamond used to measure T_1 relaxation image. (adapted from J.-P. Tetienne et al. [104]) 33
4.5 (a) Molecular structure of Cyt-C protein. (b) NV defect structure in the diamond lattice was used to measure the relaxation rate. (c) The experimental setup of widefield NV relaxation imaging. (d) A schematic of the common-mode rejection pulse sequence of T_1 relaxation imaging. The contrast relaxation T_1 = ($T_{1,0}$ - $T_{1,\pi}$)/($T_{1,0}$ + $T_{1,\pi}$). (e) Relaxation curve from a bare diamond (black filled circles) and decay with Cyt-C solution on a diamond (open red circles). (adapted from Suvechhya et al. [109]) 34

5.1 Schematic of nitrogen implantation and annealing to form the Nitrogen-vacancy defect in a diamond. 36
5.2 (a) Electronic grade diamond was cut with triangular prism shape and cleaned by acetone in this experiment. (b) The top side presents one triangular-shaped diamond. (c) One triangular-shaped diamond is presented by the bottom side which is determined as the NV layer side. 36
5.3 (Left) Nitrogen ion distribution in atoms per cm^3 as a function of implantation depth. (Right) Vacancy distribution calculated from the carbon recoils as a function of implantation depth. 37
5.4 (a) TEM image of a cross-section of a Magnosphere superparamagnetic particle which consists of core particle, magnetic layer from Fe_3O_4, and a thin polymer layer. (b) SEM image shows Magnosphere aggregate with uniform size. (c) Schematic 3D model of Magnosphere superparamagnetic particle. (adapted from https://www.jsrlifesciences.com/en/research-reagents-ivd/magnosphere) 38

5.5 (a) Optical image of core shell magnetic particles after dropping on the glass slide. The particle size is estimated with some particle examples before selection. (b) 3 particles were picked up and placed on the NV layer side of the ensemble diamond sample. (c) The diamond sample with 3 particles flipping upside down and the optical image exposed 3 particles under the NV layer of the diamond sample while focusing downward. 38
5.6 The Schematic of PCB microstrip line with the location of the diamond sample and its 45 ° angle. 39
5.7 Experimental setup of a home-built confocal microscope. . . . 40
5.8 Photograph of (a) the Optical system of the confocal microscope. (b) the scanning confocal microscope. 41
5.9 The scanning confocal microscope measurement by focusing at each position and reconstructing the spin relaxation image. The neodymium magnet (Nd magnet) is aligned along the NV axis to make a parallel field in the ESR experiment. 42
5.10 Photograph of (a) microstrip line design diagram. (b) experiment at the scanning confocal microscope with a uniform external magnetic field from Nd magnet. 43

6.1 The cartoon demonstrates a core-shell particle is picked up by a sharpened tungsten wire and placed on the diamond by the NV layer side. A sharpened tungsten wire can be inserted under the diamond sample then flip the diamond upside down. 45
6.2 (a) The optical image shows two particles under the diamond sample in the black color. (b) After the correct focus, another particle is revealed. (c) The green laser was positioned at the center of the particle before the experiment started. 45
6.3 (a) The fluorescence intensity recorded when the pinhole focusing under the diamond sample. The fluorescence emitting from the core-shell particles can be observed. (b) After the focus adjustment, the fluorescence of ensemble NV and core-shell particle was recorded. 46
6.4 (a) T_1 relaxation time recorded between three positions are compared. The solid lines fit the exponential function of relaxation decay time. (b) The different fluorescence intensity from (a). The maximum contrast is $\tau \sim 200$ μs. 47

6.5 (a) The fixed pulse sequence utilized to measure the fluorescence decays respected to the maximum contrast in Fig. 6.4(b). (b) The fluorescence emits from the target core-shell particle. (c) The T_1 contrast image corresponded to the fluorescence image(b). 48
6.6 (a) Relaxation image with a red dashed line for marking the line cut of measurement along the horizontal axis. The red, green, and blue markers represent the NV area, border of contrast, and center positions of measurement from Fig. 6.4(a), respectively. (b) Line-cut profile of the fluorescence contrast of T_1 measurement respected to (a). (c) T_1 relaxation time recorded along the line-cut respected to (a). 48
6.7 (a) A schematic drawing of the applied static field for the local B-H curve measurement. (b) ODMR spectrum was measured outside the particle (yellow circle denoted as the particle in the inset), denoted as NV area (cross mark in the inset). (c) The T_1 contrast image with the color circles corresponding to the measurement positions. 50
6.8 ODMR with frequency dependent-mapping . (a) The mapping image at the microwave frequency of 2.708 GHz is the most splitting corresponding to the left side of the particle. (b) The mapping image at the microwave frequency of 2.748 GHz with a small contrast at the center. (c) The mapping with 2.776 GHz reveals the right side of the particle with the most reverse stray field which reduces the Zeeman splitting. 51
6.9 (a) The ODMR with Zeeman splitting results measured at a different position of the particle, left side (red), center (green), and right side (blue). (b) The ODMR results at the specific range of microwave, corresponding to the yellow shade in (a), shows the different frequency splitting agree with the position of left side, center, and right side of the particle, (color-mark in the inset) respectively. (c) The ΔB dependence in the external applied field B_{ex} measured at the left side of the particle. The linear fitting reveals the slope which implies the magnetic B-H curve of the particle. (d) The schematic illustrates the magnetic local field under the static magnetic field at a different position of particle based on ODMR results. 52

6.10 (a) Determination of particles distribute the magnetic fluctuation to a single NV in 8 directions. The center particle is the nearest particle at the center position. (b) Laser intensity after objective lens which is approximated by the Gaussian distribution plot. (c) 2D modeling of magnetic fluctuation of each single NV. The population for the average relaxation time is related to the laser intensity. 54
6.11 (a) A simulation of $\sqrt{\langle B_{\perp}^2 \rangle}$ measured by a signle NV as a function of distance x. By varying distance of NV to the particles. (b) Position-dependent of T_1 relaxation time corresponding to (a). (c) The $\sqrt{\langle B_{\perp}^2 \rangle}$ contributions in 1 line and 4 lines for 1^{st} layer as shown in Fig. 6.10(a) as a function of distance from the center position. (d) The estimated T_1 relaxation time for single and ensemble NV condition with an increasing number of contributed layer. 55

A.1 (a) M-H Curve from -0.5 T to 0.5 T (a) at 300 K and (b) comparison of at 5 K and 300 K. 60
A.2 (a) The zero-field cooled (ZFC) and field-cooled (FC) magnetization curves. 61

B.1 (a) The backscattered electron image and (b) the secondary electron image of the magnetic beads with incident electron energy at 15 KeV. 63
B.2 The SEM image with positional EDS of the magnetic particles at 12000X. 63
B.3 EDS pattern of magnetic beads with different positions. 64
B.4 The EDS elemental mapping images of magnetic beads for C, O, Fe, Si, Pt, and Pd. 66
B.5 (a) The EDS line spectrum across a magnetic bead. (b) The EDS line spectra of C, Si, and O. (c) The EDS line spectra of Fe, Al, Pt, and Pd. 67

C.1 ODMR spectra in the absence of a magnetic field with different microwave power dependents (a) at 30 dBm, (b) at 25 dBm, (c) at 20 dBm, and (d) at 15 dBm, respectively. The local strain was revealed at the minimum microwave power in (d). . 69

D.1 (a) Optical image of the magnetic particles, and (b) the PL image emitted from the magnetic particles. 71

D.2 (a) The PL quenching at the particle at position No. 1 with the maximum time scale of 1 second. (b) The PL quenching at the particle at position No. 1 with the maximum time scale of 10 seconds. (c)-(d) The PL intensity image of the magnetic particles before and after laser excitation, respectively. 71

F.1 Schematic of the NV mesh patterned diamond fabrication. (a) The electronic-grade diamond is covered by a copper grid mask and then implanted with nitrogen ions. (b) After the implantation process, the diamond sample was annealed to form the vacancy lattice. (c) Schematic illustrates the NV scanning probe on the NV mash target. 75

F.2 (a) SEM image of the NV probe after FIB milling process (top view). The diameter of the NV tip is estimated at 1 μm and 4 μm long. (b) SEM image captured from the side view of the NV probe. (c) The tungsten wire with a diameter of 30 μm and around 500 μm long is attached to the tuning fork and the NV probe at the end. 76

F.3 (a) The fluorescence intensity measured from the NV tip which was estimated at 1 μm diameter. (b) The ESR spectrum was measured at the tip to confirm that the NV defects were located at the tip of the NV probe. 76

F.4 Schematic of the NV-NV interaction experiment. (a) The NV probe is scanning on the NV mesh patterned diamond as the NV target under the magnetic field bias. (b) The experimental result was extracted from the fluorescence intensity through the NV probe. The bright areas were NV centers from nitrogen implantation through the copper grid mask. 77

F.5 (Upper) The scanning area by the recording of fluorescence intensity of 25×5 μm^2. The cartoon shows the NV probe position at the edge of the NV pattern. (Lower) The Zeeman splitting is measured as the function of varying external magnetic fields. The dashed line is marked at 7.2 mT which used to measure the NV$-$NV interaction between the NV probe and the NV target. 77

F.6 (a) The electrons in the NV probe are excited by the Spin echo sequence from MW1. Meanwhile, the electrons on the target diamond are excited by a π-pulse from MW2. The result signal and reference are observed during read-out (b) The result from the DEER experiment was compared with the spin echo. The shorten coherent time was expected from the dipole-dipole coupling between the probe and target spins. 78

G.1 Bloch sphere describes DEER experiment. When the second microwave frequency corresponding to the P1 Center is applied, the defect spins flip and the total magnetic field is changed, which cause the fluorescence drop in the NV spins. . 80
G.2 The fluorescence image of the NV mesh patterned diamond. the bright area corresponds to the copper mask during nitrogen implantation. 81
G.3 (a) Rabi oscillation measured in the NV mesh area. The microwave power of 39 dBm was applied. The π-pulse of 48 ns is obtained and used to excite spin echo experiment. (b) Spin echo with ^{13}C nuclear spin oscillation. 81
G.4 (a) The microwave pulse sequence in DEER experiment. The microwave frequency is swept to match the P1 center resonance frequency. (b) The fluorescence intensity as a function of frequency which shows the P1 spin induces the magnetic noise to the NV spins, causing the fluorescence to decrease. . . 81

H.1 (a) The ODMR experiment setup with widefield NV spectroscope. The external magnetic field from the magnets is parallel to one of the NV axes by the in-plane of the (110) diamond. (b) The NV energy levels when excited by a green laser. (c) The ODMR dips corresponding to the NV spin transition frequencies of f_- and f_+ due to 186 mT of B_{app}. 84
H.2 (a) illustration the recording of each frequency from each side of the Zeeman splitting by 16 values. (b) The acquisition of fluorescence images for 32 frequencies covered the transition frequencies of the NV spin in the diamond sample. 85

H.3 (a) illustration the recording of each frequency from each side of the Zeeman splitting by 16 values. (b) The magnetic images and the white rectangular are the line cut measurement areas used to extract the ΔB of each B_{app}. (c), (d) The ΔB as a function B_{app}. The linear fitting of each area indicated the paramagnetic properties of WS_2 (e) The results of the average line cut were fit by the Gaussian fitting after measuring the ΔB for both areas. 86

Chapter 1

Introduction

1.1 Background

Superparamagnetic particles play a crucial role in the key components for innovative achievement in cancer treatment, known as magnetic hyperthermia. The single domain in the superparamagnetic particles exhibits other different behaviors from the bulk materials for example, the weak of remanent magnetization in the absence of an external magnetic field and the heat generation during applying the AC magnetic fields, where the goal is to destroy the cancer at the target cells. The superparamagnetic particles are associated with the biomedical technique for bioseparation. The superparamagnetic beads represent a sophisticated technique for the specificity of antigen-antibody combination[1,2], called immunoassays with magnetic separations.

Once the target molecules attract the superparamagnetic beads, the external magnetic field is applied to separate them from the other the rest of the materials before transferring the supernatant part to the other. This process can be repeated until the materials have much more purification.[3] The superparamagnetic nanoparticles exhibit strong magnetization under magnetic bias but become almost zero magnetization when the field is removed. This behavior allows for interesting applications in complex molecular biological science.

The important property behind superparamagnetism is that it improves the magnetic contrast in biomedical imaging, such as magnetic resonance imaging (MRI). The nanoparticles enable the high sensitivity of electron spin and relaxation time images. This is due to the magnetic noise which refers to the random fluctuations in the magnetic field generated in the superparamagnetic particles even without imposing of an external magnetic field.[4]

Magnetic noise detection has new opportunities for this fantastic property due to the combination of superparamagnetic particles and quantum sensing, especially through the nitrogen-vacancy (NV) centers in diamonds. Because of the atomic scale point defect in the diamond crystals, magnetic sensing is extremely sensitive to small magnetic fields for a specific point of interest, making it perfect for mapping and identifying magnetic noise in the nanoscale. With the outstanding sensitivity and spatial resolution provided by quantum sensing in diamonds, a magnetic field generated by a single domain of superparamagnetic particles or even a small magnetic source can be detected. This feature is particularly beneficial in applications where high-resolution magnetic sensing and mapping are fundamental, including nanoscale magnetic imaging. These systems are developed more effectively including superparamagnetic integration, which will enable more precise as well as measurement of magnetic noise that was previously challenging to observe.

Furthermore, the utilization of superparamagnetic particles as the molecular separation through the precise tracking of the movement of superparamagnetic nanoparticles, will allow us to investigate the nuclear magnetic resonance (NMR) in specific target elements. Because of high magnetization during external magnetic bias, the total magnetic field will be increased resulting in a higher frequency of nuclear spins. This novelty is undiscovered even mentioned in any applications. In addition to this research, we will enhance new insights into biological processes and facilitate more effective high-performance instrumentation in the future by opening up new avenues for research and innovation in biophysics and materials science.

This dissertation is aimed at relaxation imaging of the local magnetic noise produced by a superparamagnetic core-shell particle using NV centers in diamonds. This research is expected to discover the analysis technique for relaxation time by interacting with fluctuating magnetic noise in the environment under ambient conditions with prospects for paving the way to a cutting-edge advancement in exploring fundamental physics at the nanoscale.

1.2 Organization

This dissertation consists of seven chapters based on the basic background and concept of NV centers in diamonds.

Chapter 2 refers to Quantum sensing phenomena via defect points in diamonds including structure and properties, which are described by NV energy levels. The optical properties and investigation technique of ODMR. This chapter covers the introduction of the Bloch sphere which is used to describe the spin projection of electron spins. The superposition state is demonstrated by Rabi oscillation measured with a microwave pulse sequence.

Chapter 3 mentions the DC and AC magnetic sensing in NV centers. The concepts of ODMR with microwave pulse techniques to detect the DC and AC fields. Introduction to noise spectroscopy which interacts with the NV spins and causes the relaxation time.

Chapter 4 describes the basics of superparamagnetic particles and the source of magnetic fluctuation. The relaxation of a single domain in the nanomagnetic particles and relaxation imaging concepts.

Chapter 5 focuses on the sample preparation and describes the experimental setup used in this research. The NV ensemble diamond is used as the relaxation sensor for a superparamagnetic core-shell particle. A spin relaxation experiment and imaging with a home-built confocal microscope are given in this chapter.

Chapter 6 describes the experimental results of local magnetic field analysis and the superparamagnetic behavior. The magnetic B-H curve was detected by ESR and discovered magnetic vectors at a different position across the core-shell particle.

Chapter 7 summarizes the results and discussion in detail. The perspective and applications for future works.

Chapter 2

Quantum Sensing of NV Center in Diamond

The defects in a diamond crystal have been studied for several decades, indicating the impurities in crystal structures, especially nitrogen, boron, and silicon. Each defect exposes the color of the crystal known as the color center. In solid-state and quantum physics, scientists have demonstrated a robust spin coherence system, high sensitivity, and measurable under ambient conditions for various applications. This promising and utility defect center is the nitrogen-vacancy center (NV Center) in diamond, consisting of a nitrogen atom (N) substituted for a carbon atom (C) and a neighboring vacancy atom (V) in the diamond structure where the crystal is based on C_{3v} symmetry.[5,6] The NV centers are classified by four possible crystallographic axes ($[1\bar{1}\bar{1}]$,$[\bar{1}\bar{1}1]$,[111], and $[\bar{1}1\bar{1}]$) originated from diamond tetrahedral structure and orientation of the symmetry axes[7] as shown in Fig 2.1. The demands of diamonds are not only for decorations and gorgeousness but also for utility in science and technology applications. However, diamond defects can be found in nature but are not controllable in the number of defects and density for appropriate applications. Consequently, diamond synthesis has been studied and developed to support these requirements of the diamond denoted as the laboratory-grade diamond. The synthesized diamonds are commonly from one of these two methods, high-pressure-high-temperature (HPHT)[8,9] and chemical vapor deposition (CVD).[10–12] Furthermore, the NV density can be controlled by varying electron irradiation and annealing conditions to support the magnetometry applications.[13,14] Thus, it is evident that the NV density in the diamond structure plays the most important role in magnetic

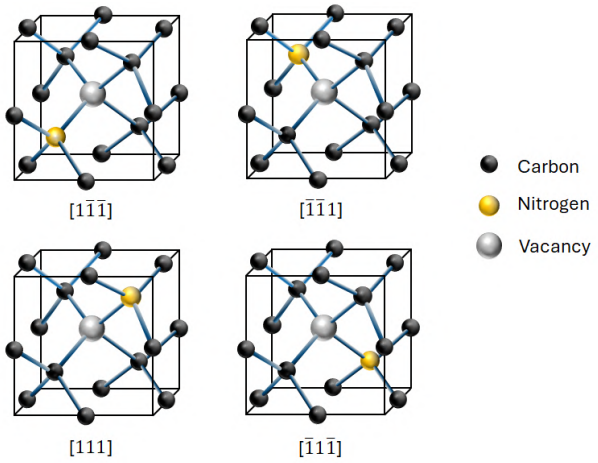

Figure 2.1: Diamond structure with four possible orientations of NV centers in diamond. The blackball represents a carbon atom, the yellow one is a nitrogen atom and the white one is a vacancy.

sensing. In this chapter, the electronic structure and properties of the NV center are described, including the spin state of the unpaired electrons in the ground state.

2.1 Diamond Structure and Properties

The NV defect center exists in two main types of charge states, one is a negatively charged NV center, (NV^-) and another is a neutral NV center, (NV^0). When substituted nitrogen forms in a carbon lattice due to the covalent bond from 3 valence electrons of nitrogen and carbon atom, two electrons are left as a lone pair to the vacancy atom, bonding with another three carbon atoms by Dangling bonds. In this case, it is defined as NV^0, which contains a total spin angular momentum, $S = \frac{1}{2}$. On the other hand, the NV^- traps one electron from the conduction band and gives a spin $S = 1$ according to the spin triple state.[15,16]. To determine the feature of these charge states, the optical resonance spectrum line is observed and distinguished when an electron from the lowest vibrational ground state absorbs a photon and is promoted to the excited state. This absorption line is called the zero phonon line, (ZPL)[17,18] and other broadband wavelengths are produced from phonon absorption and emission, called phonon side band, (PSB), illustrated in Fig. 2.2(a) and (b). After absorption, the electron relaxes to the bottom of the excited state by a non-radiative process and then returns to the ground state by lower energy photon emission, known as the Stokes shift. The zero phonon line measured

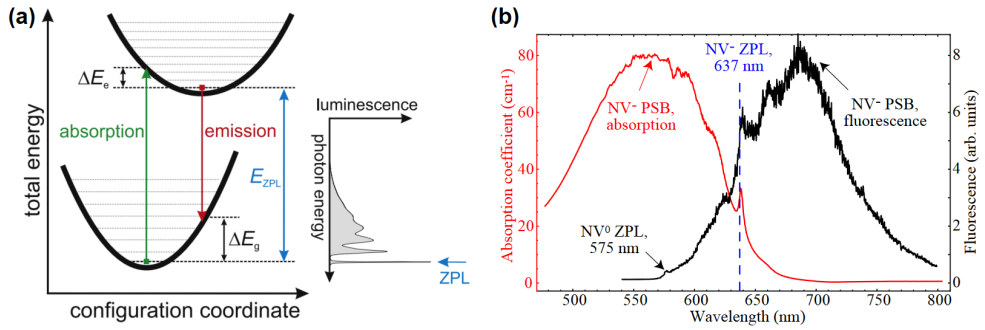

Figure 2.2: (a) Vibrational energy structure of NV center with photoluminescence transition absorption and emission. (b) Absorption and emission spectra with the photon side band and zero phonon line of NV^0 and NV^-. ((a) adapted from A. Alkauskas et al., [17] and (b) adapted from V. M. Acosta thesis [18]).

at intrinsic energy between the ground state and the excited state of the vibrational energy of the NV structure, 2.156 eV or 575 nm and 1.945 eV or 637 nm for NV^0 and NV^-, respectively. In this study, we emphasized the NV^- as the most sensitive and outstanding for the magnetic field applications[19] and denoted as NV center for all content in this thesis. The electronic structure of the NV center is composed of the ground triplet state ($^3A_2$) and an excited triplet state (^3E), located in between valence band and conduction band of diamond structure with a wide band gap of 5.5 eV. The excited state is about 0.6 eV under the conduction band. In practice, a high-power light source can excite the electrons from the ground state, promote them through the excited state, and leave an electron in the conduction band, transforming to a neutral NV center due to this tiny proximity.[20]

2.2 Optical Read Out and Spin Properties of NV Center

Because the main resonant transition wavelength of ZPL is 637 nm, NV center can be excited by a higher frequency or lower wavelength of ZPL. In this case, we illuminated the NV diamond with a green laser, with a 532 nm wavelength, to excite the electrons in the ground state to be polarized. There are three main energy states of two spin systems of NV center, a ground state, ($^3A_2$), an excited state, (^3E) and a metastable state. in the absence of an external magnetic field, the ground triplet state contains three spin sublevels, the singlet state, $m_s = 0$ and the doublet degeneracy state[21]

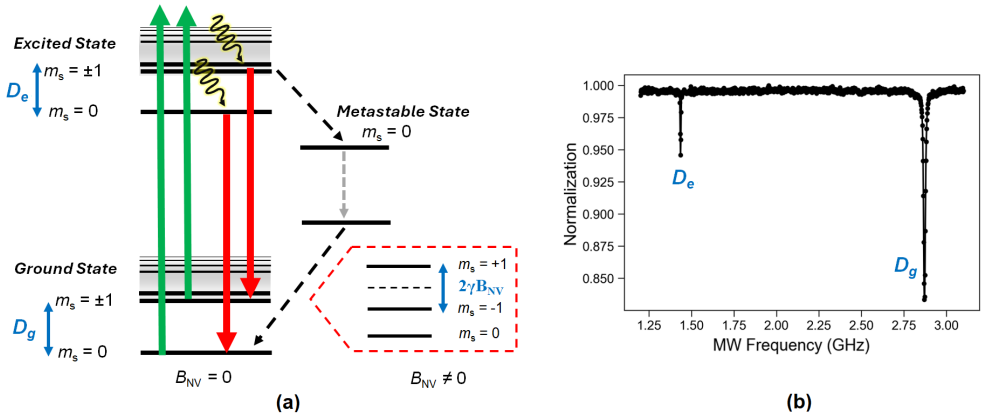

Figure 2.3: Schematic of the NV^- energy level. The illumination of a green laser with $\lambda = 532$ nm promotes the electron population from the ground state into the excited state. The electron-phonon coupling (zigzag line) relaxes to the lowest vibrational level of the excited state by the non-radiation process before returning to the ground state $m_s = 0$ and radiating a lower energy photon of 637 nm (red light). Meanwhile, the $m_s = \pm 1$ population mostly decays via a non-radiation through the metastable state by changing spin to $m_s = 0$, resulting in diminished fluorescence intensity. (b) dips of fluorescence intensity corresponding to ZFS of excited state and ground states of the NV structure.

$m_s = \pm 1$, which are separated by the zero-field splitting, (ZFS), $D_g = 2.87$ GHz. Identically, the doublet degeneracy state in the excited triplet state also has ZFS, $D_e = 1.42$ GHz.[15,22]

2.2.1 Optically Detected Magnetic Resonance (ODMR)

One of the most important advantages of the NV center is that it is photostable at room temperature and the changing of fluorescence is measurable as a function of time. In addition, the magnetic resonance is proportional to frequency splitting caused by the Zeeman effect. For these reasons, the simple spectroscopy technique commonly used to investigate the magnetic resonance and spin coherence in the NV centers is the optically detected magnetic resonance[16] and so-called ODMR for short. ODMR has the capability to monitor fluorescence as a function of microwave frequency. During sweeping the microwave around the resonant frequency, the fluorescence is recorded. When the frequency is matched with the resonant frequency of the NV centers, the fluorescence contrast is exposed outstandingly. Obviously, the zero-field splitting divides two magnetic spins into the microwave range.

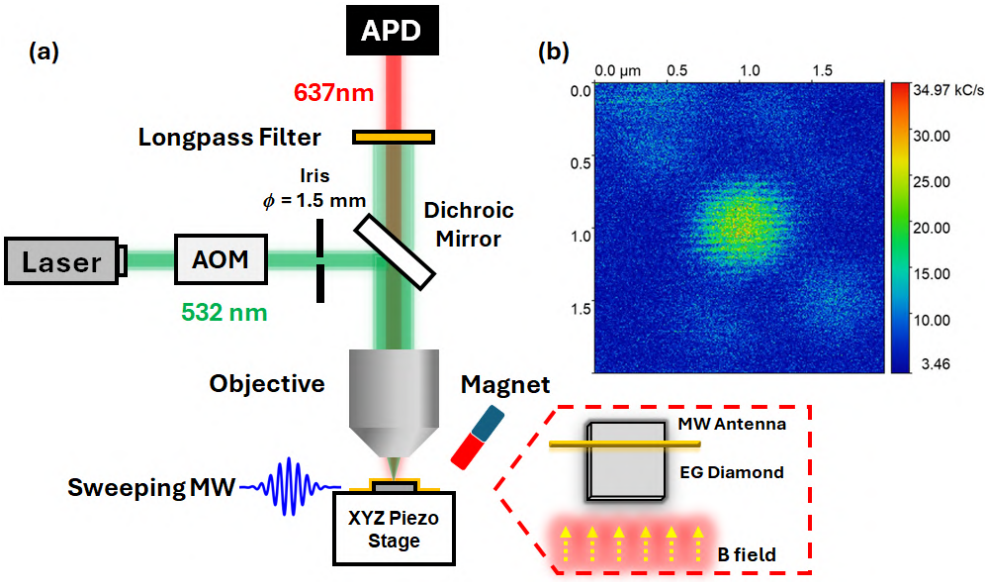

Figure 2.4: (a) Diagram of a simple ODMR setup and a diamond sample on the XYZ piezo stage. (b) The fluorescence image of a single NV center in an electronic grade diamond.

Consequently, these two sublevels can be manipulated by applying microwave radiation. By applying the external magnetic field, the degeneracy state of $m_s = +1$ and $m_s = -1$ are distinguished corresponding to Zeeman splitting, $2\gamma B_{NV}$ (see Fig. 2.3).

When the degeneracy ground state, $m_s = \pm 1$, is manipulated by a microwave excitation at 2.87 GHz during spin-polarized by a green laser, the initial spin starts at $m_s = \pm 1$ before exciting to the excited state. The electron-phonon coupling occurs and relaxes to the bottom of the excited state by a non-radiative process. The most electron population in this state tends to decay to a metastable singlet state and change the magnetic spin to $m_s = 0$ by intersystem crossing (ISC).[23,24] This process causes the 1042 nm infrared emission and drops other fluorescence intensity by 30% approximately[25]. This phenomenon is from the electron spin resonance (ESR) of the NV center in a diamond.

Generally, the ODMR setup is combined with a laboratory home-built confocal scanning microscope based on Galvano mirrors and a laser scanning system. However, the XYZ piezo stage is used as a 3D position scanner in Fig. 2.4. When the diamond sample is placed on a PCB microstrip line with a 25 μm diameter Au wire as a microwave antenna, and set on the piezo scanner.

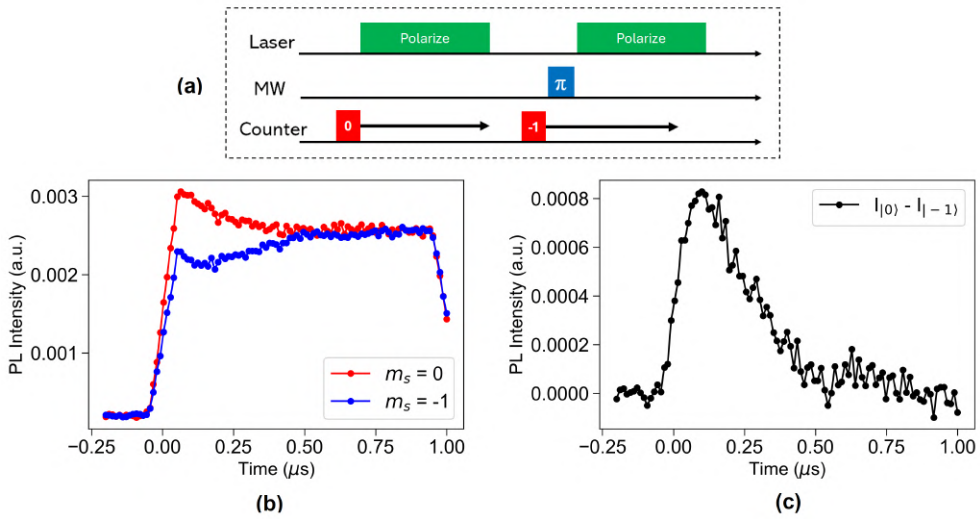

Figure 2.5: (a) The pulse sequence of time-resolved fluorescence spin dependence. (b) Time-resolved fluorescence of a single NV between two initial states measured during 1 μs laser pulse. (c) The different fluorescent intensity between two states, $m_s = 0$ and $m_s = -1$, indicates fluorescence contrast and equilibrium state after 0.50 μs.

The green laser pulse is controlled by an acoustic-optic modulator (AOM) through the Iris to illuminate a clean Gaussian beam into the diamond. The 100x objective lens with 0.9 numerical aperture (NA) is set up to focus the laser beam on the diamond. In this case, we normally use a low-power laser, around 1 mW at the sample, to avoid NV charge conversion. The 600 - 800 nm fluorescence emission is accumulated into a dichroic mirror. A longpass filter will block the broadband fluorescence to ensure that a red photon can pass to an avalanche photodiode (APD) as a detector of the ODMR system. The microwave generator, laser source, and APD counter are combined with the RF switches and connected to the pulse blasters to generate the pulse sequences as the timing control experiments.[26] In Fig. 2.5(a) depicted the pulse sequence for time-resolved fluorescence in a single NV which resulted in the different spin state fluorescence intensity as a function of time (Fig. 2.5(b) and (c)).

2.2.2 Spin Hamiltonian of Ground State NV Center

Various interactions of the NV center in diamond have been reported as environmental sensing applications such as magnetic spin sensing (electron spin, nuclear spin)[27–29], temperature[30–34], electric fields[35–37], electric charges,

electric current and voltage[38,39], strain[16,31,40] and pressure sensing.[34,41] In this work, we focus on the fundamentals of the magnetic field interaction of electron spin in the ground state of the NV center. The perturbation in the spin energy of the quantum magnetic sensing of the NV center can be simply described in terms of the ESR frequency lifting by using the Spin Hamiltonian, as shown

$$\widehat{H} = D_g S_z^2 + E\left(S_x^2 - S_y^2\right) + \gamma \mathbf{B} \cdot \mathbf{S} \tag{2.1}$$

Where $D_g = 2.87$ GHz is on-axis ground state zero-field splitting, E is off-axis zero-field splitting from strain in the diamond crystal which can be in several kHz to a few MHz ranges,[19] $\mathbf{B}$ is the vector of magnetic field (B_x, B_y and B_z), $\mathbf{S}$ represents S_x, S_y and S_z as the Pauli matrices, $\gamma = g\mu_B/h \cong 28$ MHz/mT, is the electron gyromagnetic ratio, $g \simeq 2.0$ is the Landé g-factor, h is the Planck constant, and μ_B is the Bohr magneton.[42]

In the presence of the external magnetic field along the quantization axis of the NV center, denoted as S_z of the Pauli vector. In this case, the strain is extremely weak according to an electronic-grade diamond, ($E \ll D_g$), and can be negligible for simplicity. Thus, we can derive other coordination to be zero, ($\mathbf{B} = 0, 0, B_z$), and the $\widehat{H}$ can be written by[43]

$$\widehat{H} = \begin{pmatrix} D_g + \gamma B_z & 0 & 0 \\ 0 & 0 & 0 \\ 0 & 0 & D_g - \gamma B_z \end{pmatrix} \tag{2.2}$$

In Eq. 2.2, the eigenstates are the resonance frequencies of the spin transition of $m_s = -1$ and $m_s = +1$, denoted as f_- and f_+, respectively. Thus, the different frequencies between f_- and f_+ can be calculated by

$$f_\pm = D_g \pm \gamma \left|\mathbf{B}_z\right| \tag{2.3}$$

$$f_+ - f_- = \Delta f = 2\gamma \left|\mathbf{B}_z\right| \tag{2.4}$$

In Fig. 2.6(a), the continuous wave ODMR (CW-ODMR) demonstrates when a green laser is applied and MW is swept continuously. A counter records the fluorescence with and without MW as the signal and reference,

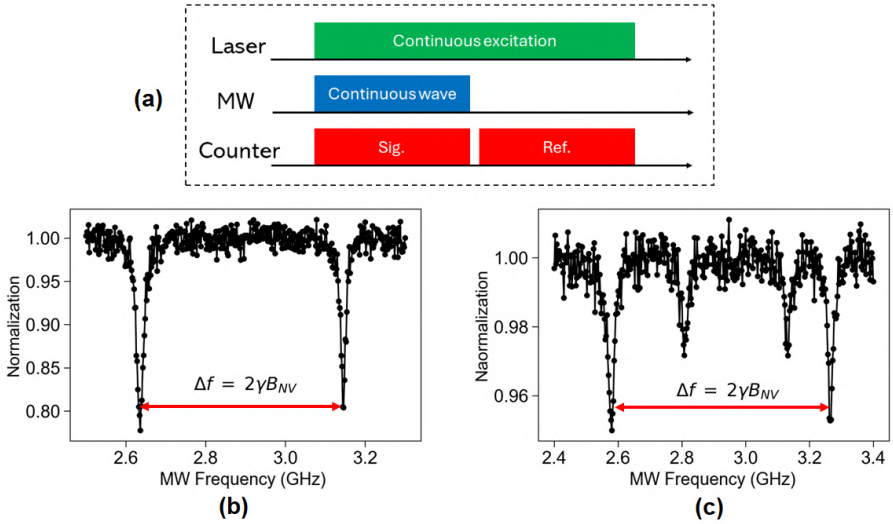

Figure 2.6: (a) The continuous laser and MW excitation in the CW-ODMR experiment. (b) Fluorescence spectrum of a single NV center from ODMR experiment as the function of microwave frequency. The result depicted that the fluorescence intensity reduces at the transition frequency of the $m_s = -1$ and $m_s = +1$ separated by the Zeeman energy. (c) Fluorescence spectrum from ensemble NV center when the magnetic field is applied along one of the NV axes.

respectively. When an external magnetic field is applied along one of the NV axes parallelly, two spin sublevels, $m_s = \pm 1$, are separated by the Zeeman effect. The magnitude of an external magnetic field is proportional to the Zeeman energy in terms of frequency, $\Delta f = 2\gamma B_{NV}$, where $B_{NV} = B_z$ is the magnetic field parallel to the NV quantization axis (see Fig. 2.6(b) for a single NV). At the same time, other NV axes make an equal angle of 109.5° with the vector of the external magnetic field (see Fig. 2.6(c) for an ensemble NV).

Once we consider the non-zero local strain in diamond ($E \neq 0$) in the Spin Hamiltonian and the external magnetic field is parallel to the NV axis, $\widehat{H}$ can be written by

$$\widehat{H} = \begin{pmatrix} D_g + \gamma B_z & 0 & E \\ 0 & 0 & 0 \\ E & 0 & D_g - \gamma B_z \end{pmatrix} \tag{2.5}$$

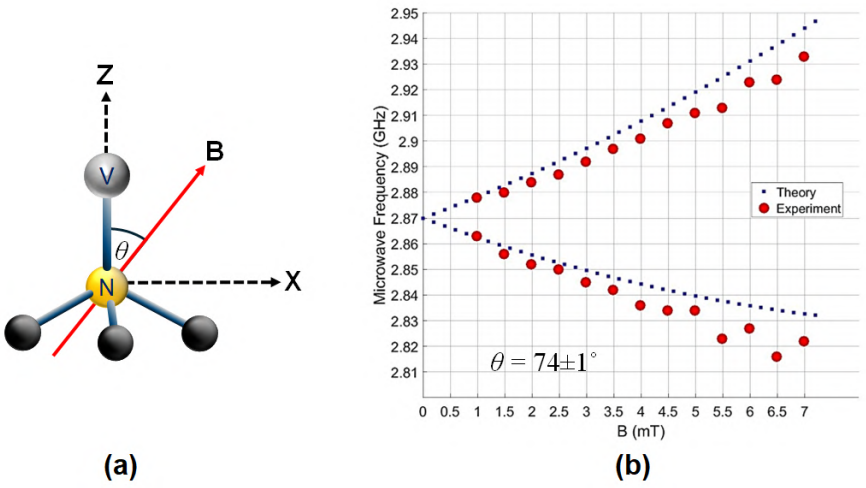

Figure 2.7: (a) The C_3v symmetry model of the NV center with an external magnetic vector with θ angle respect to the NV axis. (b) The simulation of Zeeman splitting compared with the ODMR experimental result by varying the magnetic field at $\theta = 74 \pm 1^{\circ}$.

By using the quadratic formula, $ax^2 + bx^2 + c = 0$, the eigenstates of Eq. 2.5 can be calculated by[19]

$$f_{\pm} = D_g \pm \sqrt{\gamma^2 B_{NV}^2 + E^2} \tag{2.6}$$

Since the external magnetic field is misaligned with the NV axis, we can define θ as the angle between the external magnetic vector and the NV axis of interest in the XZ plan as shown in Fig. 2.7(a). The $\mathbf{B}\cdot\mathbf{S}$ term in Eq. 2.1 can be expressed as dot product in matrix notation, $\mathbf{B}^T\mathbf{S} = B_x S_x + B_y S_y + B_z S_z$. According to the magnetic field in the XZ plan, we assume the $B_y = 0$ and thus, $Bx = B\sin\theta$ and $Bz = B\cos\theta$. Consequently, the spin Hamiltonian in Eq. 2.1 can be rewritten as[44]

$$\widehat{H} = D_g S_z^2 + E\left(S_x^2 - S_y^2\right) + \gamma B\left(S_x \sin\theta + S_z \cos\theta\right) \tag{2.7}$$

In Fig. 2.8, The ODMR spectrum demonstrates the different conditions of degeneracy state between zero magnetic field and various magnetic fields interacting with a single NV center with $\theta = 74 \pm 1^{\circ}$. For any θ, the $\widehat{H}$ in term of matrix components can be expressed by

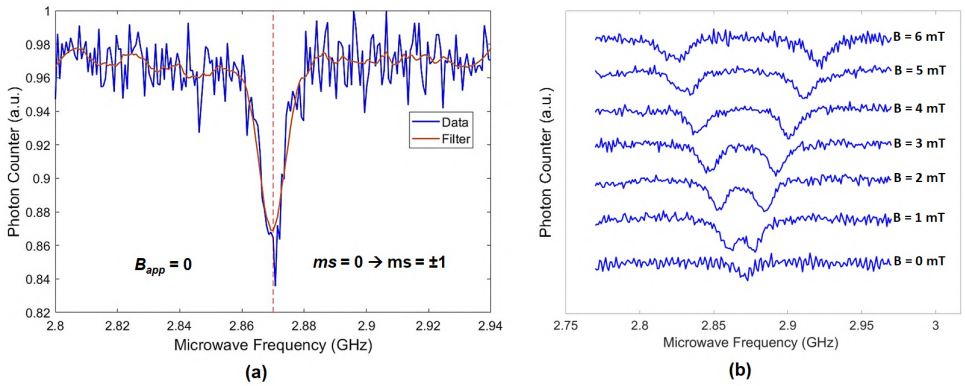

Figure 2.8: The Fluorescence spectrum as a function of microwave frequency recorded from CW-ODMR experiment. (a) Without a magnetic field applied, ($B_{app} = 0$), fluorescence drops at the transition frequency, 2.87 GHz when the electrons transition to $m_s = \pm 1$ sublevels. (b) In the presence of a magnetic field, the magnetic vector projection angle is $\theta = 74 \pm 1^{\circ}$ with various magnitudes. The $m_s = -1$ and $m_s = +1$ are separated because of the Zeeman effect.

$$\widehat{H} = \begin{pmatrix} D_g + \gamma B cos\theta & \frac{\gamma B sin\theta}{\sqrt{2}} & 0 \\ \frac{\gamma B sin\theta}{\sqrt{2}} & 0 & \frac{\gamma B sin\theta}{\sqrt{2}} \\ 0 & \frac{\gamma B sin\theta}{\sqrt{2}} & D_g - \gamma B cos\theta \end{pmatrix} \tag{2.8}$$

In the case of $\theta = 90^{\circ}$, the magnetic field is perpendicular to the NV-axis. As a consequence of this alignment, Eq. 2.8 can be rewritten as

$$\widehat{H} = \begin{pmatrix} D_g & \frac{\gamma B}{\sqrt{2}} & 0 \\ \frac{\gamma B}{\sqrt{2}} & 0 & \frac{\gamma B}{\sqrt{2}} \\ 0 & \frac{\gamma B}{\sqrt{2}} & D_g \end{pmatrix} \tag{2.9}$$

In Fig. 2.9, $B_{\perp}$ or off-axis magnetic fields also induce spin mixing and reduce overall the excited level lifetime and cause the increasing of the probability in ISC transitions[45,46], resulting in fluorescence drop when using diamond scanning probe on the magnetic pattern sample[46].

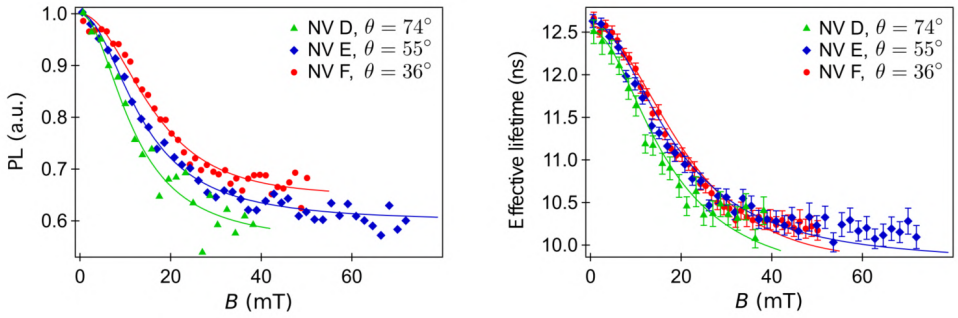

Figure 2.9: (a) The PL intensity and (b) the effective lifetime as a function of B with different angles. (adapted from J.-P. Tetienne et al[46]).

2.3 Bloch Sphere

In quantum mechanics, the total spin state of the particle is defined as $2S+1$. For example, the total spin state for a total spin angular momentum, $S = 1/2$ is two states, $(2\left(\frac{1}{2}\right) + 1 = 2)$, $m_s = -1/2$ and $m_s = +1/2$. Otherwise, For a total spin angular momentum, $S = 1$, there are three total spin states: $m_s = -1$, $m_s = 0$, and $m_s = +1$. In this section, a Bloch sphere is introduced as the geometric spin visualization during microwave manipulation including the Dirac notation[47,48] that the vector state is presented with a ket in a Bloch sphere. The NV center contains the two-level spin system that performs quantized eigenstates of $|0\rangle$ for $m_s = 0$ and $|1\rangle$ for $m_s = +1$ or -1 in the ground triplet state. The superposition of a two-level system is given by

$$|\psi\rangle = a|0\rangle + b|1\rangle \tag{2.10}$$

where a and b are the complex coefficients for each eigenstate wavefunction. The normalization condition for $\langle\psi\,|\,\psi\rangle = 1$ is

$$|a|^2 + |b|^2 = 1 \tag{2.11}$$

The two-level quantum state can be represented as a coherent superposition of the vector in the Bloch sphere, called the Bloch vector. Generally, the Bloch sphere consists of two independent poles, where the eigenstate $|0\rangle$ is at the north pole and $|1\rangle$ is at the south pole. In the Fig. 2.10, the Bloch vector can describe the quantum qubit state given by[49]

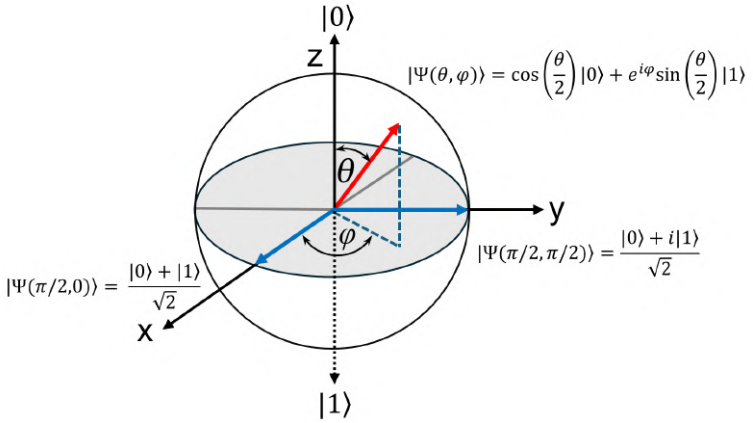

Figure 2.10: The Bloch sphere geometrically represents the Bloch vector of spin state lie on the equator of the sphere corresponding to the rotation and phase angle. The superposition states ($\theta = \pi/2$) are located in both x- and y-axis depending on the angle φ.

$$|\psi(\theta,\varphi)\rangle = \cos\left(\frac{\theta}{2}\right)|0\rangle + e^{i\varphi}\sin\left(\frac{\theta}{2}\right)|1\rangle \tag{2.12}$$

where θ is the angle of rotation between two states, and φ is phase of the state. For example, the superposition states can be determined where $\theta = \pi/2$ as shown

$$|\psi(\pi/2,\varphi)\rangle = \frac{1}{\sqrt{2}}\left(|0\rangle + e^{i\varphi}|1\rangle\right) \tag{2.13}$$

while the phase $\varphi = 0$ and $\varphi = \pi/2$ correlate with the x and y axis, respectively.

2.4 Rabi Oscillation

In the presence of a magnetic field, the electron spin of the NV center is continuously excited by a resonant microwave pulse while increasing pulse duration continuously. The excited spins start from $m_s = 0$ to $m_s =$ -1, for example, and then return to $m_s = 0$ again. We exploit this two-level system, $m_s = 0$ and $m_s = -1$ or $m_s = +1$, as a spin qubit that undergoes a precession frequency, called the Larmor precession of the spin,

$\omega_L = \gamma B$. The Bloch sphere describes the spin manipulation where the north and south poles are represented by the eigenstates, $|0\rangle$ and $|1\rangle$, respectively. The eigenstates, $|0\rangle$ is bright fluorescence when $|1\rangle$ is dropped fluorescence in the ODMR experiment. The oscillation of fluorescence between these two states is known as Rabi Oscillation. Thus, the frequency of Rabi oscillation is called Rabi frequency (ω_R). The process of Rabi oscillation is based on the pulse measurement as demonstrated in Fig. 2.11(a). The spin state is initialized by a pulse laser to $m_s = 0$ at the starting pulse. The first photon counter starts before the end of the initialization for 300 ns, as the total fluorescence contrast can be recorded (See Fig. 2.5(c)), to collect the fluorescence intensity as the reference. Next, the microwave pulse drives with a resonance frequency of $m_s = -1$ or $m_s = +1$. A delay time can be put between a laser pulse and a microwave pulse driving for a hundred ns to several μs to confirm that most population is polarized to $m_s = 0$ state completely.[23,50–53] During a single step of the evolution of microwave pulse duration, the second photon counter with 300 ns is started coincidentally with the second laser pulse as the read-out sequence. The remaining population of $m_s = 0$ is read as the signal fluorescence.

The Rabi oscillation results are normalized by Sig./Ref. as shown in Fig. 2.11(c). The Rabi frequency in Hz, f_R is estimated by fitting with the exponential decay function, $A\exp(-\tau/T_R)\cdot\cos(2\pi f_R\tau) + B$ when A and B are the constant, T_R is the decay time constant of the Rabi oscillation.[53,54] The π and $\pi/2$-pulse are extracted from f_R by $\tau_\pi = 1/2f_R$ and $\tau_{\frac{\pi}{2}} = 1/4f_R$, respectively. The microwave excitation protocol is basically when the magnetic field strength of the incident microwave, B_{MW}, is perpendicular to the NV axis at the resonance frequency, for having a strong dipole oscillation.[55] The Rabi frequency is given by $\omega_R = \gamma B_{MW}$ which the oscillating magnetic field of the microwave is proportional to its excitation power,[56,57] making the Rabi frequency is the power dependence, $\omega_R \propto \sqrt{P_{MW}}$.

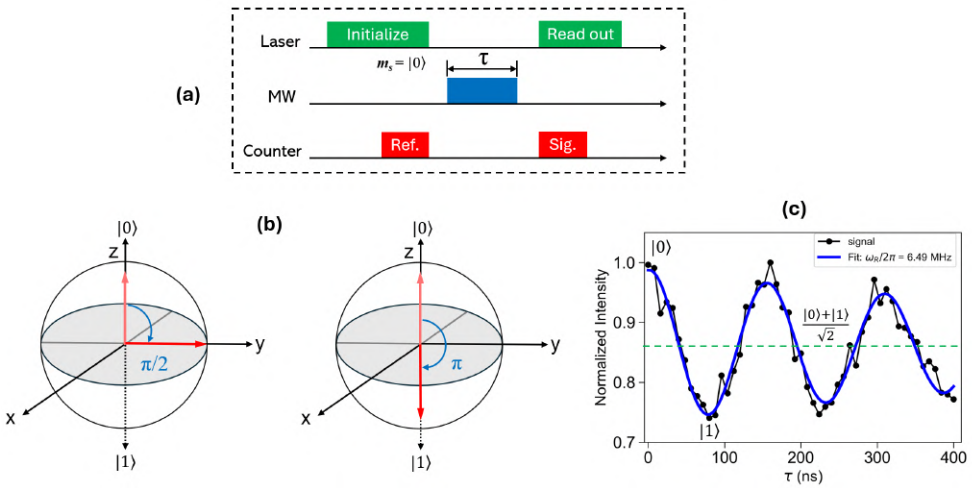

Figure 2.11: Rabi Oscillation protocol. (a) The pulse sequence for the Rabi experiment. The 3 μs green laser initializes the spin state to polarize at $m_s = |0\rangle$. Before starting the microwave, the delay time can be around a hundred ns up to several μs to ensure that the majority population will become polarized. Subsequently, a resonant microwave pulse with a varied duration (τ) starts continuously. The 300 ns width photon counter can be read at the initial state as the reference, and the signal's counter also starts with a read-out laser pulse to reflect the residual probability of $m_s = |0\rangle$ state. (b) The Bloch vector of the spin state rotates after $\omega_R \cdot \tau = \pi/2$ and π pulses for the superposition and $m_s = |1\rangle$ states, respectively. (c) The Rabi oscillation result measured on a single NV center, corresponding to (b)

Chapter 3

DC and AC Magnetic Sensing

The most important sensing protocol of quantum sensing via diamond allows for magnetic sensing applications with high spatial resolution. The majority of NV sensors are commonly used to detect not only the magnetostatic field but also the oscillating magnetic field and dipole coupling in hyperfine interaction in atoms. Consequently, magnetometry via NV center in diamonds become interesting in this present. The first NV center magnetic detection was proposed by J.M. Taylor et al,[58] in which the magnetic spin was identified in nanoscale with the direct proximity of spin particles. Because of the strong covalent bonds in carbon lattices, a high impurity NV center intrinsically demonstrates an extremely long coherent time at room temperature and ambient conditions by transverse relaxation times, $T_2 = 1.8$ ms, in an engineered CVD diamond.[59] For the longitudinal relaxation time, T_1, which is commonly from the interaction of phonon in the diamond lattice and temperature dependence.[19,60] In this chapter, we outline the continuous and pulse measurement techniques on the NV center in diamond. The ODMR spectroscopy is utilized to yield the DC magnetic field including timing control microwave pulse to detect phase accumulation in the AC magnetic field.

3.1 Continuous Wave ODMR

The ordinary technique to manipulate the spin state in the NV center is the continuous wave ODMR (CW-ODRM)[61], a straightforward method to measure the static field component. As described in Section 2.2.1, the ODMR spectrum extracts the fluorescence intensity as a function of microwave frequency through continuous laser excitation and microwave radiation. For the

microwave sweeping across the spin transition frequency, the off-resonance with laser excitation yields a stable fluorescence until the resonance frequency, the reduced fluorescence due to the ISC decay is monitored. For weak magnetic sensing, the Zeeman effect splits the transition frequency between $|0\rangle \rightarrow |-1\rangle$ and $|0\rangle \rightarrow |+1\rangle$ resulting in this different frequency is $2\gamma B_{\parallel}$ in case of the parallel magnetic field. For a high magnetic field, the transverse component of the magnetic field, $B_{\perp}$, predominantly induces the mixing of NV spin states ($m_s = 0$ and $m_s = \pm 1$) that reduces the NV spin lifetime and causes the decrease in the fluorescence spectrum of ODMR contrast.[62,63] The CW-ODMR technique is simpler to setup more than the pulse ODMR and can overcome the inhomogeneous microwave during the experiment.[43] The CW-ODRM sensitivity is verified by a minimum detectable magnetic field limited by the photon shot-noise as follows[43,51,64]

$$\eta_{cw} = \frac{4}{3\sqrt{3}} \frac{\Delta\nu}{\gamma C\sqrt{R}} \tag{3.1}$$

Where $\Delta\nu$ is the full-width-at-half-maximum (FWHM) linewidth of the CW-ODMR dip, γ is the gyromagnetic ratio of the electron, C is the ESR contrast from the CW-ODMR spectrum, and R is photon-detection rate. We can express $R = I_0 t$, I_0 is the NV fluorescence intensity and t is the averaging time.[65] Therefore, $4/3\sqrt{3}$ denotes the steepest slope of the Lorentzian profile.

3.2 Pulse ODMR

From Eq. 3.1, the broadened spectral linewidth causes the lack of high sensitivity in the CW-ODMR, which prevents other important pulse measurement techniques for the magnetometry. Pulse ODMR is a promising candidate to improve the sensitivity of NV magnetic sensing. Generally, AOM is connected to the laser source and triggered by a pulse blaster through the RF switch, as well as the microwave source and APD. When the laser illuminates to polarize the NV spin to $m_s = 0$ for a few microseconds, the microwave starts to manipulate the spin states during the laser off, for example, Rabi oscillation experiment as shown in Fig. 2.11(a). This protocol helps to reduce the power broadening of the ODMR linewidth which restrains the DC magnetic sensitivity.[51]

3.3 Ramsey Interferometry

The spin dynamics in the NV center are based on a two-level system as shown in the Rabi oscillation. However, the magnetic sensitivity is limited by continuous polarization by green laser and dominant microwave in CW-ODMR.[66] In Fig. 3.1, when the $\pi/2$-pulse microwave is applied, the NV spin state is initial in between $|0\rangle$ and $|1\rangle$ for the superposition state, where it is an unperturbed state for the free-induction decay (FID) observation. The Ramsey pulse sequence is achieved by applying the microwave pulse sequence $\pi/2-\tau-\pi/2$, where τ is the free precession time, evolves without a dominant microwave during the superposition state. The first $\pi/2$-pulse makes the Bloch vector align on the equator sequentially, the time evolves freely under a DC magnetic field perturbation with phase (φ) accumulation. The last $\pi/2$-pulse rotates the vector to the initial measurement state. Consequently, the phase information accumulated under the DC magnetic field is[6,59]

$$\varphi = \gamma \int_0^\tau B(t)dt \tag{3.2}$$

The fluorescence intensity is recorded with several repetitions and plotted with the evolution time, τ to demonstrate the oscillation, called Ramsey fringes.[67] the Fourier transform of the Ramsey fringes discovers the different transition frequency under the different bias of the DC magnetic field, equal to the ESR result from CW-ODMR experiment.[6,68] The hyperfine interaction also responds to the NV center revealing the beat frequency in the Ramsey fringes. The damping oscillation occurred due to the spin bath, for example, the carbon isotope ^{13}C spin bath in high impurity diamond which leads to the oscillating magnetic field during the measurement time. The decay time from the total Ramsey fringes is described by the time constant T_2^*, which is denoted as dephasing time. Thus, the fluorescence intensity as a function of free evolution time can be fit with $I_{RS} = A\exp(-\tau/T_2^*)^n \cdot \sin(2\pi f\tau + \varphi) + B$, where A and B are the constant, f is the fringe frequency, n is the stretched exponential parameter and φ is a rotating phase.[69]

3.4 Spin Echo and Coherence of NV Spin

The quantum sensing for AC magnetic field detection relies on the dynamical decoupling (DD) technique, which employs pulse sequences to eliminate the inhomogeneous magnetic field and increase the coherent time. By improvement of Ramsey interferometry, a π-pulse is added in the middle of

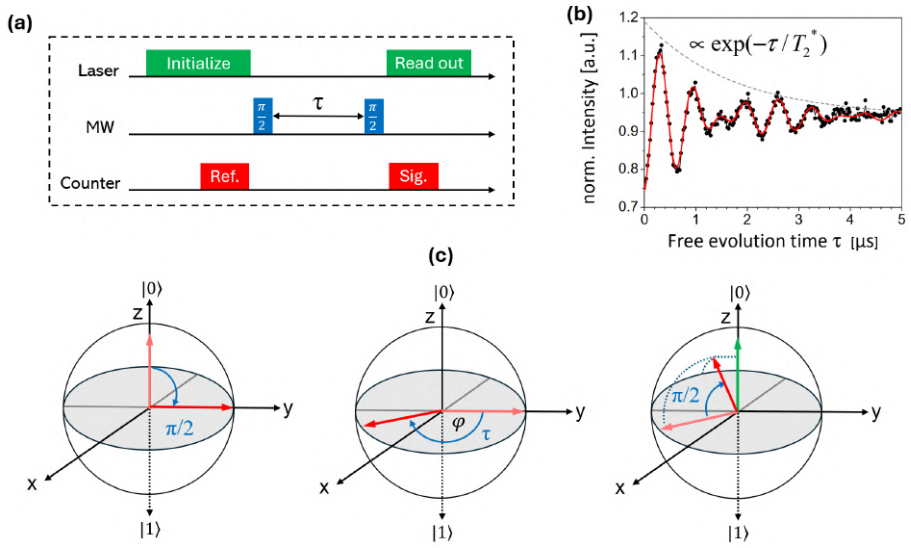

Figure 3.1: (a) The Ramsey pulse sequence. (b) The Ramsey fringes are depicted by the fluorescence intensity plotting with free evolution time. The FID is proportional to the exponential decay as the function of the electron spin precession (adapted from E. O. Schafer-Nolte [67]). (c) The geometrical dynamic of Ramsey interferometry in Bloch sphere. The phase accumulation, φ, is pick up during the free evolution time, τ.

two $\pi/2$-pulses. This technique can ignore the DC magnetic bias but sense the AC field by reflecting phase accumulation as the fluorescence intensity. This protocol is known as Hahn Echo or Spin Echo (SE), which E. L. Hahn proposed in the 1950's.[70] Spin echo consists of $(\pi/2 - \tau - \pi - \tau - \pi/2)$ sequences. The first $\pi/2$-pulse initializes the NV spin into the superposition state. During the first free evolution time, the spin start dephasing under the inhomogeneous static field. Sequentially, the π-pulse flips the spin over 180° before a second free evolution time in order to refocus the dephasing phase. The first and the second free evolution time are equal during π-pulse, this causes the total phase accumulation to be canceled symmetrically. In other words, the DC dephasing effect is eliminated and the alternative magnetic field from others is outstanding, which causes a longer coherent time than T_2^*.[43] The phase accumulation from the total spin echo sequence is given by

$$\varphi_{SE} = \gamma \left(\int_0^{\tau/2} B(t)dt - \int_{\tau/2}^{\tau} B(t)dt \right) \tag{3.3}$$

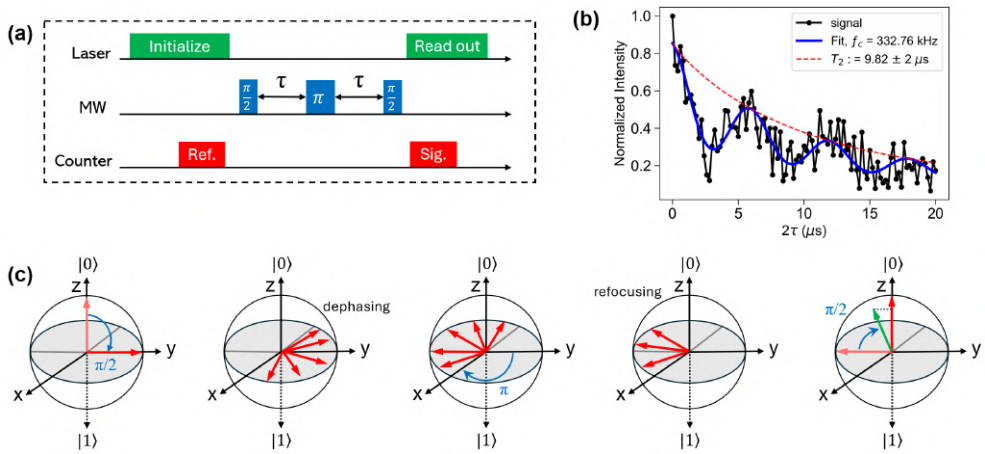

Figure 3.2: (a) The spin echo pulse sequence improved from Ramsey protocol by adding a π-pulse in the middle. (b) Spin echo result from an NV ensemble diamond under the magnetic field $B_{NV} \approx 31$ mT along one of NV axes. The data is fit by Eq. 3.4, reveals the periodic revival corresponding to Larmor frequency of ^{13}C nuclear spin and coherent time T_2. (c) Bloch sphere demonstrated each step of spin echo.

In case of the HPHT or CVD single crystal diamond containing ^{13}C isotope with 1.1% natural abundance,[71] when the ^{13}C nuclear spin has a precession influenced by a magnetic field, spin echo reveals the collapse and revival of ^{13}C nuclear spin bath ($I = 1/2$) periodically with the Larmor precession frequency of 10.71 kHz/mT, on the contrary, the ^{12}C is nuclear spinless ($I = 0$), has no spin[72]. The fluorescence decay rate as a function of interval time is determined as the time constant of the spin-spin relaxation or the coherent time, T_2, that plays the most important role in quantum sensing.

In Fig. 3.2(b), we recorded spin echo from an electronic grade NV ensemble diamond and obtained the precession frequency of ^{13}C nuclear spin by fitting to[72–74]

$$A + Be^{-(2\tau/T_2)^n} \sum_{i=0}^{3} e^{-((2\tau - iT_{re})/T_{de})^2} \tag{3.4}$$

Where i is the number of revival peaks, T_{re} is the revival period, and T_{de} is the width of the revival peak.

3.5 Noise Spectroscopy

Noise is one of the main issues in quantum sensing and information. Mostly, noise source generates random fluctuations which can disturb the quantum states causing decoherence and losing actual quantum states. Noise spectroscopy in quantum systems is to study the noise properties and investigate the decoherence sources. This study helps to enhance the efficiency of quantum sensing and understand the coherence control quantum states. Noise spectroscopy is based on analyzing stochastic signals as a noise source with frequency spectrum and noise spectral density (NSD)[75] and spin relaxation.[6] Electron spins in the NV center are very sensitive to the environment. By applying external perturbation such as magnetic noise, electric charge, pH condition in chemical samples, and changing temperature, these parameters collide with the NV spin populations thus, reflecting the unstable superposition state of the NV spin. This collapse is known as decoherence.

The sensitivity windows of noise investigation can be achieved by using the filter functions $F(\omega)$ of the different methods of the dynamical decoupling pulse sequences as well as reconstruction of noise characteristics by the power spectral density $S(\omega)$, which determines noise power distribution across the target frequency ranges.[76] The signal of information is useful when the signal is correlated with a lagged time itself whether present noise or not. In other words, the fluctuation affects the system with a similar pattern as a function of delay time. Consequently, autocorrelation was used to investigate the periodic signals among noise and harmonic analysis. For example, random noise or white noise will not display a significant pattern because of non-autocorrelation over a series of times. When a fluctuating signal $V(t)$ is detected with two differences of the total time interval $T \to \infty$. The autocorrelation function $G_V(t)$ is given by[6,77]

$$G_V(\tau) = \langle V(t+\tau)V(t)\rangle \tag{3.5}$$

Where τ is the measurement time. The average function of time, t, is denoted as

$$\langle f(t)\rangle = \lim_{T\to\infty} \frac{1}{T} \int_{-\frac{T}{2}}^{\frac{T}{2}} f(t)dt \tag{3.6}$$

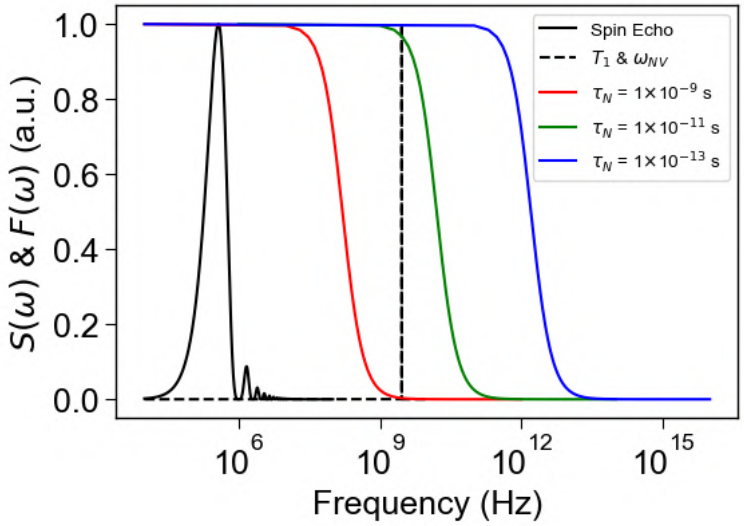

Figure 3.3: Power spectral density at different autocorrelation time for example, magnetization autocorrelation time from Néel relaxation τ_N and filter functions of Spin Echo and T_1 relaxometry protocols. (Adapted from E. Schäfer-Nolte [76]).

The interaction of noise distribution will be described in frequency domain for frequency respond analysis.[77] The Fourier transform of the autocorrelation is

$$S(\omega) = \int_{-\infty}^{\infty} e^{-i\omega\tau} G_V(\tau) d\tau \tag{3.7}$$

The noise analysis is presented by the power spectral density $S(\omega)$ in noise spectroscopy, also known as noise spectral density (NSD).

3.6 Decoherence Function

Decoherence function is to describe the probability when the quantum states cannot maintain the definite states by noise or sensing from the environment, leading to the wave function collapse. The decoherence can be investigated under different sequences of noise spectroscopy techniques based on various protocols such as Ramsey, Spin echo, and Relaxometry, depends on the power spectral density and filter function of each protocol. The decoherence decay associated with the transition probability $p(\tau)$ of the quantum states during

measuring interval τ is[6,75]

$$p(\tau) = \frac{1}{2}\left(1 - e^{-\chi(\tau)}\right) \tag{3.8}$$

The probability $p(\tau)$ is implied to the dephasing phase of the NV spin states during measurement time.[75] While $\chi(\tau) = \frac{1}{2}\phi^2_{rms}$ is called decoherence function which can be estimated by the root mean square (rms) of phase accumulation in time-domain. In addition, the analysis in the frequency domain is employed to determine the decoherence function which is related to frequency ranges of interest. This confines the noise distribution in terms of the frequency responses as follows[78]

$$\chi(\tau) = \frac{2}{\pi}\int_0^\infty \gamma^2 S(\omega) F(\omega) d\omega \tag{3.9}$$

Where $F(\omega)$ is the filter function which is associated with power spectral density and pulse measurement protocol.

3.7 Spin Relaxation Time

In the NV spin mechanism, when electrons are polarized in the excited state, the phonon interaction with the crystal lattices occurs inside the energy structure resulting in the NV spin population relaxing to the thermal equilibrium of the mixed state, which is unpolarized circumstance. This population decay time is known as spin-lattice relaxation T_1, or spin relaxation time for short. Ordinarily, T_1 relaxation is obviously temperature dependence because of broadening electron-phonon coupling by thermal energy.[60,79,80] Therefore, T_1 is also sensitive to fluctuation magnetic noise in the environment[81–85]. Thus, spin relaxation has been proposed to examine in noise spectroscopy with the power spectral density as the relaxometry.

In Fig. 3.4(a), the T_1 relaxometry is performed once the NV spins are polarized into $m_s = 0$ by a green laser excitation including either a microwave π-pulse or not, depending on which initial states will be measured. Suddenly, the laser is off and leaves the NV spins to maintain the population of the polarized state along the evolution time (dark time) τ. After a time τ, a laser is turned on to the readout process and the counter records the NV fluorescence of the remaining initial population after relaxation by time. The

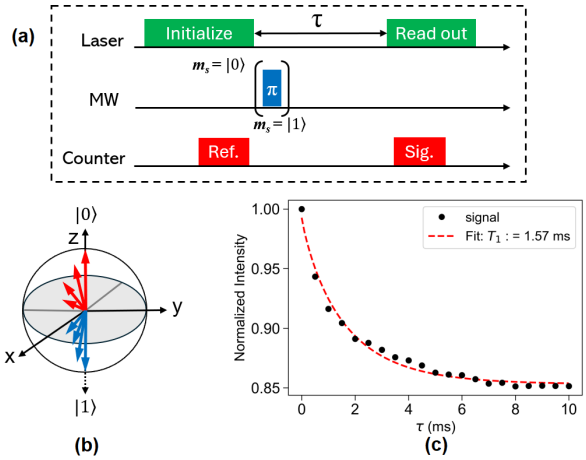

Figure 3.4: (a) The $T1$ relaxation sequence once a laser is started to polarize the NV spin to the excited state then turned off and wait by varying the dark time τ. Without a π-pulse, the relaxation time is detected from the excited state, on the other hand, a π-pulse is applied to measure T_1 relaxation from the ground state. (b) The Bloch sphere demonstrates the vector of T_1 relaxation decays respected to different initial states along the longitudinal axis (c) The T_1 relaxation result of an ensemble NV diamond as a function of time-varying and fit by $Ae^{-(\tau/T_1)^n} + B$.

fluorescence decay intensity is plotted as a function of dark time τ. In Fig. 3.4(b), interpretation of T_1 relaxation by the Bloch sphere as the magnitude decay of the Bloch vector thus, T_1 is also called longitudinal relaxation time.

In the NV relaxometry, the T_1 relaxation decays very fast due to the magnetic noise in the transverse projection $B_\perp$.[6] Because the lifetime of the $m_s = \pm 1$ states is shorter than $m_s = 0$ state[86] thus when the perpendicular magnetic is applied along one NV axis, the mixed state of $m_s = 0$ and $m_s = \pm 1$ is induced and causes the short lifetime in total, which is detectable by the changing fluorescence intensity.[62] One of the most interesting experiments for ultrahigh frequency magnetic noise detection by the quantum NV center has been the first report in the 2013s by S.Steinert et al,.[87] The GHz range magnetic noise produced by a Gd^{3+} paramagnetic ion is detected by NV spin relaxometry. The rapid relaxation of T_1 is caused by the $S = 7/2$ of Gd^{3+} spin, which produces fluctuating magnetic noise and dominates the NV spins without microwave excitation. The fluctuating magnetic noise creates a random magnetic vector to the environment with zero average field $\langle B \rangle = 0$ however, its root mean square ($B_{rms} = \sqrt{\langle B^2 \rangle}$) will not be zero statistically ($B_{rms} > 0$). This fluctuation spectral density denoted as a spin bath which

can be characterized by a Lorentzian spectrum as follows[88]

$$S(\omega) = \frac{B_{rms}^2}{\pi} \frac{\tau_c}{1 + \omega^2 \tau_c^2} \tag{3.10}$$

Where τ_c is the correlation period of the spin under the fluctuation, and ω is the Larmor frequency of the NV spins.[74] Consequently, the interaction between NV spins and the environment under the magnetic fluctuation performs the relaxation rate $\Gamma = 1/T_1$ is expressed by[87]

$$\Gamma_{tot} = \Gamma_{int} + \Gamma_{env} \tag{3.11}$$

The Γ_{tot} is denoted as the total T_1 relaxation rate measured by the NV center, Γ_{int} is the intrinsic relaxation rate of NV spins without noise, and Γ_{env} is relaxation rate under the magnetic noise in the environment.

Chapter 4

Superparamagnetic Particles and Magnetic Fluctuation

Magnetic particles are magnetic materials that display magnetic properties and can induce their magnetization under the bias of an external magnetic field. Magnetic particles exhibit different magnetic properties depending on their size and temperature. Typically, the magnetic particles are classified into the nanoscale, called magnetic nanoparticle (MNP) that have been fascinating and support various applications in medicine, biology, and materials science. For example, MNPs are used to improve the contrast of the magnetic resonance imaging (MRI) yielding higher-quality images for medical examination.[89,90] MNPs were used to destroy tumors and cancer cells in human bodies by converting magnetic to thermal energy to heat target cancer cells, known as magnetic hyperthermia (MHT).[91] The most utilized magnetic materials are considered in terms of toxicity in biocompatibility, such as iron, nickel, cobalt, and magnetite. However, cobalt and nickel are sensitive to oxygen ions which can be oxidized into toxic.[89,92,93] To avoid the toxicity, the promising iron oxidized nanomaterials namely magnetite (Fe_3O_4) and hematite (Fe_2O_3) are replaced materials for nanomagnetic particles of *in vivo* and *in vitro* biomedical applications.[94,95]

MNP behaviors have been considered with many parameters to support each application such as shape, surface, particle size, temperature, and magnetization. Especially, in the ferromagnetic property, exhibit identical magnetic dipole directions under an external magnetic field and become a magnet afterward. Frenkel and Dorfman[96] were the first researchers who predicted

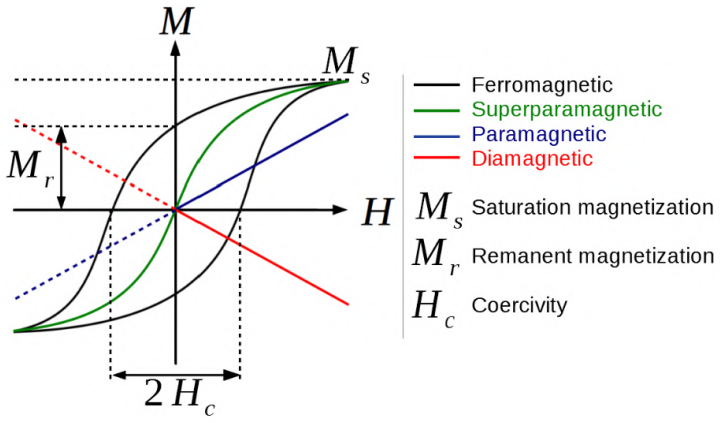

Figure 4.1: The hysteresis of the magnetic materials. Superparamagnetic properties can be saturated as well as ferromagnetic materials but, do not exhibit coercivity and remanent magnetization after demagnetization. (adapted from A. Ven al ainen [99]).

that the existing single domain would be in the ferromagnetic materials below a critical particle size, which was estimated by Kittel[97] afterward. Moreover, the transition of magnetic behavior into superparamagnetism occurred above a certain temperature, known as Curie temperature, as well as the magnetic B-H curve, which is larger than bulk ferromagnetic materials.[98]

The superparamagnetic material is in the middle between paramagnetic and ferromagnetic materials. Unlike the ferromagnetic substances, superparamagnetic domains align corresponding to the increasing external magnetic fields until the saturation quickly but, after reversing the external magnetic direction to zero, the magnetic domains are demagnetized to zero at the same point without the coercivity[99] (See Fig. 4.1).

4.1 Néel Relaxation

When the size of a ferromagnetic component is decreased below the critical size, it becomes a single-domain particle and exhibits superparamagnetic properties (See Fig. 4.2(a)). Typically, magnetic domains are dominated by magnetic anisotropy where the preferred magnetization alignment, called the easy axis, is in the domains, which makes the two stable domain directions and is separated by an energy barrier E_a. In the case of a single domain, the energy barrier reduces as it is proportional to the particle size, therefore, the thermal energy overcomes the energy barrier and randomly flips the domain

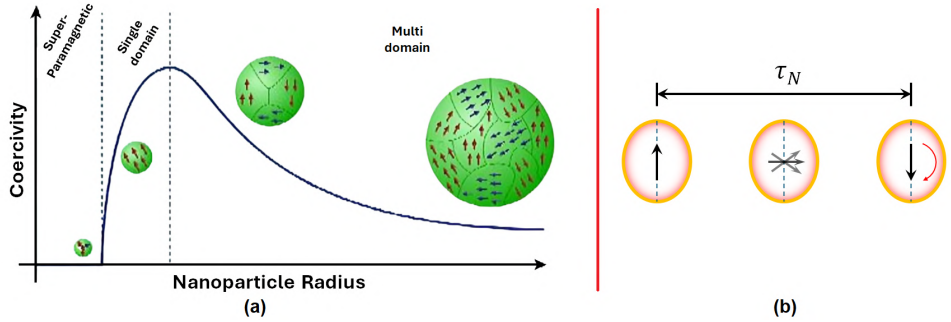

Figure 4.2: (a) Schematic representation of the coercivity-particle relations. The single-domain magnetic particles exhibit the superparamagnetic property with zero coercivity after removing the magnetic excitation. (adapted from A. Akbarzadeh et al, [89]). (b) The Néel relaxation mechanism - the magnetic moment orientation rotates inside the particle core along the easy axis (dash line) and causes magnetic fluctuation during domain flipping.

orientations for a short period. This thermal fluctuation over the magnetic moments in superparamagnetic materials causes magnetic fluctuation in the environment. The period of magnetic moment flipping between two orientations in the stationary particles is called the Néel relaxation τ_N, originating from Louis Néel who first developed the theory to explain the time-dependent magnetic behavior.[100]

The Néel relaxation time is associated with the temperature and anisotropy barrier of the particle in terms of thermal energy to anisotropy energy ratio.[91], can be expressed by a Néel-Arrhenius law[101]

$$\tau_N = \tau_0 \exp\left(\frac{KV}{k_B T}\right) \tag{4.1}$$

Where τ_0 is the attempt period of a superparamagnetic particle. For example, Fe_3O_4, which is in the range of 10^{-7}-10^{-13} s depending on the particle properties[102]. V is the superparamagnetic particle volume, and K is its anisotropy constant. Thus, the energy barrier is denoted as $E_a = KV$. k_B is the Boltzmann constant, and T is the temperature in Kelvin.

4.2 Relaxometry Imaging

The NV spin relaxation has been utilized as a sophisticated technique in quantum sensing for mapping and imaging several physical properties and applications such as magnetic noise[76,81–88], charge conversion in diamonds[103], temperature and thermal imaging[76,80,104], and conductivity images from the Johnson noise.[84,105,106] These can be done by detecting the relaxation times of the spin dynamic of the most promising materials like NV center in a diamond. The relaxation times of the NV spins can correctly obtain high spatial resolution due to the atomic scale of NV defects resolved data acquisition of physical interaction to support various applications. The magnetic noise from superparamagnetic particles has been studied by mapping the relaxometry image of T_1 relaxation time and dephasing image by T_2 coherent time researched by D. Schmid-Lorch et al.[107] The spin noise of a 10 nm Fe_3O_4 particles mixed with sodium silicate then attached to the tip of a small cantilever and the experiment setup is a commercial AFM (See Fig. 4.3(a)). An ensemble bulk diamond with shallow NV around 5 nm under its surface was used to sense the relaxation and dephasing images. The spatial images of the magnetic fluctuation while approaching the cantilever were recorded pixel by pixel corresponding to the fluorescence intensity of the NV center. The magnetic fluctuation, which is perpendicular to the NV axis $B_\perp$ and its frequency is close to the resonance frequency of the NV,[76,104] induces the decreasing NV spin lifetime, causing the fluorescence decay quickly in Fig. 4.3(c)-(e).

Another similar research is to study the magnetic images using nanodiamond attached to an AFM tip as a quantum sensing probe. This technique allows us to investigate the magnetic noise from aggregates of maghemite (Fe_2O_3) nanoparticles. J.-P. Tetienne et al[104], demonstrated a scanning ensemble NV probe from type-Ib nanodiamonds which is capable of observing topography, fluorescence, thermal, and NV spin relaxation images from magnetic particles. In Fig. 4.4(d), The decay T_1 relaxations related to each Zeeman splitting are evident that the most aggregates produced the largest local static magnetic field and magnetic fluctuation dominated the NV spins as the fastest T_1 relaxation compared with each other position.

Although the sensitivity of the ensemble NV is smaller than the single NV, which is caused by shorter intrinsic relaxation time, the signal-to-noise ratio enlarges by $\sqrt{N}$, where N is the number of NV.[19] When the ensemble NV diamond is polarized, all four orientations of NV are excited and produce the background fluorescence to the system. To reduce the background inten-

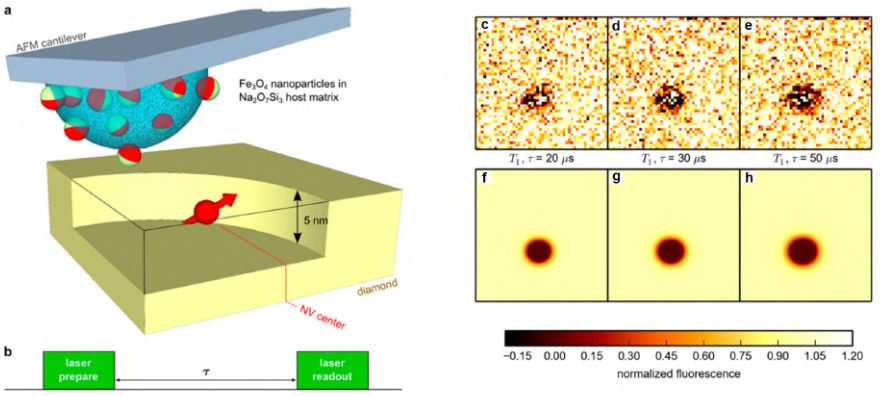

Figure 4.3: (a) The experimental setup with AFM cantilever and Fe_3O_4 particles while engaging to a shallow NV diamond. (b) the pulse sequence for T_1 relaxometry imaging. (c)-(e) Relaxometry images result by fixing each dark time τ. (f)-(h) Simulated imaging respected to (c)-(e), respectively. (adapted from D. Schmid-Lorch et al. [107])

sity, the external magnetic field is applied along one of the NV axes to select only one quantitation NV axis. When the π-pulse of the transition between $m_s = 0$ to $m_s = -1$ or $m_s = +1$ is selected, we can apply this π-pulse with the T_1 relaxation sequence as the reference (See Fig. 4.5(d)).

This technique allows us to measure the decay time only on the chosen NV axis and reduces other fluorescence backgrounds from other NV orientations, this technique is called common-mode rejection[60,108].

One of the interesting applications for biosensing focuses on paramagnetic detection in biocells by using widefield NV relaxation imaging as demonstrated in Fig. 4.5. Suvechhya et al, utilized the common-mode rejection of T_1 relaxation imaging to observe the relaxation rate induced by Fe^{3+} from cytochrome C (Cyt-C) nanoclusters involved electron transport chain within mitochondria[109]. This experiment exposed insight into the behavior of Cyt-C proteins at various concentrations. The relaxation contrast is extracted from the subtraction of T_1 with π-pulse ($T_{1,\pi}$) from the T_1 without π-pulse ($T_{1,0}$) and dividing them with the sum of these two values.

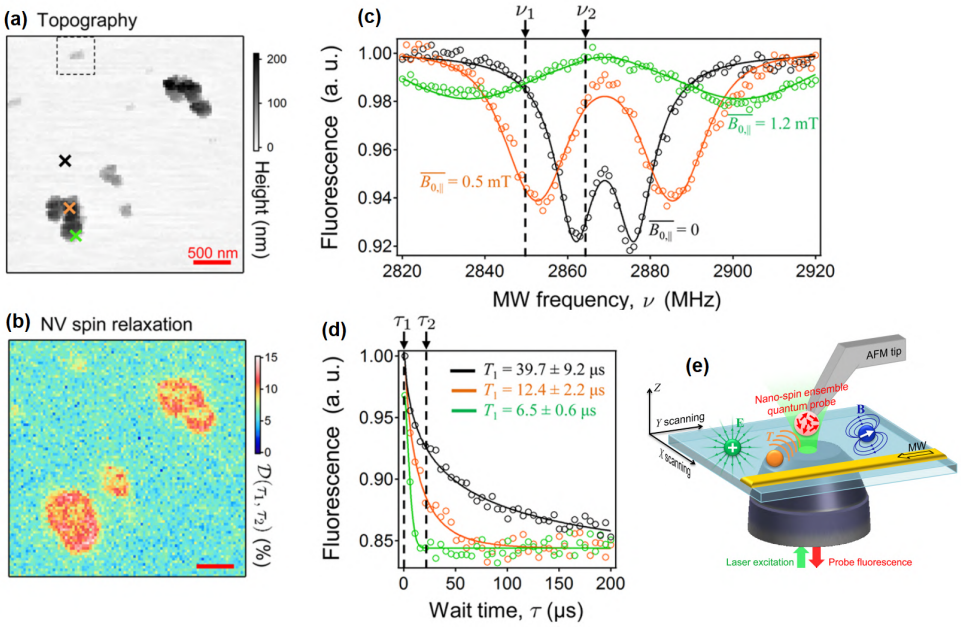

Figure 4.4: (a) The AFM topography image of aggregates of maghemite nanoparticles on a glass coverslip. (b) Relaxometry image corresponding to the different wait times τ. (c) ODMR spectrum at three different positions related to the markers in (a). (d) T_1 relaxation curves corresponding to the positions in (a). (d) AFM probe with nano ensemble NV diamond used to measure T_1 relaxation image. (adapted from J.-P. Tetienne et al. [104])

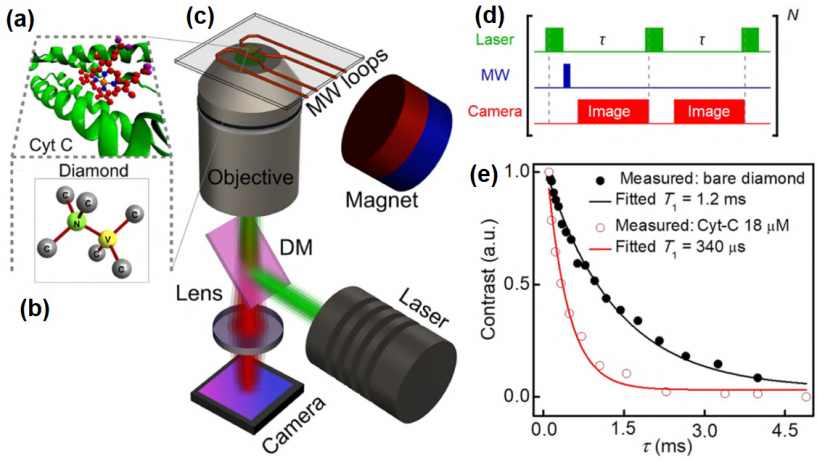

Figure 4.5: (a) Molecular structure of Cyt-C protein. (b) NV defect structure in the diamond lattice was used to measure the relaxation rate. (c) The experimental setup of widefield NV relaxation imaging. (d) A schematic of the common-mode rejection pulse sequence of T_1 relaxation imaging. The contrast relaxation $T_1 = (T_{1,0} - T_{1,\pi})/(T_{1,0} + T_{1,\pi})$. (e) Relaxation curve from a bare diamond (black filled circles) and decay with Cyt-C solution on a diamond (open red circles). (adapted from Suvechhya et al. [109])

Chapter 5

Sample Preparation and Experimental Setup

5.1 NV Ensemble Diamond and Fabrication

In this work, we used an electronic grade CVD diamond with [100] crystal orientation from Element Six. The diamond was cut into $2.0\times2.0\times0.5$ mm^3 and polished until having 50 μm thickness. The high-purity diamond contains an initial nitrogen concentration N < 1 ppb which is very low sensitivity from a magnetic imaging experiment. Thus, the diamond was then implanted with $^{14}N^{+}$ ions at 30 keV of energy and fluence of 1×10^{12} ions/cm^2 with tilt angle of 7°. After implantation, the annealing treatment is usually provided in vacuum condition at a temperature between 800° C and 1000° C for a few hours so that the NV defects are formed.[110] The NV concentration is optimized when the annealing temperature reaches 875° C and becomes stable even when the temperature increases over 1000° C for 2 hours[13]. In this work, the diamond sample was annealed at 900° C for 1 hour by using an infrared heater. The carbon recoils created the vacancies during the implantation process[111] and the NV layer was estimated at an average depth of 40±10 nm via simulation of Stopping and Range of Ions in Matter (SRIM)[112].

The diamond was cleaned in acid with a 1:3 ratio of HNO_3 and H_2SO_4 at the temperature of 220° C for 30 minutes and finally rinsed with pure water. To support the micro-scale experiments, the diamond was cut into several triangular prism shapes by laser cutting at SYNTEK Co. Ltd, as shown in Fig. 5.2.

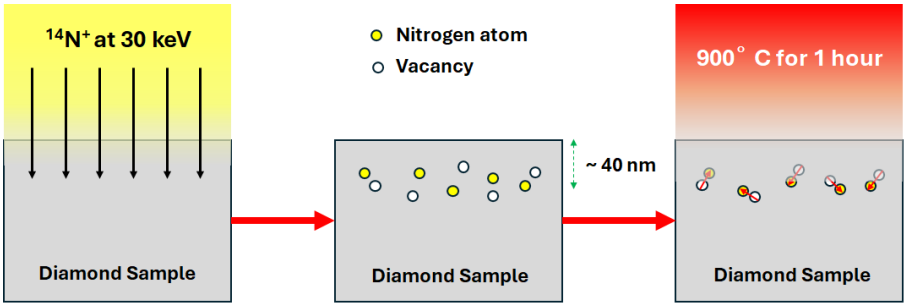

Figure 5.1: Schematic of nitrogen implantation and annealing to form the Nitrogen-vacancy defect in a diamond.

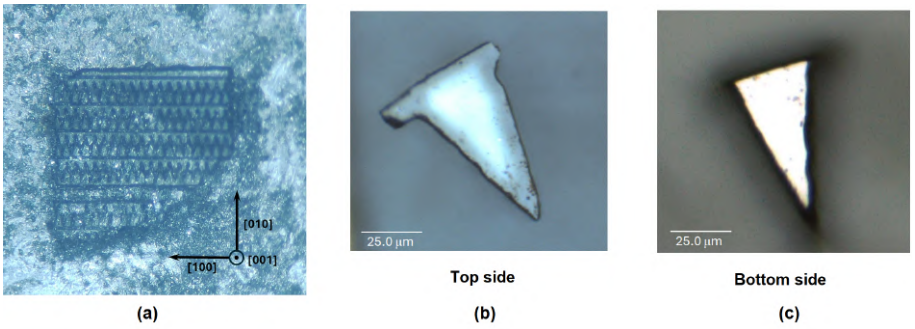

Figure 5.2: (a) Electronic grade diamond was cut with triangular prism shape and cleaned by acetone in this experiment. (b) The top side presents one triangular-shaped diamond. (c) One triangular-shaped diamond is presented by the bottom side which is determined as the NV layer side.

A prism-shaped diamond sample is placed in an ABS plastic chip tray using a shaped needle. The diamond sample is cleaned up by using a micro drop of acetone. The sticky melted plastic will pick up the residual contaminants from the diamond surface.

According to the SRIM simulation, the NV layer is formed at a depth up to 70 nm below the diamond-implanted surface. There are various parameters we put into the SRIM to calculate the NV concentration and depth of NV defects, for example, the diamond density of 3.52 g/cm^3, implantation energy of 30 keV, the implanted ion tilt angle of 7° to keep away from ion channeling[113], and displacement energy of 35.7 eV for the electron incident respected to [100] crystal direction[114,115] of the diamond sample used in this work. Therefore, the average maximum concentration is located around 40 nm beneath the diamond's surface.

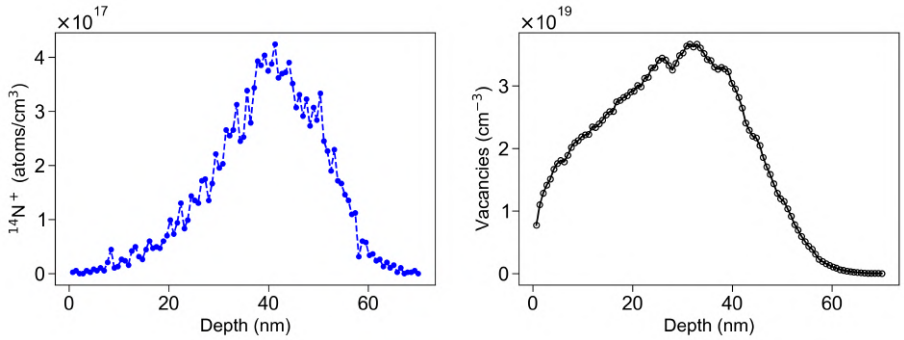

Figure 5.3: (Left) Nitrogen ion distribution in atoms per cm^3 as a function of implantation depth. (Right) Vacancy distribution calculated from the carbon recoils as a function of implantation depth.

At the average depth of 40 nm, the nitrogen concentration is 4.24×10^{17} atoms/cm^3 obtained from nitrogen ion distribution multiplied by dose in SRIM and corresponding to 1 ppm per 1.76×10^{17} atoms/cm^3 for impurity in a diamond.[13] The highest concentration of the NV^- calculated from 7% yield of nitrogen concentration at 30 keV of implantation energy.[116] Therefore, our diamond sample contains NV centers of about 2.97×10^{16} NV/cm^3 or approximately 0.17 ppm of the NV^- concentration.

5.2 Superparamagnetic Core-Shell Particle

In this research, we used a core-shell superparamagnetic particle from JSR Life Sciences Company and the product name is Magnosphere MS300/Carboxyl. The particle bead is made of a non-magnetic core covered with magnetite nanoparticle, Fe_3O_4 as a shell, which is designed for high-purity bioseparation. The particle surface was covered with a hydrophilic polymer carboxyl group which prevented ligands combination for chemistry and biology applications. These superparamagnetic particles are uniform particle size with 3 μm diameter. The magnetic layer thickness was estimated by pixel-per-distance ratio comparison with ImageJ software. The scale obtained by pixel measurement could be compared with the known distance of the image such as the particle diameter (See Fig. 5.4(a)). In this work, the thickness of the magnetite layer is approximately 200 - 300 nm from its surface.

In Fig. 5.5, the particles were diluted with deionized (DI) water by particle liquid volume and DI water ratio of 1:100. Then, particles were transferred to a glass slide using a micro-pipette by 5 μL. Although the par-

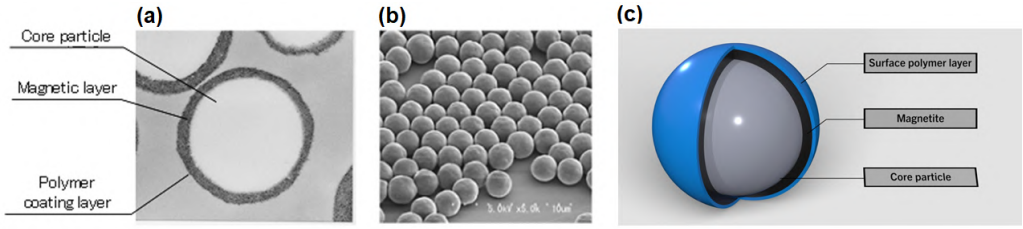

Figure 5.4: (a) TEM image of a cross-section of a Magnosphere superparamagnetic particle which consists of core particle, magnetic layer from Fe_3O_4, and a thin polymer layer. (b) SEM image shows Magnosphere aggregate with uniform size. (c) Schematic 3D model of Magnosphere superparamagnetic particle. (adapted from https://www.jsrlifesciences.com/en/research-reagents-ivd/magnosphere)

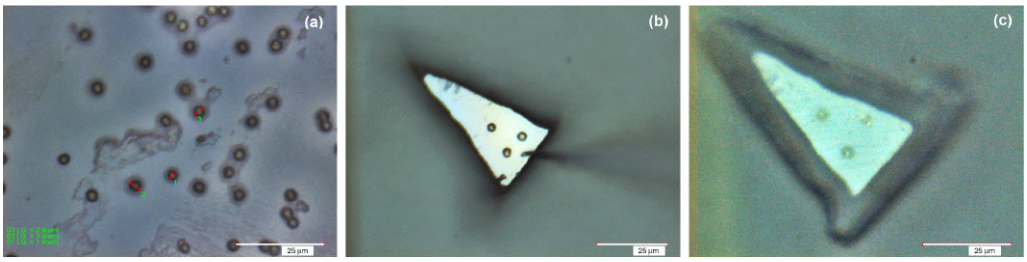

Figure 5.5: (a) Optical image of core shell magnetic particles after dropping on the glass slide. The particle size is estimated with some particle examples before selection. (b) 3 particles were picked up and placed on the NV layer side of the ensemble diamond sample. (c) The diamond sample with 3 particles flipping upside down and the optical image exposed 3 particles under the NV layer of the diamond sample while focusing downward.

ticles are uniform, the particle diameter was estimated before selection when the DI water evaporated completely. In Fig. 5.6, a PCB microstrip line was prepared to place the diamond sample. A gold antenna with 25 μm diameter was connected to deliver the microwave excitation. An approximately 3 μm diameter particle was picked up by using a microscope with micromanipulator arm and a very sharpened tungsten wire, whose diameter is smaller than the particle size. We chose 3 candidate particles that were placed on the NV layer side of the diamond sample and then, flipped the diamond upside down to support a home-built confocal upright microscope. The diamond sample was pushed by about 45° angle which aligns to the external magnetic vector.

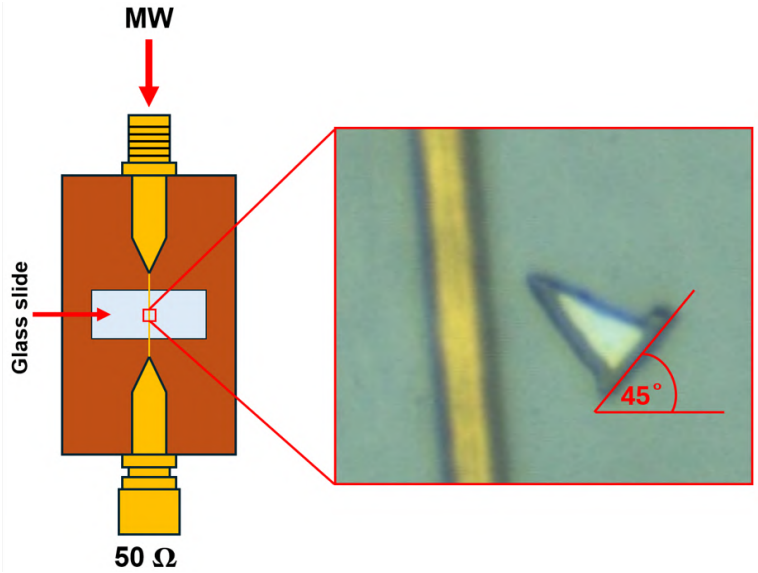

Figure 5.6: The Schematic of PCB microstrip line with the location of the diamond sample and its 45 ° angle.

5.3 Confocal Microscope

When the thicker sample is observed, the light may not be passed through the sample uniformly in the general microscope. The objective lens will not provide enough focus range for various depths of the sample. This causes non-focusing images and insufficient resolution areas in a conventional microscope. The confocal microscope is built to solve this issue which is based on the equivalent focusing spot during confocal scanning.[117] This research was carried out on a home-built confocal microscope which is commonly used to observe the electron spin resonance of the NV center. The diamond with the superparamagnetic sample was placed on the XY stage and then, tie up with plastic screws for each corner. The 532 nm laser source illuminates, and then it is filtered to 0.5 mW by a neutral density (ND) filter before reflecting at mirrors to AOM, which controls the pulse width of laser excitation. A pinhole is placed to filter spatially varying intensity noise out of the Gaussian beam laser. After that, the green laser was delivered to reflect at the dichroic mirror by fiber optics, and then its beam was controlled by the Galvo scanner. The beam expander is provided based on the Keplerian design where two collimated lenses ($f = 200$ mm and $f = 100$ mm) are separated by the distance which is equal to the sum of their focal lengths as demonstrated in Fig. 5.7 so that the laser beam waist is expanded by 2:1 ratio.

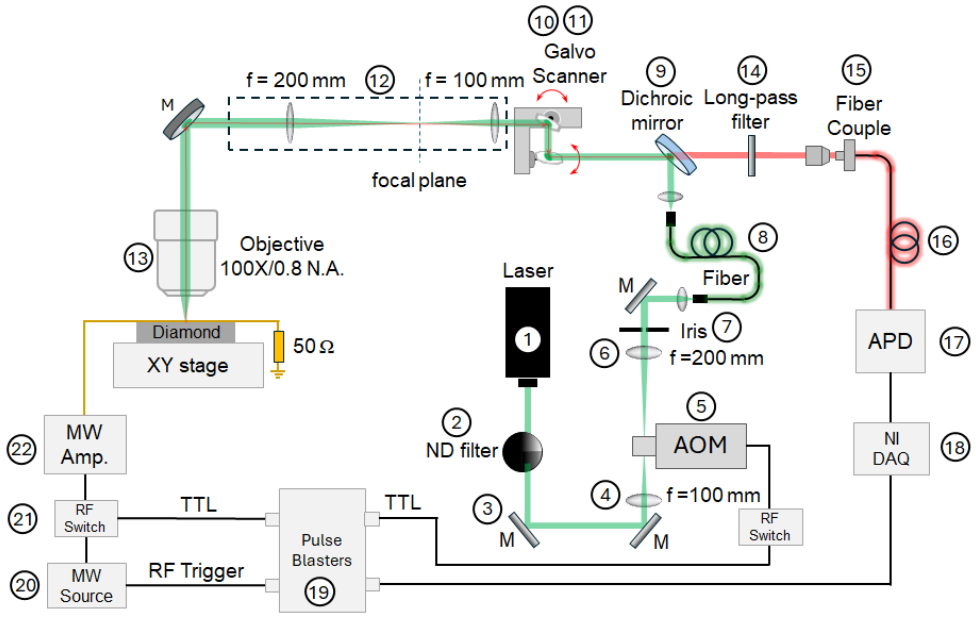

Figure 5.7: Experimental setup of a home-built confocal microscope.

The expanded laser beam is focused on the diamond sample by the 100× objective lens with N.A. = 0.8.

The fluorescence emission from the sample is filtered by a long-pass filter, and then focused on a fiber couple before recording by APD as a photon counter. A microwave source can be triggered to start sweeping frequencies during ESR measuring. The microwave is switched by the RF switch, which is controlled by a transistor-transistor logic (TTL) signal and used to control AOM. The microwave is delivered to the microstrip line on the sample holder by a gold wire as a microwave antenna. The 50 Ω terminator is connected at the end of the antenna to match the impedance and protect the extremely high incident power reflection back to the microwave amplifier. Finally, a stepper motor controls the focus range in the Z-axis. In Fig. 5.7, the list of numbers is represented by the model and serial number of each equipment used in this research, (See Appendix I).

5.4 Spin Relaxation Experiment and Imaging

Using a home-built confocal microscope in Fig. 5.8, T_1 relaxation image is measured pixel by pixel when moving the laser spot to the diamond sample. When the sample holder is placed and fixed at the XY stage, we can

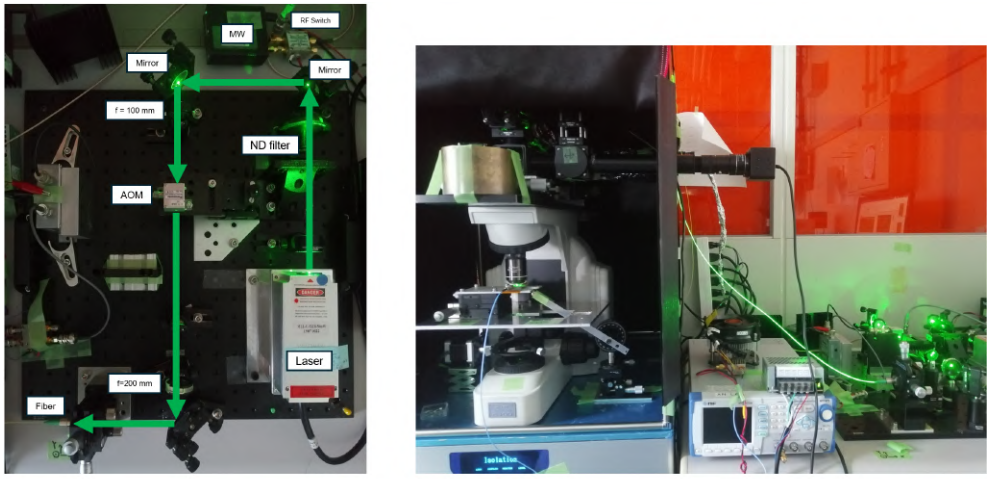

Figure 5.8: Photograph of (a) the Optical system of the confocal microscope. (b) the scanning confocal microscope.

control the focus range with a stepper motor on the Z-axis. For each position, The NV spin could have a different T_1 relaxation, which has a different fluorescence decay for each dark time τ. Consequently, by fixing τ, we can extract the different contrasts of the spin relaxation at each pixel concerning the particle position. The scanning area is determined related to the pixel sizes of the relaxation image. However, larger pixel sizes need a longer time. Each pixel from the spin relaxation image experiment is normalized with the initial polarization counter in which the most spin population is $m_s = 0$. Therefore, each pixel value is in between $0 - 1$. We designed the scanning confocal microscope to start from the pixel of $X = 0, Y = 0$. When the pixel on the X-axis is finished, the pixel on the Y-axis is increased. Until the final pixel is reached, the image is reconstructed and displayed as shown in Fig. 5.9. This system is capable of measuring ESR and mapping. For the local magnetic investigation, the external magnetic field is applied parallelly to one of the NV qualitative axes.

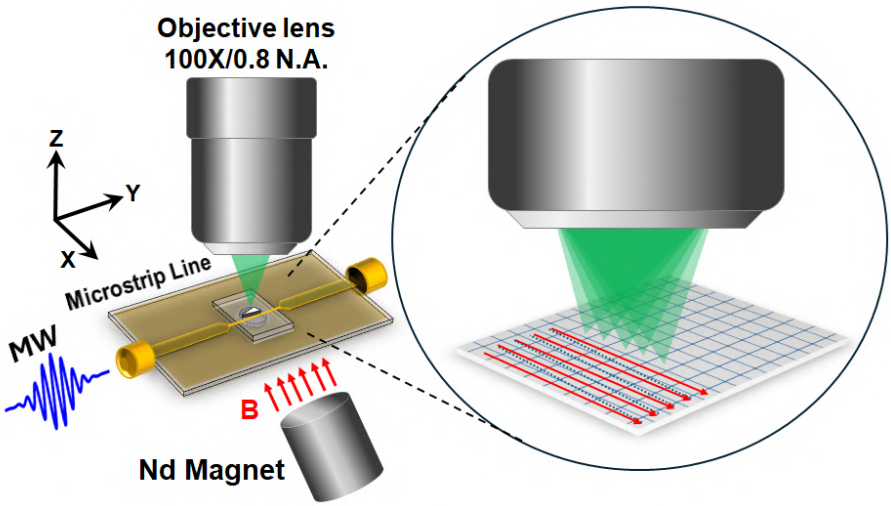

Figure 5.9: The scanning confocal microscope measurement by focusing at each position and reconstructing the spin relaxation image. The neodymium magnet (Nd magnet) is aligned along the NV axis to make a parallel field in the ESR experiment.

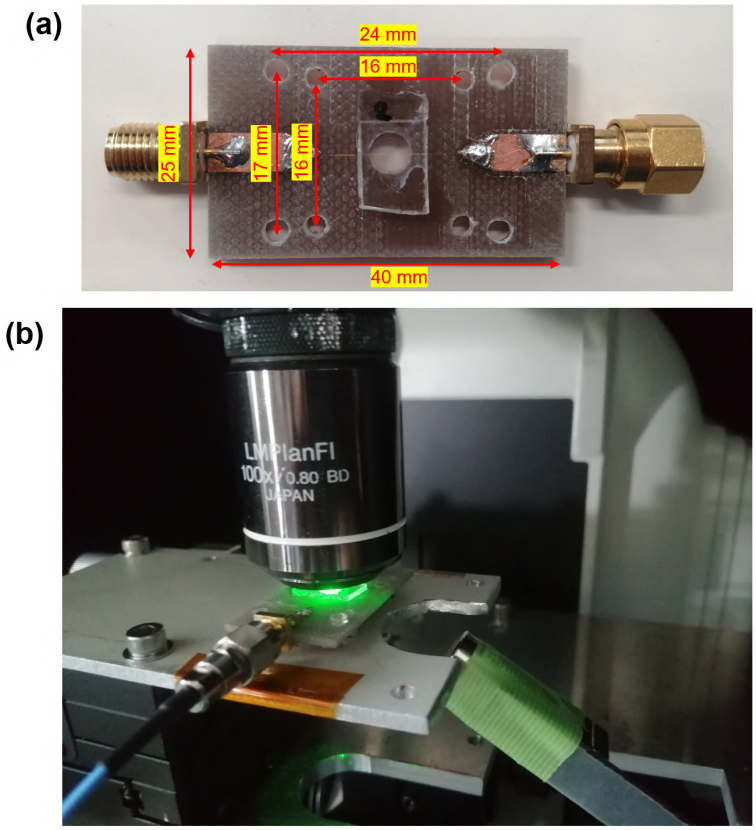

Figure 5.10: Photograph of (a) microstrip line design diagram. (b) experiment at the scanning confocal microscope with a uniform external magnetic field from Nd magnet.

Chapter 6

Relaxation Image of Conducting Magnetite Layer on a Superparamagnetic Core-Shell Particle

6.1 Experiment

A superparamagnetic core-shell particle is picked up by a sharpened tungsten wire and placed on the NV layer side of the ensemble diamond. We prepared three particles with uniform diameters of 3 μm to ensure that each particle touched the diamond. The core-shell particles were coated with a polymer which is a sticky surface. Therefore, the particles can attach to the diamond surface easily. The diamond sample with three particles was flipped by sharpened tungsten through a micromanipulator arm and became stable as well as a tripod (See Fig. 6.1). In the optical image, we can observe three particles through the diamond sample. The laser is moved to focus at the particle which we want to measure (See Fig. 6.2). In this case, we observed that the core-shell particle can produce fluorescence emission which helps us to monitor the position of each particle under the diamond sample (See Fig. 6.3).

The sample holder was placed on the home-built confocal microscope. The sample stage can be moved to adjust the position. Three core-shell particles are observed through the objective lens where the position of each

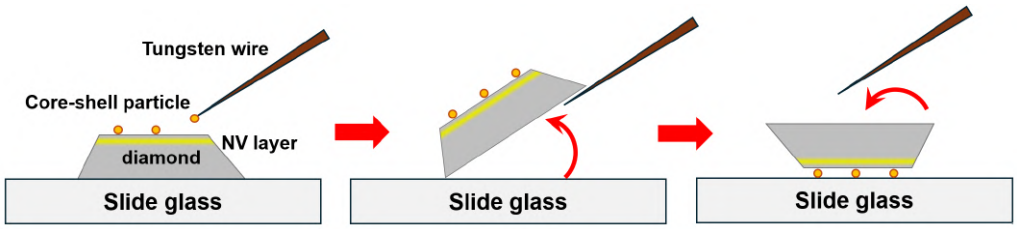

Figure 6.1: The cartoon demonstrates a core-shell particle is picked up by a sharpened tungsten wire and placed on the diamond by the NV layer side. A sharpened tungsten wire can be inserted under the diamond sample then flip the diamond upside down.

particle is fixed. The green laser points to the center of the target particle. The recorded fluorescence emission confirms the location of each particle under the diamond sample. After correct focus including the NV ensemble layer, the fluorescence between NV and particles was combined as the total fluorescence intensity results as shown in Fig. 6.3. In this case, we can estimate the center position of the target particle. The pulse sequence for T_1 relaxation was set, and the measurement was started after the sample stage was stable. The sample per point was 20,000 and the average measurement was 4 times. The time consumption for each experiment depends on these two parameters.

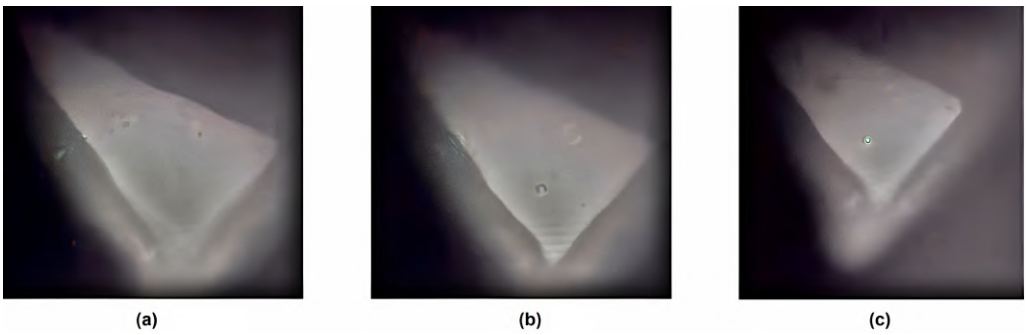

Figure 6.2: (a) The optical image shows two particles under the diamond sample in the black color. (b) After the correct focus, another particle is revealed. (c) The green laser was positioned at the center of the particle before the experiment started.

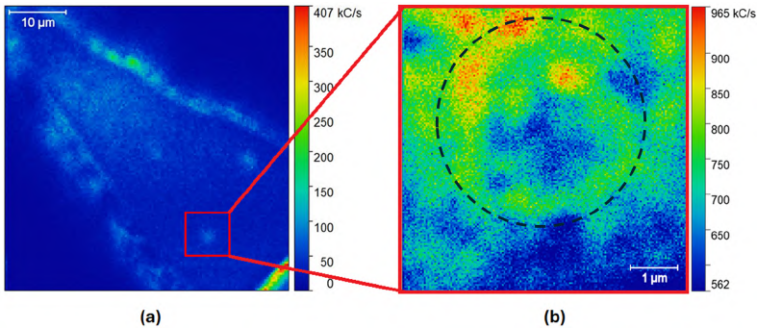

Figure 6.3: (a) The fluorescence intensity recorded when the pinhole focusing under the diamond sample. The fluorescence emitting from the core-shell particles can be observed. (b) After the focus adjustment, the fluorescence of ensemble NV and core-shell particle was recorded.

6.2 Results and Discussion

6.2.1 Spin Relaxation affected by superparamagnetic core-shell particle

After the position was estimated, we expected that this position was the nearest position between the magnetite and the NV layer. From the experiment, the T_1 relaxation time was recorded at three different positions. The first position is at the center of the particle, the second one is at the edge of the particle and the third one is outside of the particle which contains only ensemble NV centers. The dark time was set between 0 - 10 ms. The T_1 relaxation decays of these three positions are plotted as shown in Fig. 6.4(a). The red dot refers to the far position which means the intrinsic NV relaxation time. The green dot is on the border of the PL of the magnetic particle, the blue dot is at the center of the magnetic particle, and the T_1 relaxation results are fitted by $Ae^{-(\tau/T_1)^n} + B$. The highest contrast of intensities is calculated from the intensity subtraction between the NV without particle and the NV at the center of the particle as shown in Fig. 6.4(b). From these results, we can design the fixed τ fluorescence intensity of T_1 relaxation time for each position of the interesting area.

From the result in Fig. 6.4(b), it was demonstrated that the maximum contrast between particle and diamond sample is at $\tau \sim 200$ μs. Therefore, we created a fix $\tau = 200$ μs pulse sequence as shown in Fig. 6.5(a), to measure PL intensities pixel by pixel to map the contrast image of the influence of magnetic noise. The fluorescence image in Fig. 6.5(b) is comparable with

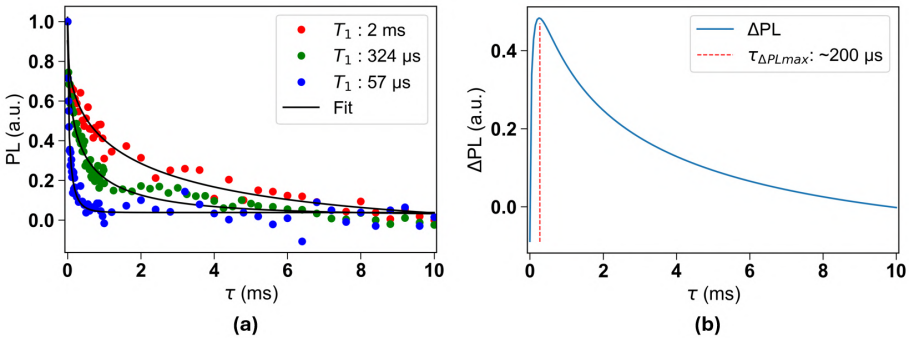

Figure 6.4: (a) T_1 relaxation time recorded between three positions are compared. The solid lines fit the exponential function of relaxation decay time. (b) The different fluorescence intensity from (a). The maximum contrast is $\tau \sim 200$ μs.

the contrast image in Fig. 6.5(c). The normalized date was calculated by the ratio of the signal divided by the reference pixel by pixel. This image contains 40×40 pixels and the area of measurement is 6 μm × 6 μm. The obvious image result revealed the effect of magnetic fluctuation on the NV spins even without an external magnetic field. The line-cut profile was measured along the horizontal line of the relaxation contrast image in Fig. 6.6(a). The results are demonstrated in Fig. 6.6(b). This profile was measured by using the Gwyddion software. The red dashed line was used to mark the direction of the line-cut while the T_1 relaxation time was demonstrated in Fig. 6.6(c) which corresponds to the line-cut profile.

To estimate the magnetic fluctuation from this effect, we assume the cubic shape of a superparamagnetic particle covering a core-shell particle by an arbitrary size and is supposed to touch the diamond at the nearest position. Based on the Eq. 3.11, we extracted the intrinsic NV relaxation time and converted it to the intrinsic rate, $\Gamma_{int} = 1/\mathrm{T}_{1,NV} = 500$ Hz, which is attributed to the thermal equilibrium decay source in the diamond structure, such as P1 center and ^{13}C isotopes. This intrinsic rate is considered to a constant value for the ensemble NV diamond in this experiment. For Γ_{env}, denoted as the decoherence T_1 due to the magnetic noise generated from superparamagnetic particles at the nearest position. The spectral density of the magnetic noise is considered then, Γ_{env} can be calculated by[76]

$$\Gamma_{env} = \gamma^2 \left\langle B_\perp^2 \right\rangle \int S(\omega, T, E_a) F(\omega) d\omega \tag{6.1}$$

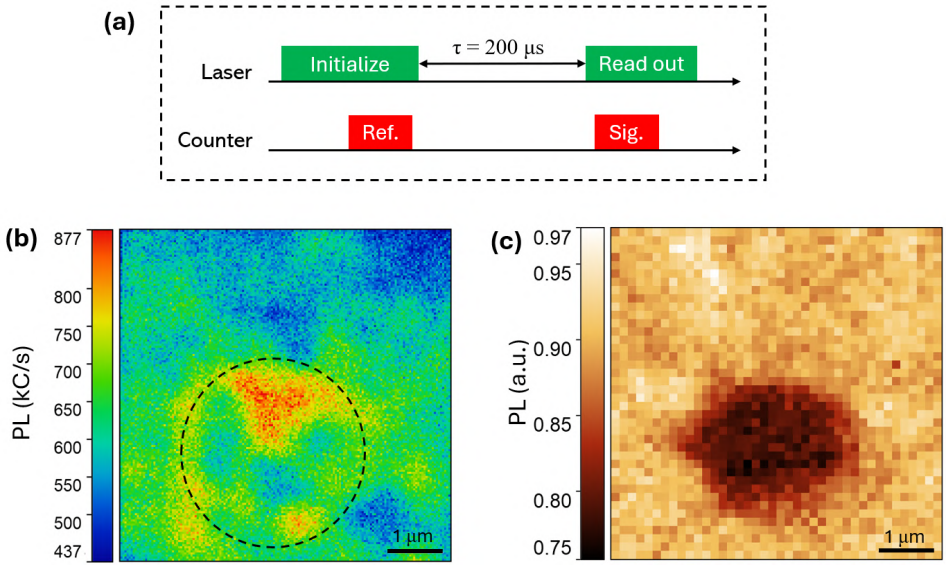

Figure 6.5: (a) The fixed pulse sequence utilized to measure the fluorescence decays respected to the maximum contrast in Fig. 6.4(b). (b) The fluorescence emits from the target core-shell particle. (c) The T_1 contrast image corresponded to the fluorescence image(b).

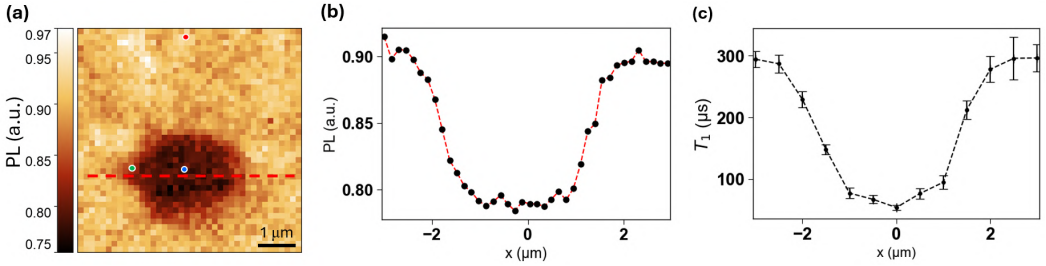

Figure 6.6: (a) Relaxation image with a red dashed line for marking the line cut of measurement along the horizontal axis. The red, green, and blue markers represent the NV area, border of contrast, and center positions of measurement from Fig. 6.4(a), respectively. (b) Line-cut profile of the fluorescence contrast of T_1 measurement respected to (a). (c) T_1 relaxation time recorded along the line-cut respected to (a).

Where ω is the frequency of the filter function spectrum, T is the temperature in Kevin, E_a is the anisotropy barrier energy of the superparamagnetic particle, and $F(\omega)$ is the filter function of T_1 relaxometry. In Eq. 3.10, the correlation period τ_c is approximated to the Néel relaxation time of a single domain in the superparamagnetic particle, $\tau_c \approx \tau_N$.

For this reason, the relaxation rate can be modified as[81,83]

$$\Gamma_{tot} = \Gamma_{int} + 3\gamma^2 \left\langle B_\perp^2 \right\rangle \frac{\tau_N}{1 + \omega_{NV}^2 \tau_N^2} \tag{6.2}$$

Consider the average magnetic field $\langle B_\perp^2 \rangle$, the random fluctuation components over the surface, and project into the transverse direction at the position, in this case, we extracted $r = 33$ nm as the average depth of the NV layer from the surface and assumed the polymer thickness is 5 nm. Thus, we can obtain:[83,107]

$$\left\langle B_\perp^2 \right\rangle = \frac{m^2 \mu_0^2}{48\pi^2} \left[\frac{5 - 3cos^2(\theta)}{r^6} \right] \tag{6.3}$$

Where θ is the angle between the NV axis and vector of the distance between the particle and the NV layer, in this case, the diamond sample is (100)-orientation therefore, θ is 54.74° to the diamond surface.[88] We denoted m as the magnetic moment of the magnetite magnetic materials. Consider $\rho_\mu = 5.4{\times}10^{28}\ \mu_B/m^3$ is the magnetic density of magnetite[107], where μ_B is Bohr magneton. In this case, we assume the volume of a superparamagnetic particle V at the nearest position, consequently, the magnetic moment is $m = \rho_\mu V$.

From the Eq. 4.1, the attempt period is from the assumption from the appropriate range as described in Sec.4.1. In this case, we choose $\tau_0 = 1{\times}10^{-13}$ s which makes the Néel relaxation time in the window of the spectral density. Many parameters affect the anisotropy constant of the magnetite, such as particle size[118] and annealing temperature. The wide range of the anisotropy constant is 1.1 to $17.0{\times}10^4$J/m^3 depending on the effects of heating temperature.[119] However, the effective anisotropy constant for commonly magnetite $K = 1.4{\times}10^4$J/m^3. Since the temperature is constant at room temperature, the anisotropy energy per the thermal energy ratio is assumed to be constant with $KV > k_B T$ in our case.

From this calculation, we found that the particle volume is $6.8{\times}10^{-25}$ m^3 which corresponded to a spherical volume with 11 nm diameter and the magnetic fluctuation $\sqrt{\langle B_\perp^2 \rangle} \approx 0.43$ mT.

The magnetization of a magnetic particle is composed of static and fluctuating components which can be expressed as

$$B_p = B_0 + \delta B \tag{6.4}$$

Where B_p is the total magnetization of the particle, B_0 is the static field that senses the spin resonance of the NV spins and can be measured by ODMR, and δB is the fluctuating field that can be detected by the spin relaxation time of the NV centers.

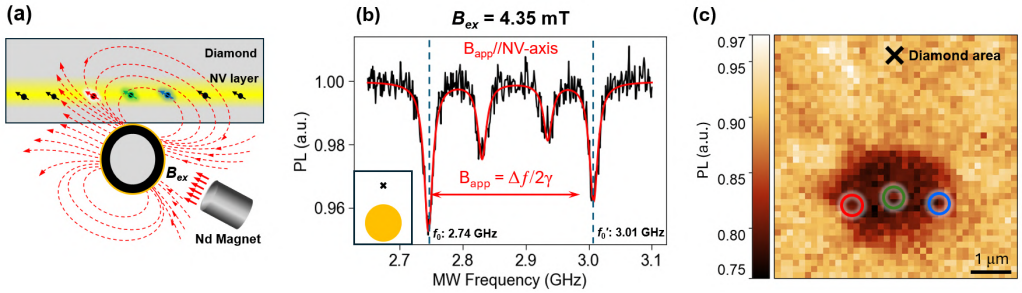

Figure 6.7: (a) A schematic drawing of the applied static field for the local B-H curve measurement. (b) ODMR spectrum was measured outside the particle (yellow circle denoted as the particle in the inset), denoted as NV area (cross mark in the inset). (c) The T_1 contrast image with the color circles corresponding to the measurement positions.

6.2.2 Magnetic Stray Field Mapping of Superparamagnetic Core-Shell Particle

In the presence of an external static field, we applied the external field using a neodymium magnet aligned along one of the NV axis with $\pm 1^\circ$ difference. An aligned bias field clearly provides the four depths of the ODMR in an ODMR measurement. Therefore, we can measure the magnetic field applied to the particle and the additional field that is produced from the particle, which may be constructive or destructive to the applied field. In Fig. 6.7(a), a schematic drawing of the external static field for B-H curve measurement. The external magnetic field from an Nd magnet was projected along one of the NV axes. From these results, we discovered that the magnet stray field is aligned with the applied field and is constructed mostly on the left side of the particle compared with the ODMR in the diamond area (cross mark in the inset) in Fig. 6.7(b). The ODMR spectrum in Fig. 6.7(b) is from the external field of 4.35 mT. The aligned field provides the resonance frequency of $f_0 = 2.74$ GHz and $f_0' = 3.01$ GHz, and the other two degenerated off-axis resonance frequencies. However, the stray field destroys the applied

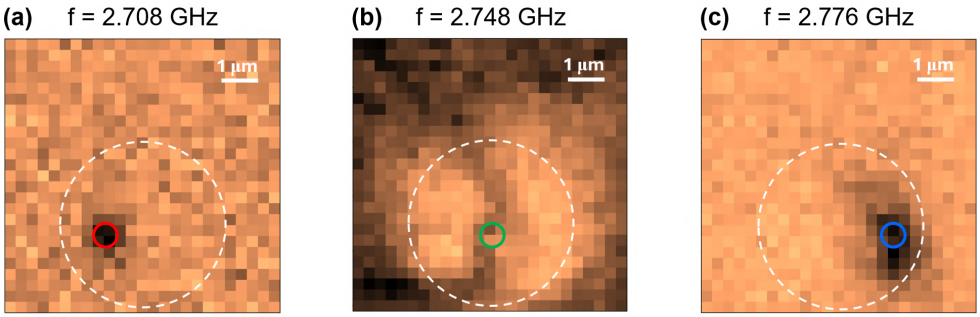

Figure 6.8: ODMR with frequency dependent-mapping . (a) The mapping image at the microwave frequency of 2.708 GHz is the most splitting corresponding to the left side of the particle. (b) The mapping image at the microwave frequency of 2.748 GHz with a small contrast at the center. (c) The mapping with 2.776 GHz reveals the right side of the particle with the most reverse stray field which reduces the Zeeman splitting.

field on the right side of the particle, while the stray field provided a slight effect at the center of the particle. Each position of the measurement points corresponds to the T_1 contrast image as demonstrated in Fig. 6.7(c).

To prove the position dependence of the stray field, we measured the ODMR with position dependence around the particle. The ODMR results were mapped with 25×25 pixels because each position was mapped several times with a sufficient average for noise cancellation. In Fig. 6.8(a), at the lowest frequency splitting, the left side of the particle displays weak fluorescence, which describes that the local field of the particle projects reverse to the applied field and causes the total magnetic field to decrease. Fig. 6.8(b) shows the microwave excitation at 2.748 GHz which exposes the small contrast fluorescence intensity at the center of the particle revealing that the stray field at the center is weak and is close to the applied field, evidence from the fluorescence contrast is the same as outer area. and the last result in Fig. 6.8(c) shows the right side of the particle, which provides the reverse magnetic field against the applied field, causing the reduced frequency splitting on the ODMR results.

From this evidence, we can measure the magnetic response by ODMR as shown in Fig. 6.9(a) and the yellow shade is the resonance frequencies of m_s = -1 as shown in Fig. 6.9(b). The black dashed line is the Lorentzian fit to determine the shifted frequencies (f_1, f_2, and f_3), compared to the frequency outside the particle, f_0. By focusing on the most largest splitting on the left side of the particle, we subtracted the measured magnetic field from this with

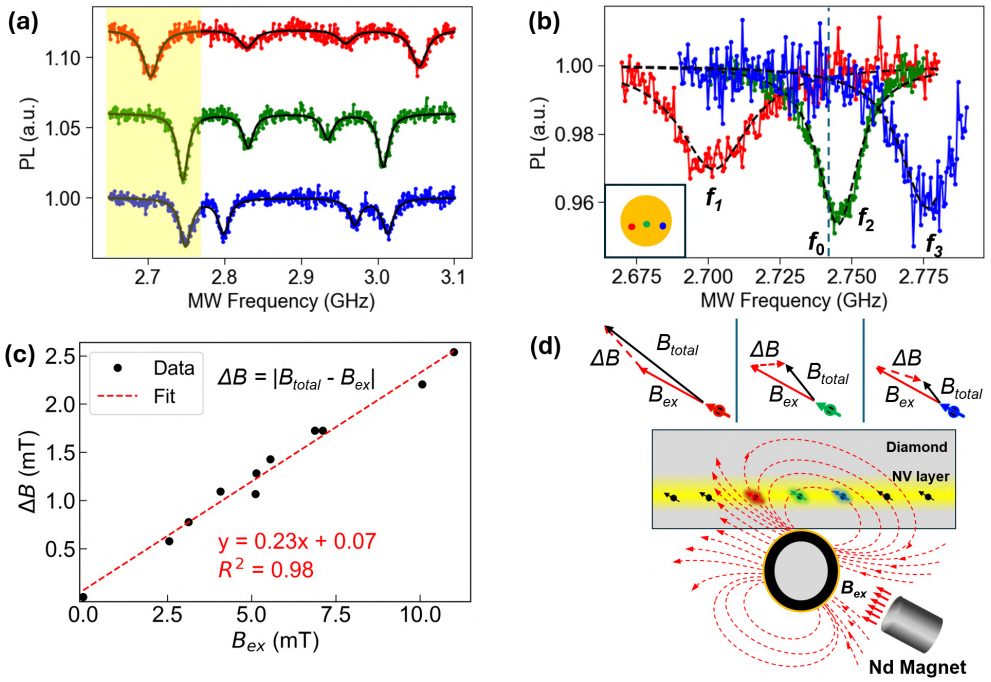

Figure 6.9: (a) The ODMR with Zeeman splitting results measured at a different position of the particle, left side (red), center (green), and right side (blue). (b) The ODMR results at the specific range of microwave, corresponding to the yellow shade in (a), shows the different frequency splitting agree with the position of left side, center, and right side of the particle, (color-mark in the inset) respectively. (c) The ΔB dependence in the external applied field B_{ex} measured at the left side of the particle. The linear fitting reveals the slope which implies the magnetic B-H curve of the particle. (d) The schematic illustrates the magnetic local field under the static magnetic field at a different position of particle based on ODMR results.

the applied field measured at the bare NV. The result is shown in Fig. 6.9(c). The linear fitting provided the slope that implied the magnetic B-H curve of the particle in this experiment, which implies that the magnetic susceptibility $\chi = 0.23$, which is dimensionless. The constant of 0.07 implies that the slope passes through almost the origin of a superparamagnetic B-H curve. In Fig. 6.9(d), the schematic is provided from the experimental results of the ODMR with frequency-dependent mapping, which illustrates the magnetic local field under the static field bias with constructive and destructive magnetic fields from three positions of the core-shell particle.

6.2.3 The Magnetic Fluctuation Model in Ensemble NV Center in Diamond

In this model, we assume that 8 magnetic particles produce the magnetic noise distribution to a single NV in 8 directions from the top view of the 1^{st} layer (see Fig. 6.10(a)). A single NV is placed at the center with 8 particles surrounding it. Each direction has at least 4 particles separated by 15 nm from the center of the particle. In this case, we demonstrated the distance effect on the mean-square magnetic fluctuation, which is a significant factor for the relaxation. We assume that all particles are 11 nm in diameter. From these parameters, the total relaxation rate is from the accumulation of each magnetic noise interacting with each single NV in the laser excitation. The total relaxation rate of all 8 directions is

$$\Gamma_{total} = \Gamma_{center} + 8\Gamma_{NS} + 8\Gamma_{WE} + 8\Gamma_{NWSE} + 8\Gamma_{NESW} \tag{6.5}$$

In Fig. 6.10(a), the nearest particle that has the most fluctuation to a single NV is provided Γ_{center}. Where N, S, W, and E are represented in the directions of north, south, west, and east, respectively.

The laser spot for this experiment depends on the wavelength (λ) and the numerical aperture (NA) of the objective lens. In this case, $\lambda = 532$ nm and NA is 0.8 therefore, the laser spot is expressed by

$$D = 1.22\frac{\lambda}{NA} \tag{6.6}$$

In this experiment, the diameter of the laser spot D is about 800 nm. We used the diameter of the laser spot to estimate the intensity of the laser excitation, which is explained by the Gaussian distribution (see Fig. 6.10(b)). We assumed that a single NV in the laser spot is separated by 100 nm and the radius from the core-shell particle is 1.5 μm. as depicted in Fig. 6.10(c). Thus, the distance from each single nanoparticle can be calculated individually. Consequently, each single NV provides a T_1 distribution in 8 directions and is contributed by adding the Gaussian distribution of laser excitation intensity by

$$I(r) = I_0 e^{\left(\frac{-2r^2}{\sigma^2}\right)} \tag{6.7}$$

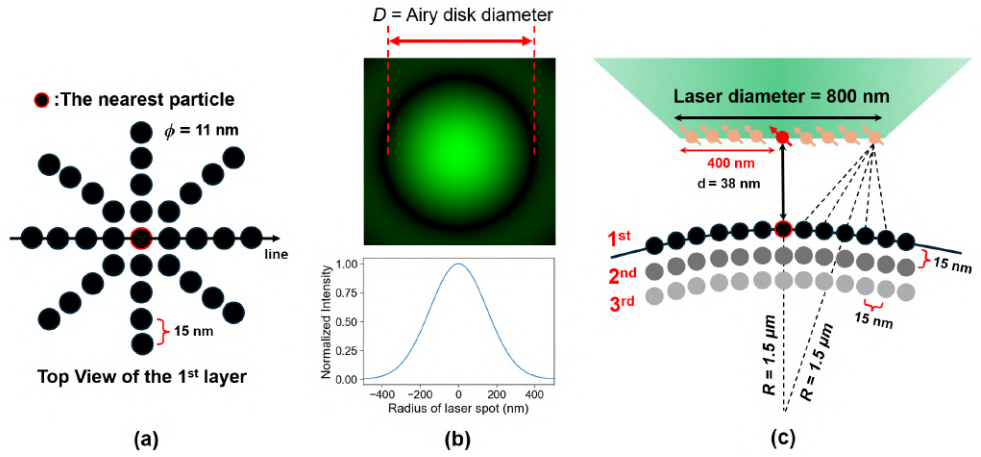

Figure 6.10: (a) Determination of particles distribute the magnetic fluctuation to a single NV in 8 directions. The center particle is the nearest particle at the center position. (b) Laser intensity after objective lens which is approximated by the Gaussian distribution plot. (c) 2D modeling of magnetic fluctuation of each single NV. The population for the average relaxation time is related to the laser intensity.

The laser intensity is approximated by the Gaussian distribution in Eq. 6.7 where $I(r)$ is a function of the radius distance from the center of the laser spot, $I_0 = 1$ for the normalization intensity and $\sigma = \frac{0.84\lambda}{2NA}$ is the Gaussian RMS width (standard deviation).

Consequently, the relaxation time average from each side in two dimensions (Fig. 6.10(a)) will be multiplied by the Gaussian distribution for each single NV along the radius of the laser spot (0 to 400 nm). In this method, we can deviate the population of relaxation time, which is related to the laser intensity during measurement, as follows.

$$T_{1,total} = \frac{T_{1,center} + e^{\left(\frac{-2\times 100nm^2}{\sigma^2}\right)} \times 8 \times T_{1,100nm} + e^{\left(\frac{-2\times 200nm^2}{\sigma^2}\right)} \times 8 \times T_{1,200nm} + \cdots}{33} \tag{6.8}$$

From the radius of the laser spot, there are 4 single NV in 8 directions from a single NV at the center, and the total number of NV is 33.

To estimate the contributed $\sqrt{\langle B_\perp^2 \rangle}$, we suppose the nearest single NV with a single domain from a superparamagnetic nanoparticle at the contact

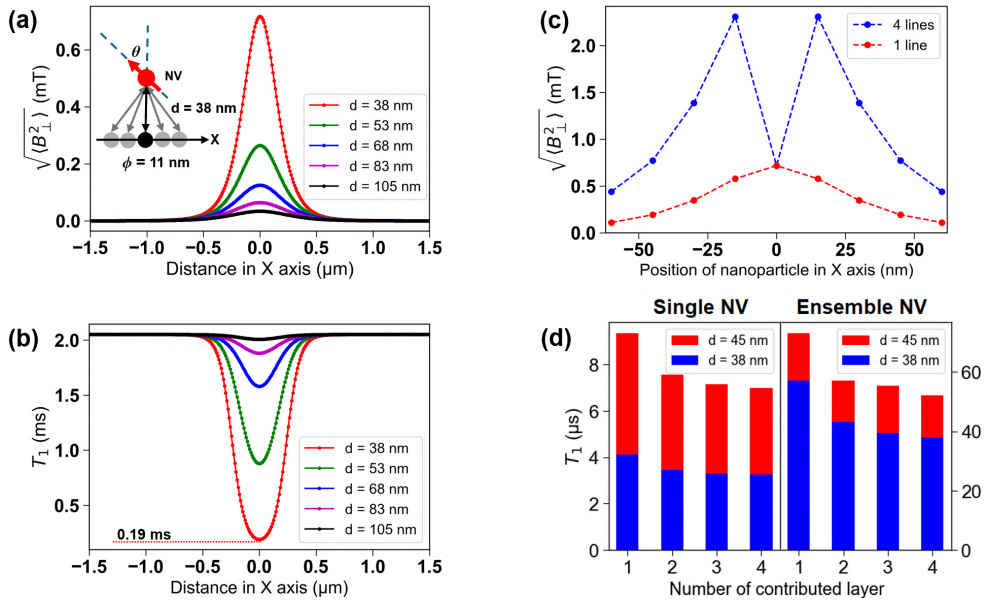

Figure 6.11: (a) A simulation of $\sqrt{\langle B_\perp^2 \rangle}$ measured by a signle NV as a function of distance x. By varying distance of NV to the particles. (b) Position-dependent of T_1 relaxation time corresponding to (a). (c) The $\sqrt{\langle B_\perp^2 \rangle}$ contributions in 1 line and 4 lines for 1^{st} layer as shown in Fig. 6.10(a) as a function of distance from the center position. (d) The estimated T_1 relaxation time for single and ensemble NV condition with an increasing number of contributed layer.

position as shown in Fig. 6.11(a). From Eq. 6.3, we can compute the $\sqrt{\langle B_\perp^2 \rangle}$ with variation of r = 38 - 105 nm. The value of $\sqrt{\langle B_\perp^2 \rangle}$ was estimated as a function of distance in x direction. Meanwhile, the value of T_1 can be evaluated from Eq. 6.2 as depicted in Fig. 6.11(b). The $\sqrt{\langle B_\perp^2 \rangle}$ from the total of 9 particles contributions from 1 line is compared with additional 3 different lines from 8 directions of particle contributions (4 lines for the total) as plotted in Fig. 6.11(c). Finally, the T_1 relaxation time is calculated in case of r = 38 and 45 nm as shown in Fig. 6.11(d). In a single NV model, the obtained T_1 value from the total 4 layer contribution is smaller than the experimental results. Meanwhile, the ensemble NV model, within the 800 nm laser spot with its Gaussian intensity distribution, provides longer T_1 contributions, ($T_1 \approx 52$ μs), at r = 45 nm which is comparable with the experimental result at the center of the particle, $T_1 = 57$ μs.

6.3 Conclusion

In conclusion, we demonstrated the T_1 spin relaxation observed from the superparamagnetic core-shell particle which is commonly used in the magnetic immunoassays. The magnetite with superparamagnetic properties generates magnetic fluctuation noise in the environment under the zero field bias from the external magnetic fields. The ensemble NV center in the diamond sample is utilized to investigate this fluctuation noise which is sensitive to the relaxation of the electron-phonon population in the NV centers. The different fluorescence contrast from the relaxation decays determined the location of the magnetic fluctuation which corresponds to magnetic particle size. Meanwhile, the root mean square of the magnetic noise has been estimated, corresponding to the nanoscale for a single domain of the superparamagnetic particle. The static field of the particle has been analyzed by applying the external constant magnetic field. The stray field reveals the position-dependent local magnetic field and is measured by the NV center. These results lead to the measurable magnetization of the core-shell particle and allow us to measure the magnetic B-H curve of the magnetic particle.

Chapter 7

Summary and Future Works

7.1 Summary

In this dissertation, we focused on the technical development of magnetic noise estimation generated from a superparamagnetic core-shell particle and measurement of the magnetic B-H curve based on magnetic sensing in the NV center in diamonds. The diamond sample with (100) orientation is implanted by $^{14}N^{+}$ ions at 30 keV of implantation energy. The NV density is estimated by using SRIM and the concentration is approximately 0.17 ppm for the ensemble NV sample. The diamond sample was cut by laser for a microscale target sample. The superparamagnetic core-shell particle is a commercial product that is commonly used in a laboratory for bioseparation. The magnetic fluctuation generated by the superparamagnetic particle induces the electron-phonon coupling in the NV center to become the equilibrium state faster than usual conditions. This is caused by the particle size being smaller than the critical size and the magnetic domain is evaluated to be a single domain.

Domain formation in a superparamagnetic particle is related to its volume which leads to the reduction in anisotropy energy and allows the thermal energy to dominate the domain as it can be explained by Néel relaxation, which plays the most important factor for T_1 relaxation time. The thickness of the magnetite layer is estimated by pixel measurement while the particle size is hidden in the aggregate of the materials. We employed the NV center to measure the T_1 relaxation time under zero magnetic bias. The shortened T_1 reveals the effect of magnetic fluctuation surrounding the particle surface

which allows us to map the particle feature. We estimated the magnetic fluctuation based on the average root mean square magnetic field perpendicular field which corresponds to the nanoparticle size and anisotropy constant of the magnetite at room temperature. Due to the static and fluctuating magnetic fields included in the particle, the fluctuating field can affect the relaxation time of the NV center. For this reason, we managed to apply a constant magnetic field which can be measured by ODMR through the diamond sample.

The magnetic stray field is proportional to the applied magnetic field at the particle as we varied the applied magnetic field. The magnetization of the particle is obtained by subtracting from the applied magnetic field. The slope of the magnetization and applied magnetic field relation is interpreted as the magnetic B-H curve of the particle. The ESR position dependence was measured and demonstrated the local magnetic field response over the particle shape, which exposed the different stray fields under the magnetic bias condition.

7.2 Future Works

The outstanding in this research is evaluated to better understand the magnetic noise produced into the environment and can be detected by the NV centers in a diamond. The applications of superparamagnetic particles are still interesting in biomedical science while lacking quantum magnetic sensing, especially in NMR applications. Our experiment will be introduced to NMR imaging based on the characteristics of NV centers in diamonds. As well as micro MRI applications, our research will pave to way to the study of magnetic noise and its effect on MRI and analytical applications suggesting the integration of technology between science and engineering.

This is just only the first step of the advantage of quantum sensing in the NV center. The high sensitivity of NV spin sensing potential will be considered as a replacement for a shallow NV diamond. We can expect that the NV defect sensing from our experiment will be employed to study other noise from tiny and specific materials. Moreover, it is better to become part of a useful method to extend the broadening of quantum technology, including improving human life.

Appendix A

Magnetic Property of The Magnetic Particle

A.1 Magnetization Curve

The magnetic beads were separated from the liquid solution by a centrifuge, drained of the liquid solution by a pipette, and dried for 10 minutes. The dried particles were measured in weight (33 mg) and covered with a plastic wrap. The hysteresis curves were measured by SQUID at 5 K and 300 K. The experimental results show the superparamagnetic property at 300 K with nearly zero coercivity force as depicted inset in Fig. A.1(a). The results in Fig. A.1(b) show the hysteresis of ferromagnetic property at low temperatures due to the block state when the temperature is below the blocking temperature compared with high temperature at 300 K.

The M-H curve fits with the Langevin function as follows[120]

$$M = M_s \left[Coth \left(\frac{\mu H}{k_B T} - \frac{k_B T}{\mu H} \right) \right] \tag{A.1}$$

Where k_B is the Boltzmann constant, T is the temperature in Kevin, M_s is the saturated magnetization of the sample, μ is the magnetic moment of the particle, and H is the magnetic applied field.

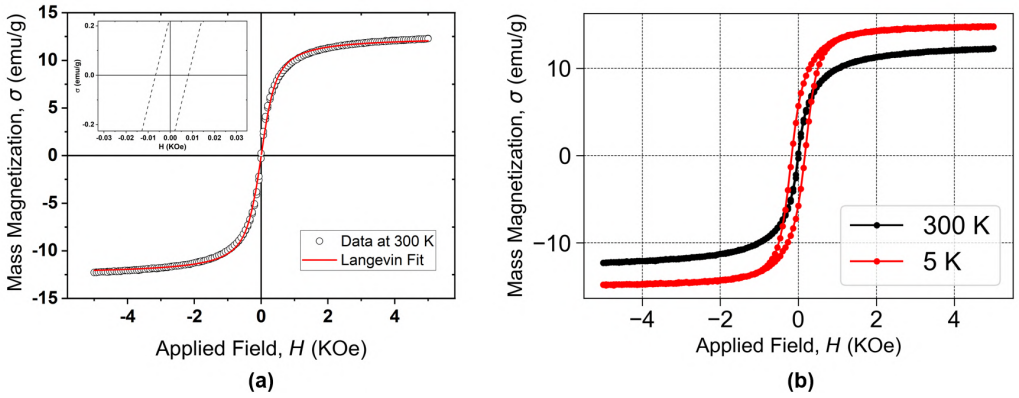

Figure A.1: (a) M-H Curve from -0.5 T to 0.5 T (a) at 300 K and (b) comparison of at 5 K and 300 K.

The nearly zero coercivity force is probably due to the residual magnetic field from the superconducting magnet or magnetic background in the system. The different saturated magnetization in Fig. A.1(b) occurred because the sample shows the ferromagnetic property below the blocking temperature (5 K) and becomes a superparamagnetic property above the blocking temperature at room temperature (300 K) and including paramagnetic impurity.

A.2 Temperature-Dependent Magnetization

In this experiment, the particles are cooled from room temperature to 5 K without a magnetic field, known as zero-field cooling. At 5 K, a constant magnetic field of 100 Oe is applied to measure the magnetization during the increase of temperature up to 300 K. To estimate the susceptibility, we assume the majority of particle mass is from magnetite, Fe3O4, which has a density of 5.17 g/cm^3. The susceptibility, χ, is plotted in Fig. A.2 which is called the ZFC curve. When the temperature reaches 300 K, the temperature is reduced to 2 K under the same constant magnetic field, resulting in the FC curve (see Fig. A.2).

In Fig. A.2, the magnetic moment of the particle is frozen at a temperature below 75 K, which is the blocking temperature (T_B). In this state, the anisotropic directions are blocked state. At a temperature above TB, the magnetic domains start moving in anisotropic directions, while the magnetic moments decrease during the increasing temperature. The ZFC curve indicated that the magnetic particles change from ferromagnetism at the blocked state to superparamagnetic behavior.

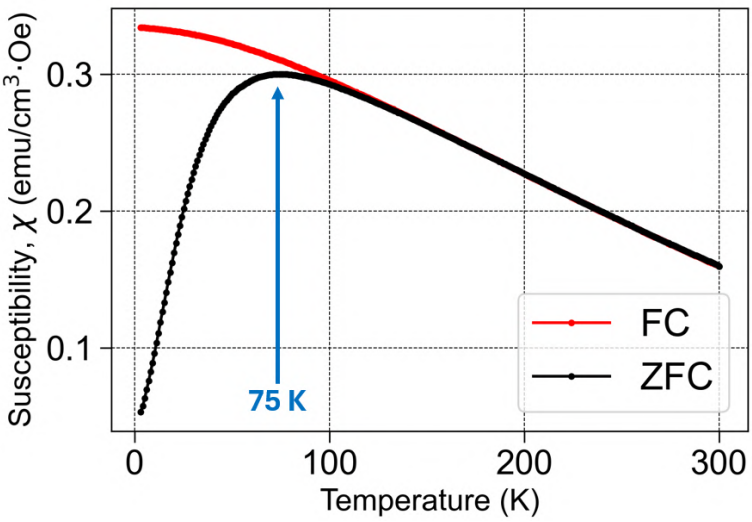

Figure A.2: (a) The zero-field cooled (ZFC) and field-cooled (FC) magnetization curves.

For the FC curve, the magnetic moments are not constant below the TB, suggesting that interparticle interactions can be neglected.

Appendix B

SEM and EDS Results

The SEM and EDS (Scanning Electron Microscope and Energy Dispersive X-ray Spectroscopy) is a sophisticated tool for analyzing that integrate structural and compositional materials analysis. The sample was bombarded with focused electron beams to obtain the spatial components of elements involving the identification of the line spectrum analysis. In this study, we spared the magnetic particles on the slide glass with the DI water by the ratio of 1:1. After drying at room temperature, the sample was coated by Pt/Pd sputtering for 10 nm making the grounding substrate to avoid the charging in the sample, which reduces the image quality. In Fig. B.1(a) and (b), the SEM image of the magnetic beads was observed with the backscattered electron image and the secondary electron image, respectively. The shape of the particles is not uniform and perfectly spherical shape.

For the EDS experiment, the acceleration voltage of 30 KeV is applied to the primary electron beam. The EDS exposed the atomic components in the sample. In Fig. B.2, we demonstrated the SEM image of the spread magnetic particles and picked up one of the particles to measure with four different positions. The element spectra shown in Fig. B.3 for each position reveal the presence of C, O, Fe, Si, Pt, and Pd from sputtering. The weight and atomic percentage corresponding to Fig. B.2 and Fig. B.3 are shown in Table. B.1.

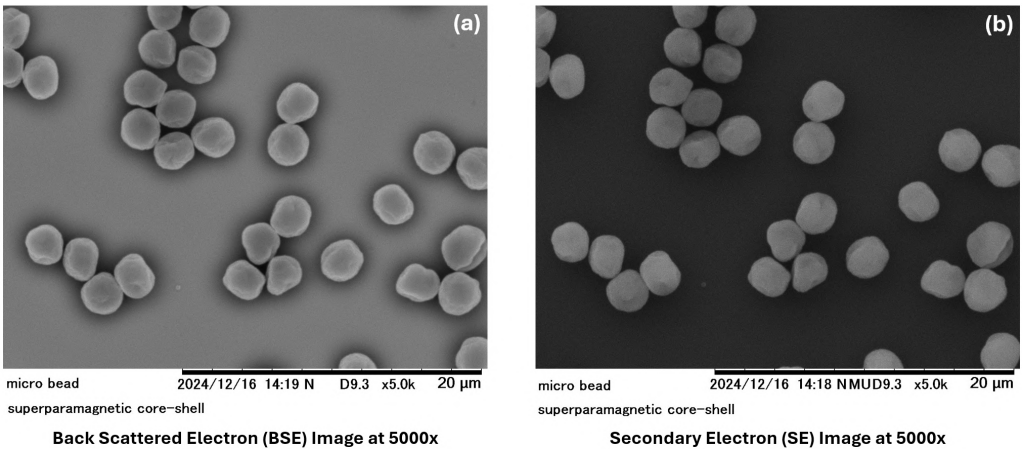

Figure B.1: (a) The backscattered electron image and (b) the secondary electron image of the magnetic beads with incident electron energy at 15 KeV.

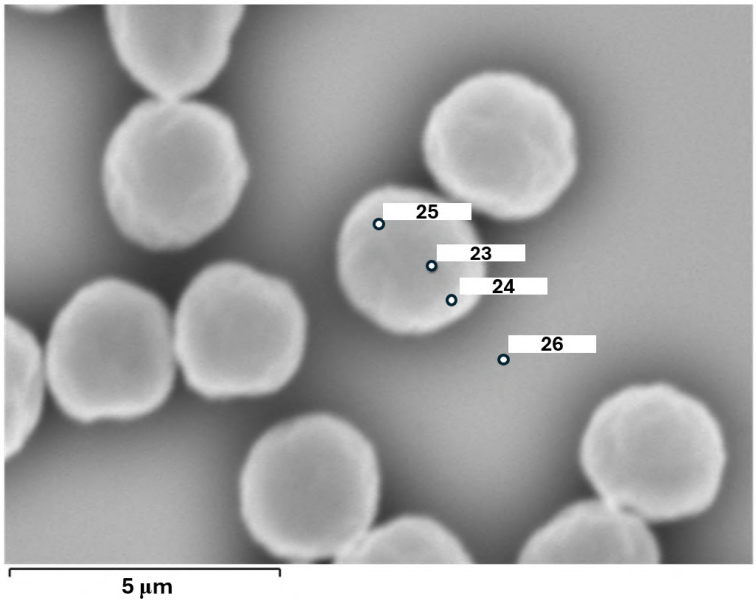

Figure B.2: The SEM image with positional EDS of the magnetic particles at 12000X.

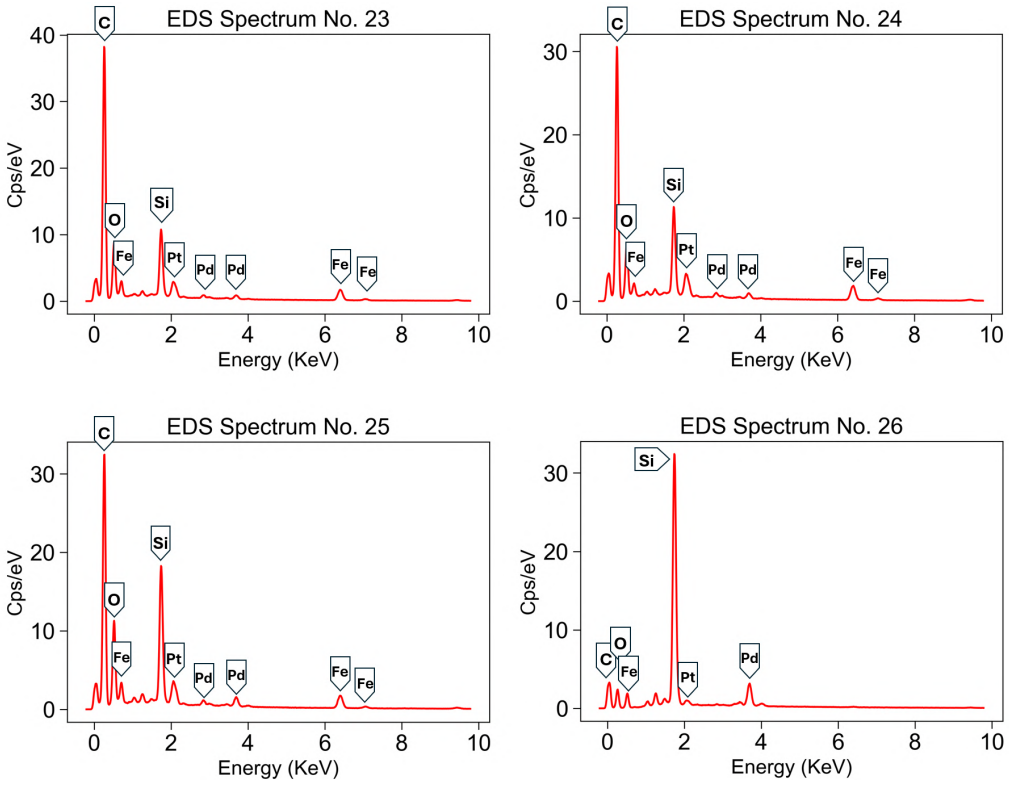

Figure B.3: EDS pattern of magnetic beads with different positions.

Elements	No. 23		No. 24		No. 25		No. 26	
	Weight %	Atomic %	Weight %	Atomic %	Weight %	Atomic %	Weight %	Atomic %
C	72.00	79.67	71.90	80.23	67.03	75.66	54.14	68.46
Al	0.07	0.03	0.08	0.04	0.11	0.06	0.67	0.38
Fe	2.97	0.71	3.80	0.91	2.86	0.69	0.42	0.11
Si	2.30	1.09	2.85	1.36	3.83	1.85	26.80	14.49
O	22.20	18.44	20.74	17.37	25.57	21.67	17.35	16.47
Pd	0.46	0.06	0.63	0.08	0.60	0.08	0.62	0.09

Table B.1: The weight and atomic percent of each spectrum corresponding to Fig. B.2

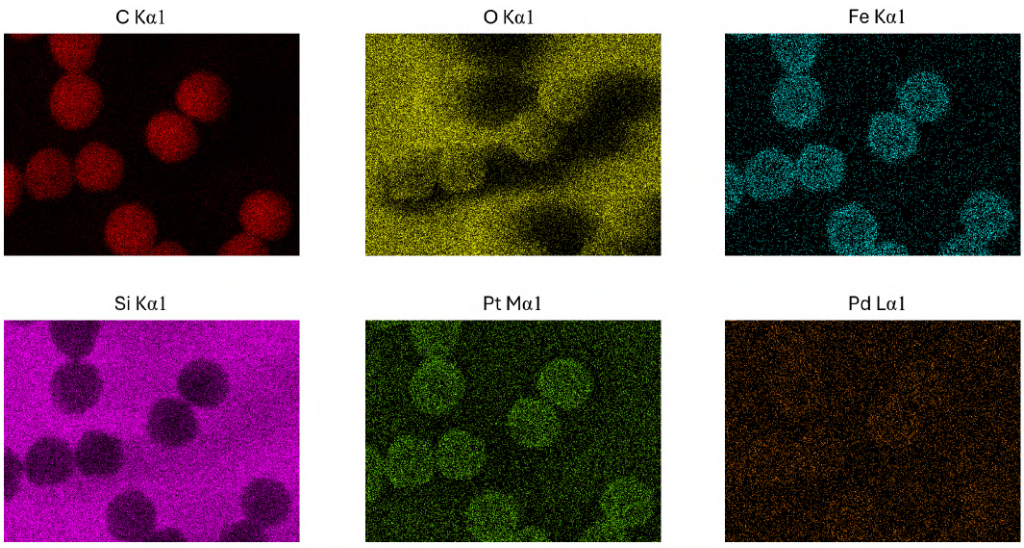

Figure B.4: The EDS elemental mapping images of magnetic beads for C, O, Fe, Si, Pt, and Pd.

The spatial distribution of the present elements is confirmed by the EDS element mapping images as shown in Fig. B.4. In this result, we obtained C and Fe distributions in each magnetic bead whereas the Si is absent for each particle. In Fig. B.5(a), the EDS line spectra are measured and demonstrate the increasing number of Carbon and Oxygen and the decreasing of Silicon inside the particle in Fig. B.5(b). For this evidence, we expected that there are two possible materials in the core particles. Firstly, the core is probably made of acrylic polymer such as poly methyl methacrylate (PMMA) with its chemical formula of $C_5H_8O_2$. Secondly, although the spectrum of Si decreased inside the core, its background does not become zero, suggesting that it is probably made of silicon dioxide (SiO_2). In Fig. B.5(c), we found that Fe is observed across the particle which is from the magnetite on the particle shell, and Pt from the sputtering.

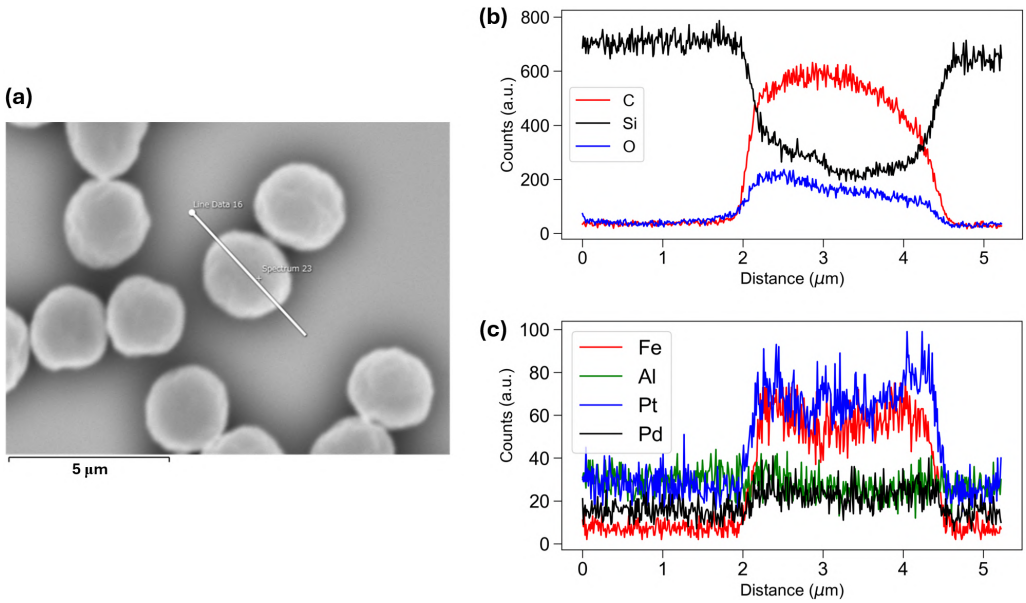

Figure B.5: (a) The EDS line spectrum across a magnetic bead. (b) The EDS line spectra of C, Si, and O. (c) The EDS line spectra of Fe, Al, Pt, and Pd.

Appendix C

The Local Strain in The Diamond Chip

We measured the ODMR spectrum with microwave power dependence at the diamond sample. The results showed that the ODRM contrasts are measured from the decrease in fluorescence related to the microwave power at 30 dBm, 25 dBm, 20 dBm, and 15 dBm with the narrow microwave ranges (2.84 to 2.90 GHz) as demonstrated in Fig. C.1(a)-(d), respectively. Each ODMR spectrum is fitted by the Lorentzian function, resulting in the increasing FWHM and two frequencies splitting from the local strain, E, in the diamond sample. This local strain probably occurred from the laser-cutting process which causes the lattice dislocation and distortion in the diamond samples.

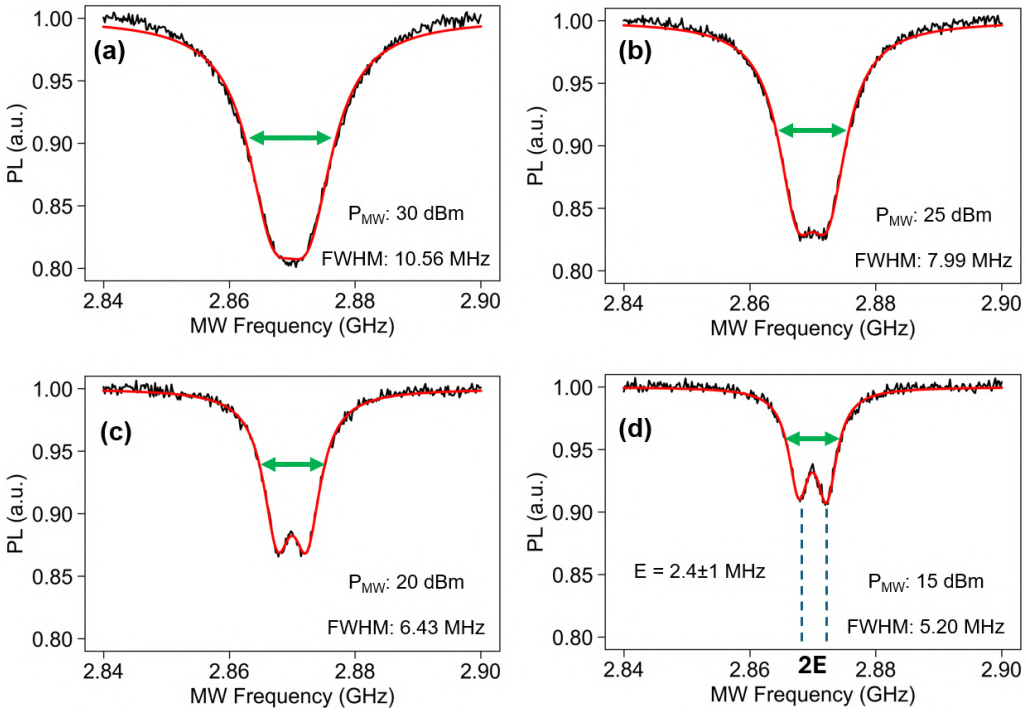

Figure C.1: ODMR spectra in the absence of a magnetic field with different microwave power dependents (a) at 30 dBm, (b) at 25 dBm, (c) at 20 dBm, and (d) at 15 dBm, respectively. The local strain was revealed at the minimum microwave power in (d).

Appendix D

Photoluminescence Quenching of The Superparamagnetic Core-shell Particles

The magnetic particles are diluted with the DI water with a ratio of 1:1 on the slide glass. The prepared sample is placed in a home-built confocal microscope as shown in Fig. D.1(a). The PL image from the scanning process is shown in Fig. D.1(b). The PL intensity generated from the particles is due to the polymer coated on their surfaces. The PL intensity of the particles is in the range of 60 kC/s, which is smaller than 10% of the PL intensity emitted from the diamond sample. The lifetime of PL intensity is measured when the laser excitation is started as shown in Fig. D.2(a) and (b) with two different selected particles in the PL images in Fig. D.2(c). The quenching of PL intensity implies the lifetime intensity in the range of several seconds after laser excitation at the magnetic particle. The PL intensity is decreased to nearly zero count per second after the experimental period of 10 seconds as shown in Fig. D.2(b) due to the PL quenching. The PL of the selected particle before and after the laser excitation is demonstrated in Fig. D.2(c) and (d), respectively.

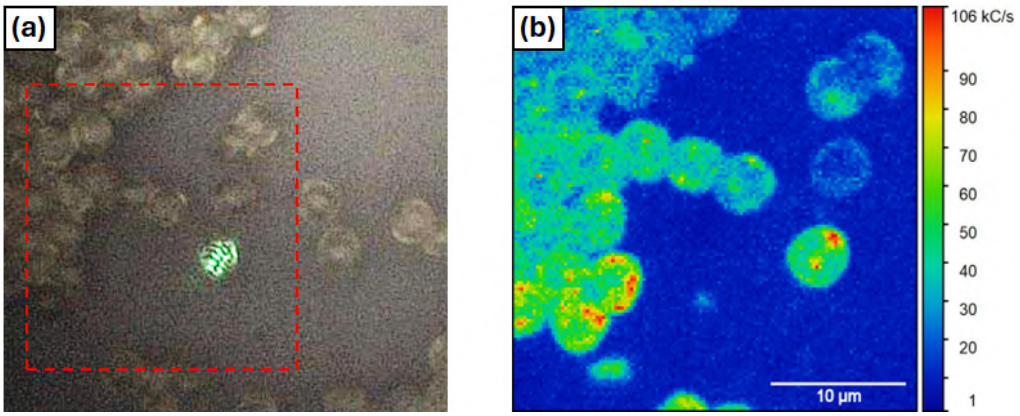

Figure D.1: (a) Optical image of the magnetic particles, and (b) the PL image emitted from the magnetic particles.

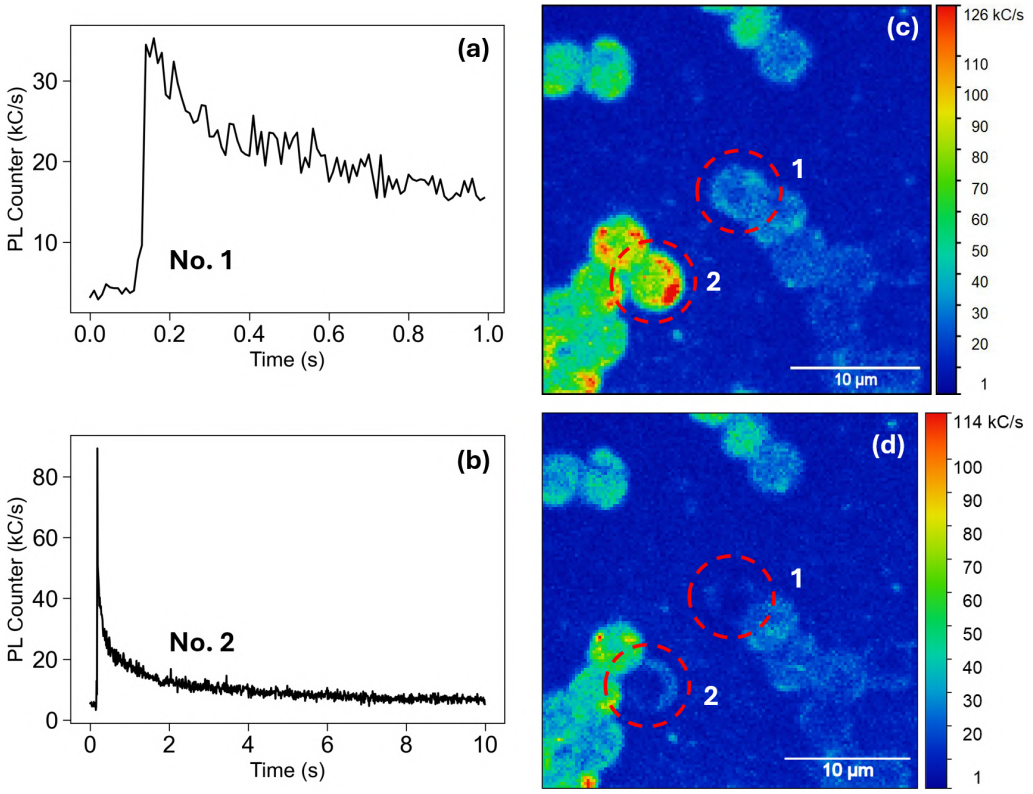

Figure D.2: (a) The PL quenching at the particle at position No. 1 with the maximum time scale of 1 second. (b) The PL quenching at the particle at position No. 1 with the maximum time scale of 10 seconds. (c)-(d) The PL intensity image of the magnetic particles before and after laser excitation, respectively.

Appendix E

Particle Size Estimation

From the experimental results, we measured $\Gamma_{int} = 1/\mathrm{T}_1, NV = 500$ Hz, and $\Gamma_{tot} = 1/\mathrm{T}_1, tot = 17{,}637$ Hz. Consequently, $\Gamma_{env} = \Gamma_{tot}$ - $\Gamma_{int} = 17{,}137$ Hz. For other free parameters, we assume the attempt period $\tau_0 = 1{\times}10^{-}13$ s for Fe_3O_4 nanoparticle which is covered the sensitivity window of the filter function of T_1 relaxometry as described in Sec.3.5. The effective anisotropy constant $K = 1.4{\times}10^4$ J/m^3 and $\theta = 54.7°$ for (100)-orientation diamond. The total distance of NV layer from the noise source, including a 5 nm thickness polymer from assumption $r = 45$ nm.

From Eq. 6.2, the resonance frequency of NV spin is $\omega_{NV} = 2\pi{\times}2.87{\times}10^9$ Hz. Due to τ_0 is very fast, we considered $\omega^2\tau_N^2 \ll 1$, then, it can be negligible. For this reason, Eq. 6.2 can be rewritten as

$$\Gamma_{tot} = \Gamma_{int} + 3\gamma^2 \left\langle B_\perp^2 \right\rangle \tau_N \tag{E.1}$$

When $\Gamma_{tot} - \Gamma_{int} = \Delta\Gamma$, we can express

$$\Delta\Gamma = 3\gamma^2 \frac{\rho_\mu^2 V^2 \mu_0^2}{48\pi^2} \left(\frac{5 - 3\cos^2\theta}{r^6} \right) \tau_0 \exp\left(\frac{KV}{k_B T} \right) \tag{E.2}$$

$$\frac{48\pi^2 \Delta\Gamma}{3\gamma^2 \rho_\mu^2 \mu_0^2 \tau_0} \left(\frac{r^6}{5 - 3\cos^2\theta} \right) = V^2 \exp\left(\frac{KV}{k_B T} \right) \tag{E.3}$$

For simplicity, we assumed that the term on the left side is β and the

term on the right side $\frac{K}{k_B T} = \alpha$. Then, we rearranged and obtained the exponential form as follows.

$$\beta = V^2 \exp(\alpha V) \tag{E.4}$$

Square root each side and rewrite

$$V e^{\alpha V/2} = \beta^{1/2} \tag{E.5}$$

$$\frac{\alpha V}{2} e^{\alpha V/2} = \frac{\alpha \beta^{1/2}}{2} \tag{E.6}$$

In this form, we used the Lambert-W function or product logarithm[121] to solve this equation. According to the Lambert-W function: $W(\phi e^{\phi}) = \phi$, when ϕ is a real number. Therefore, Eq. E.6 will be

$$W\left(\frac{\alpha V}{2} e^{\alpha V/2}\right) = W\left(\frac{\alpha \beta^{1/2}}{2}\right) \tag{E.7}$$

$$\frac{\alpha V}{2} = W\left(\frac{\alpha \beta^{1/2}}{2}\right) \tag{E.8}$$

$$V = \frac{2}{\alpha} W\left(\frac{\alpha \beta^{1/2}}{2}\right) \tag{E.9}$$

In Eq. E.9, we represented $\beta = 4.58 \times 10^{-48}$ and $\alpha = 3.38 \times 10^{24}$. However, there are two branches of the Lambert-W function for real number solving. Firstly, if $ye^y = x$, when y is the answer of $W_0(x), x \geq 0$. $W_0(x)$ is the Lambert-W function with branch 0. Secondly, if $-1/e \leq x < 0$, we will use W_{-1}, called the Lambert-W function with branch -1.

In our case, x is $\frac{\alpha \beta^{1/2}}{2}$ and ≥ 0. Therefore, we utilized the Lambert-W function with branch 0 to solve this problem. We extracted volume of the nanoparticle affects the relaxation time, $V = 6.8 \times 10^{-25}$ m^3 which corresponds to the spherical shape of the superparamagnetic nanoparticle with a diameter of 11 nm with $\tau_N \approx 9.9 \times 10^{-13}$ s.

Appendix F

NV-NV Interaction

F.1 NV Mesh Patterned Diamond

We prepared the NV mesh patterned diamond by using an electronic grade diamond, which was covered by a 6.5×6.5 μm^2 copper grid mask with 1×10^{12} ions/cm^2 dose at 30 keV of implantation energy per ion which corresponding to 33 nm depth of the NV density. The diamond sample was annealed at 900°C for 1 hour. After this process, the vacancy lattice was formed with nitrogen atoms, forming the ensemble NV defects in the diamond. This diamond sample was used as a target sample (See Fig. F.1).

F.2 Characteristic of Ensemble NV Diamond Probe

In Fig. F.2, A diamond with the same implantation process was cut by laser with a triangular shape. The polyvinyl alcohol (PVA) was used to coat its surface and sputtered by the Pt/Pd to protect the shallow NV from damage by the FIB milling process, which fabricated a 1 μm tip of the NV probe. The photoluminescence (PL) image is emitted from the NV tip after cleaning by Aqua Regia. The ESR spectrum of the NV tip shows the resonant frequency at 2.87 GHz (See Fig. F.3). A tungsten wire with 30 μm diameter was sharpened by chemical etching before attaching it to the tuning fork quartz crystal and the NV diamond probe, and then adjusting the position to make sure that the NV tip was pointed to the lowest position.

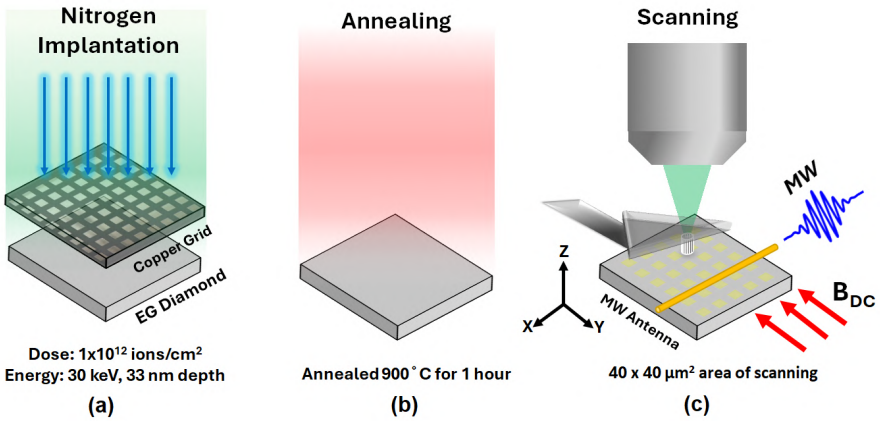

Figure F.1: Schematic of the NV mesh patterned diamond fabrication. (a) The electronic-grade diamond is covered by a copper grid mask and then implanted with nitrogen ions. (b) After the implantation process, the diamond sample was annealed to form the vacancy lattice. (c) Schematic illustrates the NV scanning probe on the NV mash target.

F.3 NV-NV Interaction Results

The NV mesh target was attached to the experimental system. The external magnetic field was generated by using the electromagnetic coils in between. The target sample was adjusted with 45° with the external magnetic vector which provided the most magnetic interaction to one of the NV axes. The NV probe approached the NV target during the fluorescence recording (See Fig. F.4(a)). The 40×40 μm^2 scanning area was started resulting in the fluorescence patterns as shown in Fig. F.4(b). The magnetic field dependence ESR image was recorded using the mixed fluorescence intensity between the scanning NV probe and the NV target. The frequency splitting under a magnetic field bias at 7.2 mT is classified as a spin state for each NV spin.

Because of the different axis between the NV probe and NV target, We can identify the Zeeman splitting that occurred between the NV probe and the NV target as shown in Fig. F.5. The NV probe was placed at the edge of the NV mesh patterned target to reduce the extreme fluorescence intensity from the patterned area as shown in Fig. F.5(Upper). By varying the external magnetic field, the Zeeman splitting frequencies were recorded as the function of the magnetic field as shown in Fig. F.5(Lower). From this result, we can identify the frequency of each spin of the NV probe and NV target. Consequently, the Rabi oscillation of each spin was measured with the same microwave power to have each π-pulse. To observe the electron spin

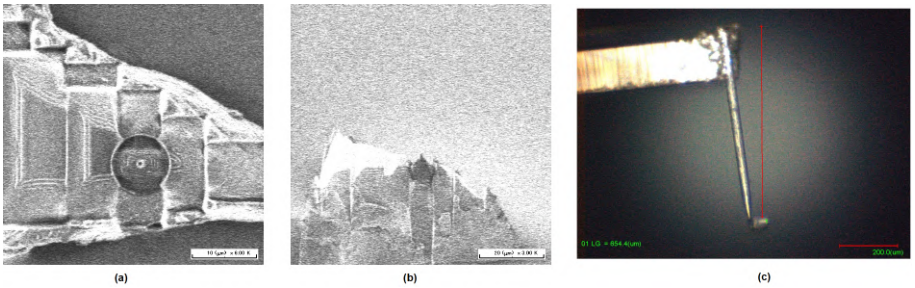

Figure F.2: (a) SEM image of the NV probe after FIB milling process (top view). The diameter of the NV tip is estimated at 1 μm and 4 μm long. (b) SEM image captured from the side view of the NV probe. (c) The tungsten wire with a diameter of 30 μm and around 500 μm long is attached to the tuning fork and the NV probe at the end.

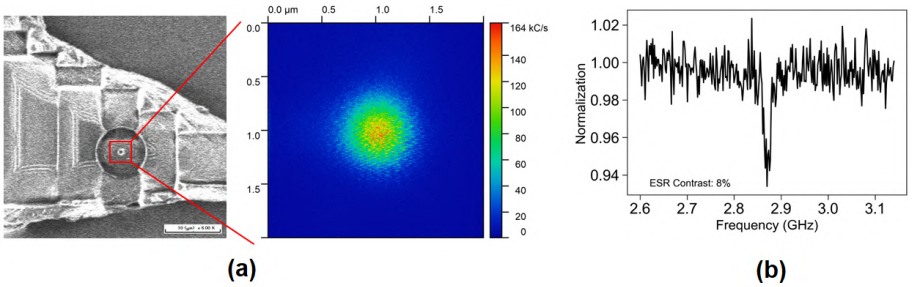

Figure F.3: (a) The fluorescence intensity measured from the NV tip which was estimated at 1 μm diameter. (b) The ESR spectrum was measured at the tip to confirm that the NV defects were located at the tip of the NV probe.

which may affect the electron spin at the NV probe, We measured the double electron-electron resonance (DEER) between the NV probe and target spins by using the microwave sequence as shown in Fig. F.6(a).

From the different transition frequencies between the NV probe and NV target, the Rabi oscillation is used to identify the MW π-pulse for each NV. DEER sequence is measured, and the dipole-dipole coupling effect causes the reverse dipole fields. The result is expected to be the disorder of the spin echo decay by showing the shortening of T_2, compared to the spin echo of the probe NV.

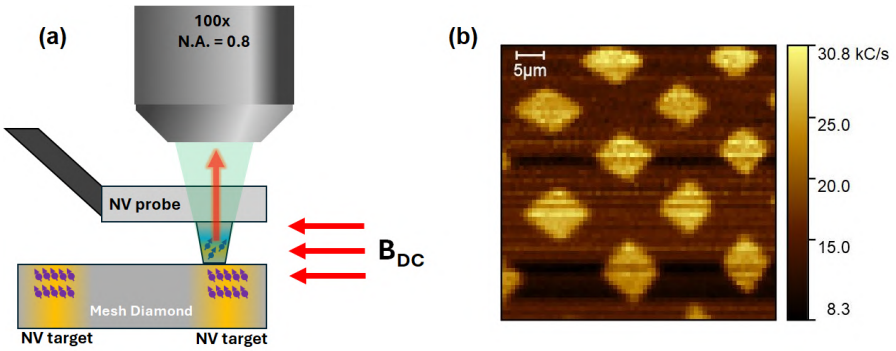

Figure F.4: Schematic of the NV-NV interaction experiment. (a) The NV probe is scanning on the NV mesh patterned diamond as the NV target under the magnetic field bias. (b) The experimental result was extracted from the fluorescence intensity through the NV probe. The bright areas were NV centers from nitrogen implantation through the copper grid mask.

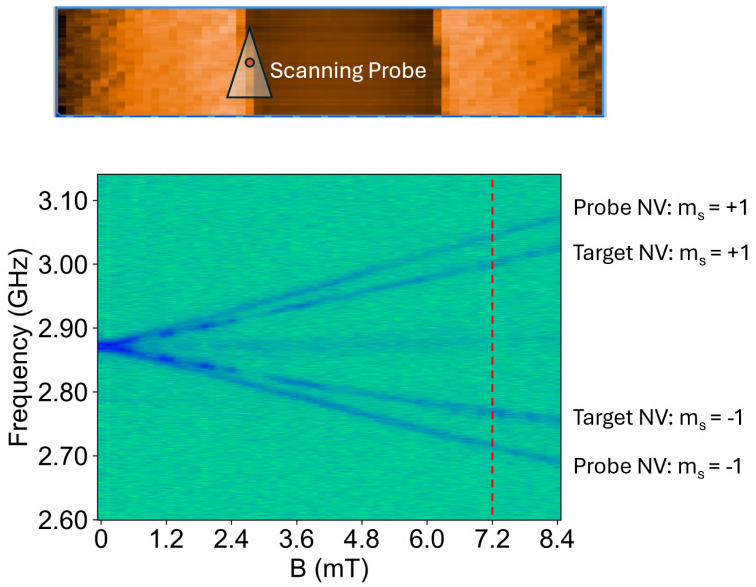

Figure F.5: (Upper) The scanning area by the recording of fluorescence intensity of 25×5 μm^2. The cartoon shows the NV probe position at the edge of the NV pattern. (Lower) The Zeeman splitting is measured as the function of varying external magnetic fields. The dashed line is marked at 7.2 mT which used to measure the NV−NV interaction between the NV probe and the NV target.

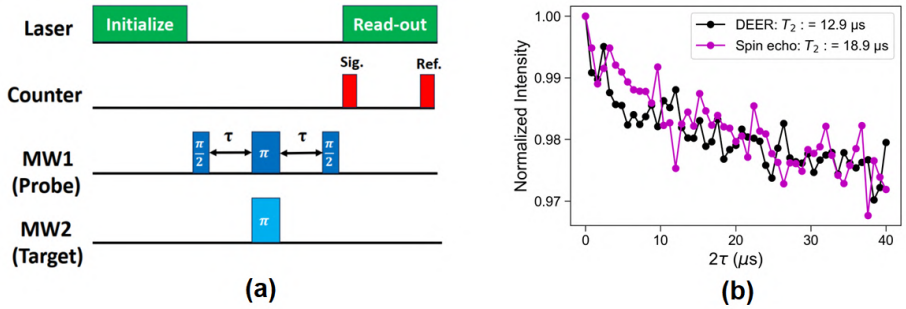

Figure F.6: (a) The electrons in the NV probe are excited by the Spin echo sequence from MW1. Meanwhile, the electrons on the target diamond are excited by a π-pulse from MW2. The result signal and reference are observed during read-out (b) The result from the DEER experiment was compared with the spin echo. The shorten coherent time was expected from the dipole-dipole coupling between the probe and target spins.

Appendix G

NV-P1 Center Interaction

G.1 Nitrogen defect: P1 Center

Generally, the nitrogen defects are located in a diamond. This defect is one of the most common defects in natural diamond and called P1 Center. The P1 center consists of a single substitutional nitrogen atom replacing a carbon atom in the diamond structure. This defect has an unpaired electron which is a paramagnetic behavior. The unpaired electron has a spin $S = 1/2$, performed a two level quantum system in a diamond structure. Moreover, this defect can interact with the external magnetic fields resulting in energy transition in atoms. However, P1 center cannot emit fluorescence which is not optically active as the NV center. To investigate the P1 center interaction, the double electron-electron resonance is utilized. P1 centers are often used as probes in experiments involving other defects like NV centers. They can serve as a source of magnetic noise or as a tool for calibrating and understanding the diamond's magnetic environment. Additionally, P1 centers are sometimes used to study the diamond's spin dynamics and coherence properties, which are crucial for the development of quantum devices.

G.2 Double Electron-Electron Resonance

Double Electron-Electron Resonance (DEER) with Nitrogen-Vacancy (NV) centers is a powerful technique used in quantum sensing and magnetic resonance. It combines the principles of electron spin resonance (ESR) and the unique properties of NV centers in diamond to measure the interactions

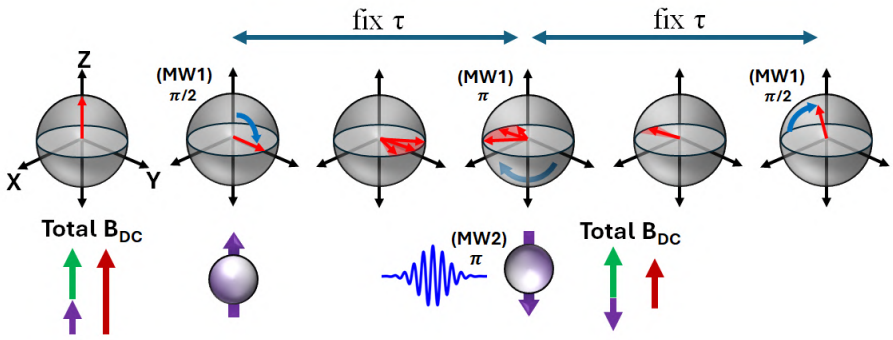

Figure G.1: Bloch sphere describes DEER experiment. When the second microwave frequency corresponding to the P1 Center is applied, the defect spins flip and the total magnetic field is changed, which cause the fluorescence drop in the NV spins.

between electron spins at the nanoscale. In DEER experiment, consists of a spin echo pulse sequence measuring at the NV probe as a sensor and the second MW π-pulse to excite the spin state of the sample. When the second π-pulse is applied, the target spin is flipped which causes the total magnetic field to reduce and changes the dipole interaction in the system (See Fig. G.1).

G.3 Experimental Results

We used the NV mesh patterned diamond to investigate the P1 center interaction. The external magnetic field was applied parallelly to one of the NV axis. The magnitude of the magnetic field is calculated by the ESR spectrum and spin echo with ^{13}C nuclear spin. In this case, the magnetic field is 32 mT which corresponding to Larmor frequency of ^{13}C nuclear spin at 344.75 kHz as shown in Fig. G.3(b). The resonance frequency of P1 center can be estimated by

$$f_{P1} = \gamma B_{ex} \tag{G.1}$$

Where γ is the gyromagnetic ratio of electron and B_{ex} is the external magnetic field. In this case, the P1 center frequency is approximately 901.32 MHz. Because of hyperfine coupling with the ^{14}N nuclear spin, other spin coupling with P1 center were observed (See Fig. G.4(b))

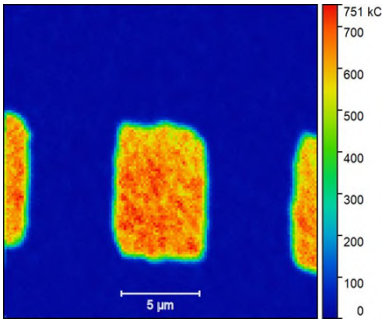

Figure G.2: The fluorescence image of the NV mesh patterned diamond. the bright area corresponds to the copper mask during nitrogen implantation.

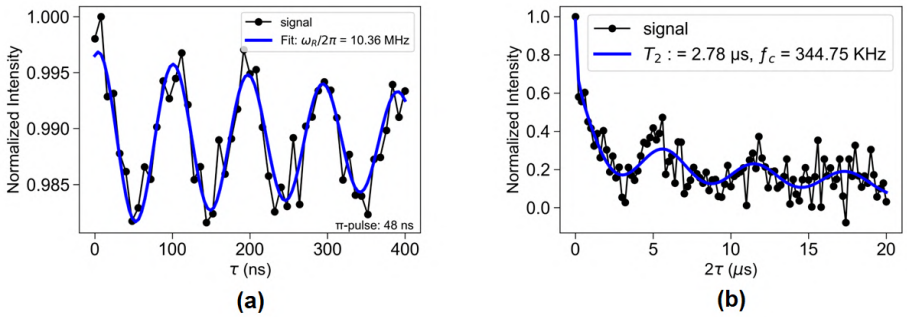

Figure G.3: (a) Rabi oscillation measured in the NV mesh area. The microwave power of 39 dBm was applied. The π-pulse of 48 ns is obtained and used to excite spin echo experiment. (b) Spin echo with ^{13}C nuclear spin oscillation.

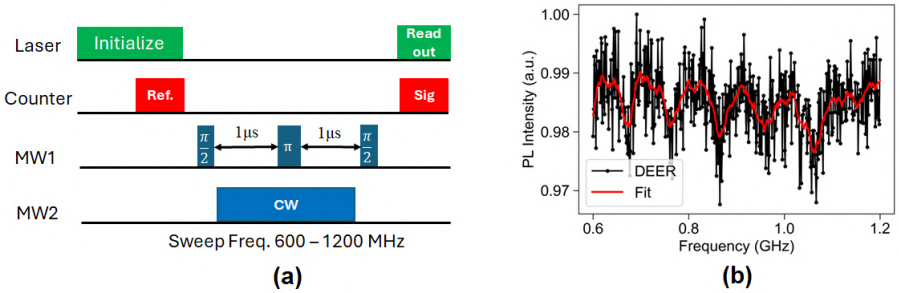

Figure G.4: (a) The microwave pulse sequence in DEER experiment. The microwave frequency is swept to match the P1 center resonance frequency. (b) The fluorescence intensity as a function of frequency which shows the P1 spin induces the magnetic noise to the NV spins, causing the fluorescence to decrease.

Appendix H

Widefield Nitrogen-Vacancy Magnetometry for The Magnetic B-H curve of The 2D Materials Estimation

In the nanomaterials world, a single atom bonded in one layer is developing and its applications are one of the promising materials for the modern future. This type of material is known as two-dimensional (2D) materials or Van Der Waals heterostructures. Generally, scientists regulated and derived single-layer materials from carrying the suffix "-ene" for a single-layer element, e.g. graphene, and "-ane" or "-ide" for single layer compound of two or more elements, e.g. tungsten disulfide. Advanced technology in materials science has been developing to overcome the drawbacks in microelectronics and pave the way for the quantum computing world in the future. Two-dimensional (2D) materials or single-layer materials are one of promising for solid-state applications and tend to be interesting in the frontier research in the present. Basically, nanomaterials are usually classified by the size or nanoscale in different dimensions. For example, a three-dimensional particle in the nanoscale is called a zero-dimensional (0D) material, commonly known as a nanoparticle in the quantum dot. When we consider a two-dimensional material in the nanoscale, but its shape is large and long size, consisting of various zero dimensions to form like a nanotube or nanowire, it will be determined as a dimensional (1D) material. Finally, a one-dimensional material with a single layer is also called a two-dimensional material or 2D material.

H.1 Widefield Nitrogen-Vacancy Spectroscopy

Magnetic imaging is one of the most technical methods that have been used to explore magnetic properties and structures, especially in living cells and nanomaterials for several decades. In biology, optical technique and quantum sensing have been combined to discover the bio-magnetic components behind, such as magnetotactic bacteria (MTB). Quantum magnetometry in spectroscope is also able to reveal the magnetic domains delivered in nanoparticles, for example, paramagnetism and ferromagnetism. Because these magnetic properties are weak and need high precision and high stability equipment for measuring, nitrogen-vacancy centers in bulk diamonds were considered to resolve the magnetic imaging techniques by providing a satisfactory signal-to-noise ratio (SNR). In 2008, dense NV-center diamonds were used to record the magnetic stray as a widefield magnetic image for the first time. This application is crucial in magnetic imaging as its capability to enhance the ultra-high sensitivity close to femtotesla/$\mathrm{Hz}^{1/2}$ with a micrometer range of spatial resolution. To achieve this work, we utilized optical equipment with ensemble NV diamond as magnetic array sensors. The optical microscope provided widefield image monitoring from the ensemble NV diamond at each microwave frequency. Thus, it is namely called a widefield NV microscope.

In the widefield NV setup, We used the ODMR experiment and recorded the fluorescence intensity by using the sCMOS sensor (See Fig. H.1(a)). The 2D material used in this experiment was a tungsten disulfide WS_2 flake. The 2D material was transferred to the 2 mm $\times$ 1 mm $\times$ 0.1 mm type-Ib (110) diamond. The magnetic field can be placed in between the diamond sample to induce the magnetic stray field in the 2D material. The stray field interacted with the one of NV axes which is parallel to the magnetic vector. The spin transition frequencies from the Zeeman splitting were identified at the bare diamond area before recording the stay field from the 2D material. The magnetic sample generates the stray magnetic field, B_{str} which induces the effective field along with the applied external magnetic field, B_{app}. Therefore, the total magnetic field, which is parallel to one of the NV axis to create the most Zeeman splitting, is $B_{NV} = B_{app} + B_{str}$ and related to the electron spin transition frequencies, f_+ and f_-, monitored by ODMR. This relation can be explained by.

$$B_{NV} = B_{app} + B_{str} = \frac{f_+ - f_-}{2\gamma}, \tag{H.1}$$

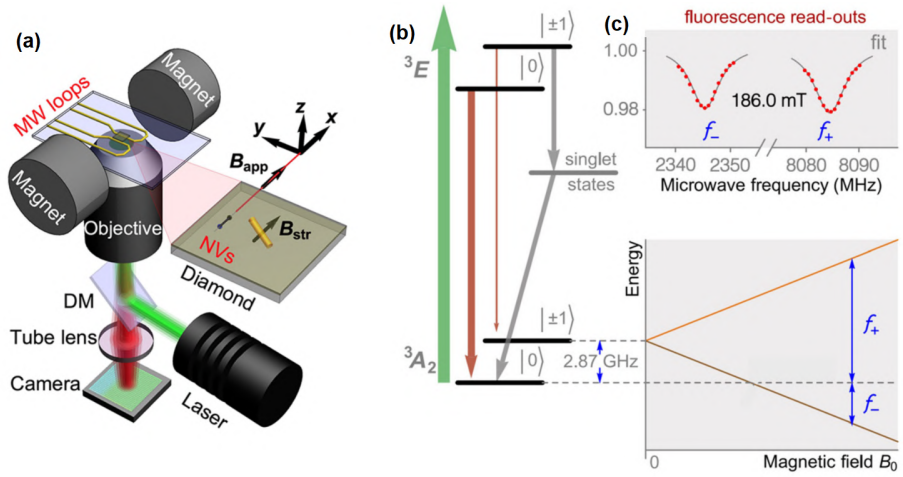

Figure H.1: (a) The ODMR experiment setup with widefield NV spectroscope. The external magnetic field from the magnets is parallel to one of the NV axes by the in-plane of the (110) diamond. (b) The NV energy levels when excited by a green laser. (c) The ODMR dips corresponding to the NV spin transition frequencies of f_- and f_+ due to 186 mT of B_{app}.

To extract the stray field image from the sample, the B_{app} is subtracted from Equation H.1 after ODMR recording from the sample. In case of the spin transition from the ground state anti-crossing, f_+ and f_- are summation. The fluorescent images from sweeping microwave frequency across f_+ and f_- are recorded by sCMOS for each frequency step. Therefore, The ODMR result indicated the minimum measurable B-field, fitting by the Lorentzian function. The magnetic images reveal the stay field images produced by the sample deposited on the NV diamond surface.

H.2 Widefield NV Image Processing

The microwave frequency is swept up to 16 MHz range which covers each ODMR transition frequency of the NV diamond. Consequently, the fluorescence images are acquired and accumulated the signal averaging for 32 arrays by the sCMOS sensor. In 32 microwave frequencies, they are separated into two frequencies of spin transitions, 16 frequencies for f_+ and another 16 frequencies for f_- (see Fig. H.2(a)). At a given pixel, there are 16 points ODMR curves of fluorescence intensity for each microwave frequency are marked and fit to a Lorentzian function by 16 points (see Fig. H.2(b)) which is related to the ODMR central frequency of its pixel. Each image is 600×600 pixels

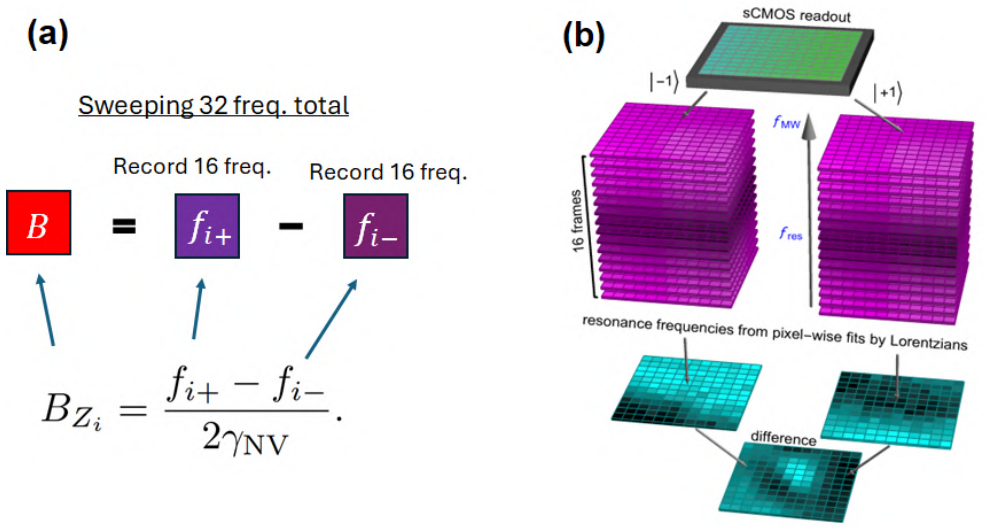

Figure H.2: (a) illustration the recording of each frequency from each side of the Zeeman splitting by 16 values. (b) The acquisition of fluorescence images for 32 frequencies covered the transition frequencies of the NV spin in the diamond sample.

corresponding to 65×65 nm^2 per pixel. Thus, each images of spin transition frequencies is stacked with the dimensions of 16×600×600. The ODMR magnetic images for each spin transition frequency are obtained from 16 images with 600×600 pixel size. These two images consist of the local magnetic field of $B_{app} + B_{str}$. Although there are other parameters, for instance, temperature, charge, and strain, that can shift the frequency, they could be eliminated by the subtraction process, $f_+ - f_- = (B_{app} + B_{str}) \cdot 2\gamma_{NV}$.

To measure the stray magnetic field, we only emphasized the magnetic field parallel to the NV diamond axis at the edge of the WS_2 flakes. In electromagnetism, the magnetic B-H curve (χ) of the materials implies how many materials become magnetized (M) when induced by an external magnetic field (H). The relation of magnetization in materials is[122]

$$M = \chi H, \tag{H.2}$$

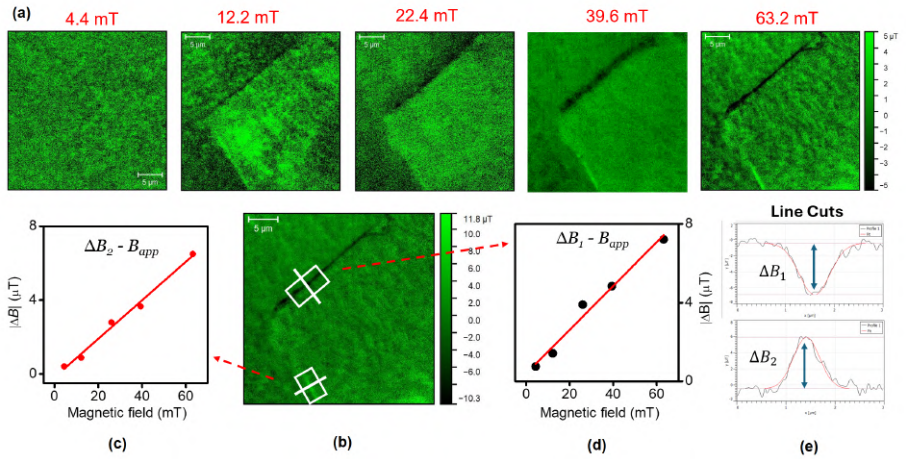

Figure H.3: (a) illustration the recording of each frequency from each side of the Zeeman splitting by 16 values. (b) The magnetic images and the white rectangular are the line cut measurement areas used to extract the ΔB of each B_{app}. (c), (d) The ΔB as a function B_{app}. The linear fitting of each area indicated the paramagnetic properties of WS_2 (e) The results of the average line cut were fit by the Gaussian fitting after measuring the ΔB for both areas.

H.3 Magnetic Stray Field and The Magnetic field B-H curve of WS_2

We applied the magnetic field from 0 to 70 mT by 5 values, B_{app} = 4.4, 12.2, 22.4, 39.6, and 63.2 mT as shown in Fig. H.3(a). The Fluorescence images of WS_2 flake were recorded into the sCMOS when the microwave was applied. In the Fig. H.3(b), the magnetic images and indicating line cut measurement areas are used to extract the stray magnetic field ΔB of each B_{app} which corresponds to M and H in the Eq. H.2, respectively. The amplitude of ΔB was calculated by subtracting B_{str} between the sample and diamond substrate via the Gwyddion software for AFM image analysis.

We managed to identify the magnetic B-H curve χ of WS_2 by a variation of the slope of the stray magnetic field $\Delta B - B_{app}$ dependence. These slopes help us estimate the magnetic B-H curve in each point or even multilayers in WS_2 flakes. The magnetic B-H curve of this sample is 7.34×10^{-5} and the linear fitting of $\Delta B - B_{app}$ plotting is confirmed that the WS_2 2D material displays the paramagnetic behavior.

Appendix I

Instrument List

In this experiment, we set up the instrument on a standard vibration isolation optical table. Some of the equipment and band companies are as follows,

1. **Laser Source**: Sintec Optronics PSU-HFDA, MLL-U-532B-50mW.
2. **ND filter**: FW2AND, Twelve Station Dual Filter Wheel for Ø1" (Ø25 mm) Filters with Base Assembly, 10 ND Filters Included
3. **Broadband Dielectric Mirror, 400 - 750 nm**: BB1-E02 - Ø1"
4. **LA1509-YAG - f = 100 mm**: Ø1", N-BK7 Plano-Convex Lens, 532/1064 nm V-Coat, Thorlabs
5. **AOM Laser beam modulator**: Panasonic model EFLM200AL2GW.
6. **LA1708-YAG - f = 200 mm**: Ø1", N-BK7 Plano-Convex Lens, 532/1064 nm V-Coat, Thorlabs
7. **Iris pinhole**: ID8/M
8. **Single mode fiber optic cable**: 488 - 633 nm, FC/APC, Ø900 μm Jacket, 2 m Long
9. **Dichroic beam-splitter**: FF552-Di02-25x36
10. **2D Galvo System, Silver-Coated Mirrors**: GVS002

11. **Mounting Adapter for a 2D Galvo System, Metric**: GCM102/M
12. **Gimbal Mirror Mount for the 30 mm Cage System**: KC45D1
13. **Objective lens**: Olympus LMPlanFL 100×/0.8 BD JAPAN
14. **Long pass filter**: LOPF-25C-635
15. **Fiber Launch System: Free Space, Metric**: KT110/M
16. **Single mode fiber optic cable**: 633 - 780 nm, FC/PC, Ø3 mm Jacket, 1 m Long
17. **APD for photon counting**: Excelitas Technologies SPCM-AQRH-14-FC
18. **Data acquisition (DAQ)**: National Instruments NI-DAQ USB-6211
19. **Pulse Blasters**: SpinCore PBESR-PRO-500-PCI (PCI board, 500 MHz)
20. **Low-Harmonic RF Generator**: SG6000F
21. **RF Switch 50Ω DC to 5000 MHz**: ZYSWA-2-50DR+
22. **High power amplifier 50Ω 15W 600 to 4200 MHz**: ZHL-15W-422-S+
23. **Power Supply for AOM TTL mode**: Yokogawa 7651 Programmable DC Source
24. **Power Supply for AOM Drive**: DC Stabilizing Power supply AD-8723D
25. **DC power supply for MW amplifier**: High reliability DC power supply PAN 35-20

Bibliography

[1] M. Zhu, Y. Hu, G. Li, W. Ou, P. Mao, S. Xin, and Y. Wan, "Combining magnetic nanoparticle with biotinylated nanobodies for rapid and sensitive detection of influenza h3n2," *Nanoscale Research Letters*, vol. 9, pp. 1–10, 2014.

[2] N. Nath, B. Godat, H. Benink, and M. Urh, "On-bead antibody-small molecule conjugation using high-capacity magnetic beads," *Journal of Immunological Methods*, vol. 426, pp. 95–103, 2015.

[3] S. Berensmeier, "Magnetic particles for the separation and purification of nucleic acids," *Applied microbiology and biotechnology*, vol. 73, pp. 495–504, 2006.

[4] M. Polikarpov, M. Ustinin, S. Rykunov, A. Yurenya, S. Naurzakov, A. Grebenkin, and V. Panchenko, "Study of anisotropy of magnetic noise, generated by magnetic particles in geomagnetic field," *Journal of Magnetism and Magnetic Materials*, vol. 475, pp. 620–626, 2019.

[5] S. Becker, N. Raatz, S. Jankuhn, R. John, and J. Meijer, "Nitrogen implantation with a scanning electron microscope," *Scientific reports*, vol. 8, no. 1, p. 32, 2018.

[6] C. L. Degen, F. Reinhard, and P. Cappellaro, "Quantum sensing," *Reviews of modern physics*, vol. 89, no. 3, p. 035002, 2017.

[7] L. M. Pham, N. Bar-Gill, D. Le Sage, C. Belthangady, A. Stacey, M. Markham, D. Twitchen, M. D. Lukin, and R. L. Walsworth, "Enhanced metrology using preferential orientation of nitrogen-vacancy centers in diamond," *Physical Review B—Condensed Matter and Materials Physics*, vol. 86, no. 12, p. 121202, 2012.

[8] F. Bundy, H. T. Hall, H. Strong, and R. Wentorfjun, "Man-made diamonds," *nature*, vol. 176, no. 4471, pp. 51–55, 1955.

[9] S. Eaton-Magaña, J. E. Shigley, and C. M. Breeding, "Observations on hpht-grown synthetic diamonds: a review," *Gems & Gemology*, vol. 53, no. 3, pp. 262–284, 2017.

[10] J.-C. Arnault, S. Saada, and V. Ralchenko, "Chemical vapor deposition single-crystal diamond: a review," *physica status solidi (RRL)–Rapid Research Letters*, vol. 16, no. 1, p. 2100354, 2022.

[11] Y. Zheng, C. Li, J. Liu, J. Wei, X. Zhang, H. Ye, and X. Ouyang, "Chemical vapor deposited diamond with versatile grades: from gemstone to quantum electronics," *Frontiers of Materials Science*, vol. 16, no. 1, p. 220590, 2022.

[12] T. Luo, L. Lindner, J. Langer, V. Cimalla, X. Vidal, F. Hahl, C. Schreyvogel, S. Onoda, S. Ishii, T. Ohshima, *et al.*, "Creation of nitrogen-vacancy centers in chemical vapor deposition diamond for sensing applications," *New Journal of Physics*, vol. 24, no. 3, p. 033030, 2022.

[13] V. M. Acosta, E. Bauch, M. P. Ledbetter, C. Santori, K.-M. Fu, P. E. Barclay, R. G. Beausoleil, H. Linget, J. F. Roch, F. Treussart, *et al.*, "Diamonds with a high density of nitrogen-vacancy centers for magnetometry applications," *Physical Review B—Condensed Matter and Materials Physics*, vol. 80, no. 11, p. 115202, 2009.

[14] A. Edmonds, U. D'Haenens-Johansson, R. Cruddace, M. E. Newton, K.-M. Fu, C. Santori, R. Beausoleil, D. Twitchen, and M. Markham, "Production of oriented nitrogen-vacancy color centers in synthetic diamond," *Physical Review B—Condensed Matter and Materials Physics*, vol. 86, no. 3, p. 035201, 2012.

[15] M. W. Doherty, N. B. Manson, P. Delaney, F. Jelezko, J. Wrachtrup, and L. C. Hollenberg, "The nitrogen-vacancy colour centre in diamond," *Physics Reports*, vol. 528, no. 1, pp. 1–45, 2013.

[16] A. Gruber, A. Drabenstedt, C. Tietz, L. Fleury, J. Wrachtrup, and C. v. Borczyskowski, "Scanning confocal optical microscopy and magnetic resonance on single defect centers," *Science*, vol. 276, no. 5321, pp. 2012–2014, 1997.

[17] A. Alkauskas, B. B. Buckley, D. D. Awschalom, and C. G. Van de Walle, "First-principles theory of the luminescence lineshape for the triplet transition in diamond nv centres," *New Journal of Physics*, vol. 16, no. 7, p. 073026, 2014.

[18] V. M. Acosta, *Optical Magnetometry with Nitrogen-Vacancy Centers in Diamond*. Phd thesis, University of California, Berkeley, 2011.

[19] L. Rondin, J.-P. Tetienne, T. Hingant, J.-F. Roch, P. Maletinsky, and V. Jacques, "Magnetometry with nitrogen-vacancy defects in diamond," *Reports on progress in physics*, vol. 77, no. 5, p. 056503, 2014.

[20] S. D. Subedi, V. V. Fedorov, J. Peppers, D. V. Martyshkin, S. B. Mirov, L. Shao, and M. Loncar, "Laser spectroscopic characterization of negatively charged nitrogen-vacancy (nv-) centers in diamond," *Optical Materials Express*, vol. 9, no. 5, pp. 2076–2087, 2019.

[21] J. Harrison, M. Sellars, and N. Manson, "Measurement of the optically induced spin polarisation of nv centres in diamond," *Diamond and related materials*, vol. 15, no. 4-8, pp. 586–588, 2006.

[22] P. Neumann, R. Kolesov, V. Jacques, J. Beck, J. Tisler, A. Batalov, L. Rogers, N. Manson, G. Balasubramanian, F. Jelezko, *et al.*, "Excited-state spectroscopy of single nv defects in diamond using optically detected magnetic resonance," *New Journal of Physics*, vol. 11, no. 1, p. 013017, 2009.

[23] L. Robledo, H. Bernien, T. Van Der Sar, and R. Hanson, "Spin dynamics in the optical cycle of single nitrogen-vacancy centres in diamond," *New Journal of Physics*, vol. 13, no. 2, p. 025013, 2011.

[24] G. Fuchs, V. Dobrovitski, D. Toyli, F. Heremans, C. Weis, T. Schenkel, and D. Awschalom, "Excited-state spin coherence of a single nitrogen–vacancy centre in diamond," *Nature Physics*, vol. 6, no. 9, pp. 668–672, 2010.

[25] Á. Gali, "Ab initio theory of the nitrogen-vacancy center in diamond," *Nanophotonics*, vol. 8, no. 11, pp. 1907–1943, 2019.

[26] D. B. Bucher, D. P. Aude Craik, M. P. Backlund, M. J. Turner, O. Ben Dor, D. R. Glenn, and R. L. Walsworth, "Quantum diamond spectrometer for nanoscale nmr and esr spectroscopy," *Nature Protocols*, vol. 14, no. 9, pp. 2707–2747, 2019.

[27] M. S. Grinolds, S. Hong, P. Maletinsky, L. Luan, M. D. Lukin, R. L. Walsworth, and A. Yacoby, "Nanoscale magnetic imaging of a single electron spin under ambient conditions," *Nature Physics*, vol. 9, no. 4, pp. 215–219, 2013.

[28] H. Mamin, M. Kim, M. Sherwood, C. T. Rettner, K. Ohno, D. Awschalom, and D. Rugar, "Nanoscale nuclear magnetic resonance

with a nitrogen-vacancy spin sensor," *Science*, vol. 339, no. 6119, pp. 557–560, 2013.

[29] T. Staudacher, F. Shi, S. Pezzagna, J. Meijer, J. Du, C. A. Meriles, F. Reinhard, and J. Wrachtrup, "Nuclear magnetic resonance spectroscopy on a (5-nanometer) 3 sample volume," *Science*, vol. 339, no. 6119, pp. 561–563, 2013.

[30] M. Cambria, G. Thiering, A. Norambuena, H. Dinani, A. Gardill, I. Kemeny, V. Lordi, A. Gali, J. Maze, and S. Kolkowitz, "Physically motivated analytical expression for the temperature dependence of the zero-field splitting of the nitrogen-vacancy center in diamond," *Physical Review B*, vol. 108, no. 18, p. L180102, 2023.

[31] V. M. Acosta, E. Bauch, M. P. Ledbetter, A. Waxman, L.-S. Bouchard, and D. Budker, "Temperature dependence of the nitrogen-vacancy magnetic resonance in diamond," *Physical review letters*, vol. 104, no. 7, p. 070801, 2010.

[32] G. Kusko *et al.*, "Nanometer scale quantum thermometry in a living cell," *arXiv preprint arXiv:1304.1068*, 2017.

[33] P. Neumann, I. Jakobi, F. Dolde, C. Burk, R. Reuter, G. Waldherr, J. Honert, T. Wolf, A. Brunner, J. H. Shim, *et al.*, "High-precision nanoscale temperature sensing using single defects in diamond," *Nano letters*, vol. 13, no. 6, pp. 2738–2742, 2013.

[34] V. Ivády, T. Simon, J. R. Maze, I. Abrikosov, and A. Gali, "Pressure and temperature dependence of the zero-field splitting in the ground state of nv centers in diamond: A first-principles study," *Physical Review B*, vol. 90, no. 23, p. 235205, 2014.

[35] E. Van Oort and M. Glasbeek, "Electric-field-induced modulation of spin echoes of nv centers in diamond," *Chemical Physics Letters*, vol. 168, no. 6, pp. 529–532, 1990.

[36] F. Dolde, H. Fedder, M. W. Doherty, T. Nöbauer, F. Rempp, G. Balasubramanian, T. Wolf, F. Reinhard, L. C. Hollenberg, F. Jelezko, *et al.*, "Electric-field sensing using single diamond spins," *Nature Physics*, vol. 7, no. 6, pp. 459–463, 2011.

[37] G. Q. Yan, S. Li, T. Yamamoto, M. Huang, N. J. Mclaughlin, T. Nozaki, H. Wang, S. Yuasa, and C. R. Du, "Electric-field-induced coherent control of nitrogen-vacancy centers," *Physical Review Applied*, vol. 18, no. 6, p. 064031, 2022.

[38] L. P. McGuinness, Y. Yan, A. Stacey, D. A. Simpson, L. T. Hall, D. Maclaurin, S. Prawer, P. Mulvaney, J. Wrachtrup, F. Caruso, *et al.*, "Quantum measurement and orientation tracking of fluorescent nanodiamonds inside living cells," *Nature nanotechnology*, vol. 6, no. 6, pp. 358–363, 2011.

[39] R. Giri, F. Gorrini, C. Dorigoni, C. Avalos, M. Cazzanelli, S. Tambalo, and A. Bifone, "Coupled charge and spin dynamics in high-density ensembles of nitrogen-vacancy centers in diamond," *Physical Review B*, vol. 98, no. 4, p. 045401, 2018.

[40] X.-D. Chen, C.-H. Dong, F.-W. Sun, C.-L. Zou, J.-M. Cui, Z.-F. Han, and G.-C. Guo, "Temperature dependent energy level shifts of nitrogen-vacancy centers in diamond," *Applied Physics Letters*, vol. 99, no. 16, 2011.

[41] M. W. Doherty, V. V. Struzhkin, D. A. Simpson, L. P. McGuinness, Y. Meng, A. Stacey, T. J. Karle, R. J. Hemley, N. B. Manson, L. C. Hollenberg, *et al.*, "Electronic properties and metrology applications of the diamond nv- center under pressure," *Physical review letters*, vol. 112, no. 4, p. 047601, 2014.

[42] J. R. B. John A. Weil, *Electron Paramagnetic Resonance*. Wiley, 2006.

[43] J. F. Barry, J. M. Schloss, E. Bauch, M. J. Turner, C. A. Hart, L. M. Pham, and R. L. Walsworth, "Sensitivity optimization for nv-diamond magnetometry," *Reviews of Modern Physics*, vol. 92, no. 1, p. 015004, 2020.

[44] K. Jeong, A. J. Parker, R. H. Page, A. Pines, C. C. Vassiliou, and J. P. King, "Understanding the magnetic resonance spectrum of nitrogen vacancy centers in an ensemble of randomly oriented nanodiamonds," *The Journal of Physical Chemistry C*, vol. 121, no. 38, pp. 21057–21061, 2017.

[45] N. D. Lai, D. Zheng, F. Jelezko, F. Treussart, and J.-F. Roch, "Influence of a static magnetic field on the photoluminescence of an ensemble of nitrogen-vacancy color centers in a diamond single-crystal," *Applied Physics Letters*, vol. 95, no. 13, 2009.

[46] J. P. Tetienne, L. Rondin, P. Spinicelli, M. Chipaux, T. Debuisschert, J.-F. Roch, and V. Jacques, "Magnetic-field-dependent photodynamics of single nv defects in diamond: an application to qualitative all-optical magnetic imaging," *New Journal of Physics*, vol. 14, no. 10, p. 103033, 2012.

[47] C.-R. Wie, "Two-qubit bloch sphere," *Physics*, vol. 2, no. 3, pp. 383–396, 2020.

[48] M. Frimmer and L. Novotny, "The classical bloch equations," *American Journal of Physics*, vol. 82, no. 10, pp. 947–954, 2014.

[49] J. M. Martinis, S. Nam, J. Aumentado, K. Lang, and C. Urbina, "Decoherence of a superconducting qubit due to bias noise," *Physical Review B*, vol. 67, no. 9, p. 094510, 2003.

[50] D. Kikuchi, D. Prananto, K. Hayashi, A. Laraoui, N. Mizuochi, M. Hatano, E. Saitoh, Y. Kim, C. A. Meriles, and T. An, "Long-distance excitation of nitrogen-vacancy centers in diamond via surface spin waves," *Applied Physics Express*, vol. 10, no. 10, p. 103004, 2017.

[51] A. Dréau, M. Lesik, L. Rondin, P. Spinicelli, O. Arcizet, J.-F. Roch, and V. Jacques, "Avoiding power broadening in optically detected magnetic resonance of single nv defects for enhanced dc magnetic field sensitivity," *Physical Review B—Condensed Matter and Materials Physics*, vol. 84, no. 19, p. 195204, 2011.

[52] Y. Nakamura, H. Watanabe, H. Sumiya, K. M. Itoh, K. Sasaki, J. Ishi-Hayase, and K. Kobayashi, "Optimization of optical spin readout of the nitrogen-vacancy center in diamond based on spin relaxation model," *AIP Advances*, vol. 12, no. 5, 2022.

[53] J. Chen, O. Y. Chen, and H.-C. Chang, "Relaxation of a dense ensemble of spins in diamond under a continuous microwave driving field," *Scientific reports*, vol. 11, no. 1, p. 16278, 2021.

[54] K. Mizuno, M. Nakajima, H. Ishiwata, M. Hatano, and T. Iwasaki, "Electron spin contrast of high-density and perfectly aligned nitrogen-vacancy centers synthesized by chemical vapor deposition," *Applied Physics Express*, vol. 14, no. 3, p. 032001, 2021.

[55] V. K. Sewani, H. H. Vallabhapurapu, Y. Yang, H. R. Firgau, C. Adambukulam, B. C. Johnson, J. J. Pla, and A. Laucht, "Coherent control of nv- centers in diamond in a quantum teaching lab," *American Journal of Physics*, vol. 88, no. 12, pp. 1156–1169, 2020.

[56] C.-H. Li, D.-F. Li, Y. Zheng, F.-W. Sun, A. Du, and Y.-S. Ge, "Detecting axial ratio of microwave field with high resolution using nv centers in diamond," *Sensors*, vol. 19, no. 10, p. 2347, 2019.

[57] L. Robledo, H. Bernien, I. Van Weperen, and R. Hanson, "Control and

coherence of the optical transition of single nitrogen vacancy centers in diamond," *Physical review letters*, vol. 105, no. 17, p. 177403, 2010.

[58] J. M. Taylor, P. Cappellaro, L. Childress, L. Jiang, D. Budker, P. Hemmer, A. Yacoby, R. Walsworth, and M. Lukin, "High-sensitivity diamond magnetometer with nanoscale resolution," *Nature Physics*, vol. 4, no. 10, pp. 810–816, 2008.

[59] G. Balasubramanian, P. Neumann, D. Twitchen, M. Markham, R. Kolesov, N. Mizuochi, J. Isoya, J. Achard, J. Beck, J. Tissler, *et al.*, "Ultralong spin coherence time in isotopically engineered diamond," *Nature materials*, vol. 8, no. 5, pp. 383–387, 2009.

[60] A. Jarmola, V. Acosta, K. Jensen, S. Chemerisov, and D. Budker, "Temperature-and magnetic-field-dependent longitudinal spin relaxation in nitrogen-vacancy ensembles in diamond," *Physical review letters*, vol. 108, no. 19, p. 197601, 2012.

[61] G. Fuchs, V. Dobrovitski, R. Hanson, A. Batra, C. Weis, T. Schenkel, and D. Awschalom, "Excited-state spectroscopy using single spin manipulation in diamond," *Physical review letters*, vol. 101, no. 11, p. 117601, 2008.

[62] N. D. Lai, D. Zheng, F. Jelezko, F. Treussart, and J.-F. Roch, "Influence of a static magnetic field on the photoluminescence of an ensemble of nitrogen-vacancy color centers in a diamond single-crystal," *Applied Physics Letters*, vol. 95, no. 13, 2009.

[63] R. Epstein, F. Mendoza, Y. Kato, and D. Awschalom, "Anisotropic interactions of a single spin and dark-spin spectroscopy in diamond," *Nature physics*, vol. 1, no. 2, pp. 94–98, 2005.

[64] J. F. Barry, M. J. Turner, J. M. Schloss, D. R. Glenn, Y. Song, M. D. Lukin, H. Park, and R. L. Walsworth, "Optical magnetic detection of single-neuron action potentials using quantum defects in diamond," *Proceedings of the National Academy of Sciences*, vol. 113, no. 49, pp. 14133–14138, 2016.

[65] S. Lamichhane, K. A. McElveen, A. Erickson, I. Fescenko, S. Sun, R. Timalsina, Y. Guo, S.-H. Liou, R. Y. Lai, and A. Laraoui, "Nitrogen-vacancy magnetometry of individual fe-triazole spin crossover nanorods," *ACS nano*, vol. 17, no. 9, pp. 8694–8704, 2023.

[66] J. T. Oon, J. Tang, C. A. Hart, K. S. Olsson, M. J. Turner, J. M.

Schloss, and R. L. Walsworth, "Ramsey envelope modulation in nv diamond magnetometry," *Physical Review B*, vol. 106, no. 5, p. 054110, 2022.

[67] E. O. Schafer-Nolte, *Development of a diamond-vased scanning probe spin sensor operating at low temperature in ultra high vacuum*. Phd thesis, Physikalisches Institut der Universit¨at Stuttgart, Stuttgart, 2014.

[68] R. Schirhagl, K. Chang, M. Loretz, and C. L. Degen, "Nitrogen-vacancy centers in diamond: nanoscale sensors for physics and biology," *Annual review of physical chemistry*, vol. 65, no. 1, pp. 83–105, 2014.

[69] J. F. Barry, M. H. Steinecker, S. T. Alsid, J. Majumder, L. M. Pham, M. F. O'Keefe, and D. A. Braje, "Sensitive ac and dc magnetometry with nitrogen-vacancy center ensembles in diamond," *arXiv preprint arXiv:2305.06269*, 2023.

[70] E. L. Hahn, "Spin echoes," *Physical review*, vol. 80, no. 4, p. 580, 1950.

[71] A. Dréau, J.-R. Maze, M. Lesik, J.-F. Roch, and V. Jacques, "High-resolution spectroscopy of single nv defects coupled with nearby 13 c nuclear spins in diamond," *Physical Review B—Condensed Matter and Materials Physics*, vol. 85, no. 13, p. 134107, 2012.

[72] L. Childress, M. Gurudev Dutt, J. Taylor, A. Zibrov, F. Jelezko, J. Wrachtrup, P. Hemmer, and M. Lukin, "Coherent dynamics of coupled electron and nuclear spin qubits in diamond," *Science*, vol. 314, no. 5797, pp. 281–285, 2006.

[73] B. J. Shields, Q. P. Unterreithmeier, N. P. de Leon, H. Park, and M. D. Lukin, "Efficient readout of a single spin state in diamond via spin-to-charge conversion," *Physical review letters*, vol. 114, no. 13, p. 136402, 2015.

[74] L. Luan, M. S. Grinolds, S. Hong, P. Maletinsky, R. L. Walsworth, and A. Yacoby, "Decoherence imaging of spin ensembles using a scanning single-electron spin in diamond," *Scientific reports*, vol. 5, no. 1, p. 8119, 2015.

[75] S. Hernández-Gómez and N. Fabbri, "Quantum control for nanoscale spectroscopy with diamond nitrogen-vacancy centers: a short review," *Frontiers in Physics*, vol. 8, p. 610868, 2021.

[76] E. Schäfer-Nolte, L. Schlipf, M. Ternes, F. Reinhard, K. Kern, and J. Wrachtrup, "Tracking temperature-dependent relaxation times of ferritin nanomagnets with a wideband quantum spectrometer," *Physical review letters*, vol. 113, no. 21, p. 217204, 2014.

[77] Ł. Cywiński, R. M. Lutchyn, C. P. Nave, and S. Das Sarma, "How to enhance dephasing time in superconducting qubits," *Physical Review B—Condensed Matter and Materials Physics*, vol. 77, no. 17, p. 174509, 2008.

[78] S. Hernández-Gómez, F. Poggiali, P. Cappellaro, and N. Fabbri, "Noise spectroscopy of a quantum-classical environment with a diamond qubit," *Physical Review B*, vol. 98, no. 21, p. 214307, 2018.

[79] J. Zhou, H. D. Shin, K. Chen, B. Song, R. A. Duncan, Q. Xu, A. A. Maznev, K. A. Nelson, and G. Chen, "Direct observation of large electron–phonon interaction effect on phonon heat transport," *Nature communications*, vol. 11, no. 1, p. 6040, 2020.

[80] T. de Guillebon, B. Vindolet, J.-F. Roch, V. Jacques, and L. Rondin, "Temperature dependence of the longitudinal spin relaxation time t 1 of single nitrogen-vacancy centers in nanodiamonds," *Physical Review B*, vol. 102, no. 16, p. 165427, 2020.

[81] J.-P. Tetienne, T. Hingant, L. Rondin, A. Cavaillès, L. Mayer, G. Dantelle, T. Gacoin, J. Wrachtrup, J.-F. Roch, and V. Jacques, "Spin relaxometry of single nitrogen-vacancy defects in diamond nanocrystals for magnetic noise sensing," *Physical Review B—Condensed Matter and Materials Physics*, vol. 87, no. 23, p. 235436, 2013.

[82] F. Gorrini, R. Giri, C. Avalos, S. Tambalo, S. Mannucci, L. Basso, N. Bazzanella, C. Dorigoni, M. Cazzanelli, P. Marzola, *et al.*, "Fast and sensitive detection of paramagnetic species using coupled charge and spin dynamics in strongly fluorescent nanodiamonds," *ACS applied materials & interfaces*, vol. 11, no. 27, pp. 24412–24422, 2019.

[83] N. Sadzak, M. Héritier, and O. Benson, "Coupling a single nitrogen-vacancy center in nanodiamond to superparamagnetic nanoparticles," *Scientific reports*, vol. 8, no. 1, p. 8430, 2018.

[84] S. E. Lillie, D. A. Broadway, N. Dontschuk, A. Zavabeti, D. A. Simpson, T. Teraji, T. Daeneke, L. C. Hollenberg, and J.-P. Tetienne, "Magnetic noise from ultrathin abrasively deposited materials on diamond," *Physical Review Materials*, vol. 2, no. 11, p. 116002, 2018.

[85] M. Pelliccione, B. A. Myers, L. Pascal, A. Das, and A. Bleszynski Jayich, "Two-dimensional nanoscale imaging of gadolinium spins via scanning probe relaxometry with a single spin in diamond," *Physical Review Applied*, vol. 2, no. 5, p. 054014, 2014.

[86] A. Batalov, C. Zierl, T. Gaebel, P. Neumann, I.-Y. Chan, G. Balasubramanian, P. Hemmer, F. Jelezko, and J. Wrachtrup, "Temporal coherence of photons emitted by single nitrogen-vacancy defect centers in diamond using optical rabi-oscillations," *Physical review letters*, vol. 100, no. 7, p. 077401, 2008.

[87] S. Steinert, F. Ziem, L. Hall, A. Zappe, M. Schweikert, N. Götz, A. Aird, G. Balasubramanian, L. Hollenberg, and J. Wrachtrup, "Magnetic spin imaging under ambient conditions with sub-cellular resolution," *Nature communications*, vol. 4, no. 1, p. 1607, 2013.

[88] T. Rosskopf, A. Dussaux, K. Ohashi, M. Loretz, R. Schirhagl, H. Watanabe, S. Shikata, K. M. Itoh, and C. Degen, "Investigation of surface magnetic noise by shallow spins in diamond," *Physical review letters*, vol. 112, no. 14, p. 147602, 2014.

[89] A. Akbarzadeh, M. Samiei, and S. Davaran, "Magnetic nanoparticles: preparation, physical properties, and applications in biomedicine," *Nanoscale research letters*, vol. 7, pp. 1–13, 2012.

[90] Y. Javed, K. Akhtar, H. Anwar, and Y. Jamil, "Mri based on iron oxide nanoparticles contrast agents: effect of oxidation state and architecture," *Journal of Nanoparticle Research*, vol. 19, pp. 1–25, 2017.

[91] A. Rajan and N. K. Sahu, "Review on magnetic nanoparticle-mediated hyperthermia for cancer therapy," *Journal of Nanoparticle Research*, vol. 22, pp. 1–25, 2020.

[92] H. Soo Choi, W. Liu, P. Misra, E. Tanaka, J. P. Zimmer, B. Itty Ipe, M. G. Bawendi, and J. V. Frangioni, "Renal clearance of quantum dots," *Nature biotechnology*, vol. 25, no. 10, pp. 1165–1170, 2007.

[93] C. Murray, D. J. Norris, and M. G. Bawendi, "Synthesis and characterization of nearly monodisperse cde (e= sulfur, selenium, tellurium) semiconductor nanocrystallites," *Journal of the American Chemical Society*, vol. 115, no. 19, pp. 8706–8715, 1993.

[94] Y. Gossuin, P. Gillis, A. Hocq, Q. L. Vuong, and A. Roch, "Magnetic resonance relaxation properties of superparamagnetic particles," *Wi-*

ley Interdisciplinary Reviews: Nanomedicine and Nanobiotechnology, vol. 1, no. 3, pp. 299–310, 2009.

[95] S. Lamichhane, R. Timalsina, C. Schultz, I. Fescenko, K. Ambal, S.-H. Liou, R. Y. Lai, and A. Laraoui, "Nitrogen-vacancy magnetic relaxometry of nanoclustered cytochrome c proteins," *Nano Letters*, vol. 24, no. 3, pp. 873–880, 2024.

[96] J. Frenkel and J. Doefman, "Spontaneous and induced magnetisation in ferromagnetic bodies," *Nature*, vol. 126, no. 3173, pp. 274–275, 1930.

[97] C. Kittel, "Theory of the structure of ferromagnetic domains in films and small particles," *Physical Review*, vol. 70, no. 11-12, p. 965, 1946.

[98] C. T. Yavuz, J. Mayo, W. W. Yu, A. Prakash, J. C. Falkner, S. Yean, L. Cong, H. J. Shipley, A. Kan, M. Tomson, *et al.*, "Low-field magnetic separation of monodisperse fe3o4 nanocrystals," *science*, vol. 314, no. 5801, pp. 964–967, 2006.

[99] A. Venäläinen, *Modification of bare and functionalized Au(111) surfaces and ferromagnetism of Au and Pd nanoclusters*. Phd thesis, University of Helsinki, HELSINGFORS, 2018.

[100] L. Néel, "Théorie du traînage magnétique des ferromagnétiques en grains fins avec application aux terres cuites," in *Annales de géophysique*, vol. 5, pp. 99–136, 1949.

[101] G. F. Goya, T. Berquo, F. C. Fonseca, and M. Morales, "Static and dynamic magnetic properties of spherical magnetite nanoparticles," *Journal of applied physics*, vol. 94, no. 5, pp. 3520–3528, 2003.

[102] R. Moreno, S. Jenkins, W. Williams, and R. F. Evans, "Atomistic calculation of the f0 attempt frequency in fe3o4 magnetite nanoparticles," *arXiv preprint arXiv:2401.12080*, 2024.

[103] I. Cardoso Barbosa, J. Gutsche, and A. Widera, "Impact of charge conversion on nv-center relaxometry," *Physical Review B*, vol. 108, no. 7, p. 075411, 2023.

[104] J.-P. Tetienne, A. Lombard, D. A. Simpson, C. Ritchie, J. Lu, P. Mulvaney, and L. C. Hollenberg, "Scanning nanospin ensemble microscope for nanoscale magnetic and thermal imaging," *Nano Letters*, vol. 16, no. 1, pp. 326–333, 2016.

[105] S. Kolkowitz, A. Safira, A. High, R. Devlin, S. Choi, Q. Unterreithmeier, D. Patterson, A. Zibrov, V. Manucharyan, H. Park, *et al.*,

"Probing johnson noise and ballistic transport in normal metals with a single-spin qubit," *Science*, vol. 347, no. 6226, pp. 1129–1132, 2015.

[106] A. Ariyaratne, D. Bluvstein, B. A. Myers, and A. C. B. Jayich, "Nanoscale electrical conductivity imaging using a nitrogen-vacancy center in diamond," *Nature communications*, vol. 9, no. 1, p. 2406, 2018.

[107] D. Schmid-Lorch, T. Haberle, F. Reinhard, A. Zappe, M. Slota, L. Bogani, A. Finkler, and J. Wrachtrup, "Relaxometry and dephasing imaging of superparamagnetic magnetite nanoparticles using a single qubit," *Nano letters*, vol. 15, no. 8, pp. 4942–4947, 2015.

[108] M. Mrózek, D. Rudnicki, P. Kehayias, A. Jarmola, D. Budker, and W. Gawlik, "Longitudinal spin relaxation in nitrogen-vacancy ensembles in diamond," *EPJ Quantum Technology*, vol. 2, pp. 1–11, 2015.

[109] S. Lamichhane, R. Timalsina, C. Schultz, I. Fescenko, K. Ambal, S.-H. Liou, R. Y. Lai, and A. Laraoui, "Nitrogen-vacancy magnetic relaxometry of nanoclustered cytochrome c proteins," *Nano Letters*, vol. 24, no. 3, pp. 873–880, 2024.

[110] A. Haque and S. Sumaiya, "An overview on the formation and processing of nitrogen-vacancy photonic centers in diamond by ion implantation," *Journal of Manufacturing and Materials Processing*, vol. 1, no. 1, p. 6, 2017.

[111] P. Kehayias, J. Henshaw, M. S. Ziabari, M. Titze, E. Bielejec, M. P. Lilly, and A. M. Mounce, "A fitting algorithm for optimizing ion implantation energies and fluences," *Nuclear Instruments and Methods in Physics Research Section B: Beam Interactions with Materials and Atoms*, vol. 500, pp. 52–56, 2021.

[112] J. F. Ziegler, M. D. Ziegler, and J. P. Biersack, "Srim–the stopping and range of ions in matter (2010)," *Nuclear Instruments and Methods in Physics Research Section B: Beam Interactions with Materials and Atoms*, vol. 268, no. 11-12, pp. 1818–1823, 2010.

[113] B. Naydenov, F. Reinhard, A. Lämmle, V. Richter, R. Kalish, U. F. D'Haenens-Johansson, M. Newton, F. Jelezko, and J. Wrachtrup, "Increasing the coherence time of single electron spins in diamond by high temperature annealing," *Applied Physics Letters*, vol. 97, no. 24, 2010.

[114] J. Koike, D. Parkin, and T. Mitchell, "Displacement threshold energy

for type iia diamond," *Applied physics letters*, vol. 60, no. 12, pp. 1450–1452, 1992.

[115] D. M. Toyli, C. D. Weis, G. D. Fuchs, T. Schenkel, and D. D. Awschalom, "Chip-scale nanofabrication of single spins and spin arrays in diamond," *Nano letters*, vol. 10, no. 8, pp. 3168–3172, 2010.

[116] S. Sangtawesin, T. Brundage, Z. Atkins, and J. R. Petta, "Highly tunable formation of nitrogen-vacancy centers via ion implantation," *Applied Physics Letters*, vol. 105, no. 6, 2014.

[117] A. D. Elliott, "Confocal microscopy: principles and modern practices," *Current protocols in cytometry*, vol. 92, no. 1, p. e68, 2020.

[118] C. Nayek, K. Manna, A. Imam, A. Alqasrawi, and I. Obaidat, "Size-dependent magnetic anisotropy of peg coated fe3o4nanoparticles; comparing two magnetization methods," in *IOP Conference Series: Materials Science and Engineering*, vol. 305, p. 012012, IOP Publishing, 2018.

[119] I. Abu-Aljarayesh, A. Al-Bayrakdar, and S. Mahmood, "The effect of heating on the magnetic properties of fe3o4 fine particles," *Journal of magnetism and magnetic materials*, vol. 123, no. 3, pp. 267–272, 1993.

[120] D. C. Jiles, *Introduction to the electronic properties of materials*. CRC Press, 2017.

[121] R. M. Corless, G. H. Gonnet, D. E. Hare, D. J. Jeffrey, and D. E. Knuth, "On the lambert w function," *Advances in Computational mathematics*, vol. 5, pp. 329–359, 1996.

[122] R. W. de Gille, J. M. McCoey, L. T. Hall, J.-P. Tetienne, E. P. Malkemper, D. A. Keays, L. C. Hollenberg, and D. A. Simpson, "Quantum magnetic imaging of iron organelles within the pigeon cochlea," *Proceedings of the National Academy of Sciences*, vol. 118, no. 47, p. e2112749118, 2021.

Publication List

Journals

1. **T. Gas-osoth**, K. Hayashi, D. Prananto, and T. An, *Magnetic Noise Detection and Imaging from a Superparamagnetic Core-Shell Particle via an Ensemble of Nitrogen-Vacancy Centers in a Thin Diamond Chip*, ***APEX***, vol. 18, no. 2, 2025.

2. R. Kumar,**T. Gas-osoth**, I. Fescenko, A. Erickson, S. Lamichhane, T. Delord, T. Li, N. Raghavan, C. Cress, N. Proscia, S. W. LaGasse, S. H. Liou, X. Hong, T. An, J. F. Vega, C. M. Meriles, and A. Laraoui, *Nitrogen-Vacancy Magnetometry of Weak Ferromagnetism in WS_2 Flakes*, ***Small***, (under peer review).

Conference

Poster presentations

1. **T. Gas-osoth**, K. Hayashi, D. Prananto, and T. An, *Relaxometry Imaging of Conducting Magnetite Layers on a Core-Shell Superparamagnetic Particle Using Ensemble Nitrogen-Vacancy in Diamond* The 85^{th} JSAP Autumn Meeting 2024, TOKI MESSE and adjoining facilities, JAPAN, Sep 16, 2024.

2. **T. Gas-osoth**, K. Hayashi, D. Prananto, and T. An, *Double Electron-Electron Resonance Spectroscopy by Using a Scanning Nitrogen-Vacancy Center Diamond Probe* 2024 International Symposium on Nano-Materials for Novel Devices (JAIST-NMND2023), Kanazawa Chamber of Commerce and Industry Hall, Kanazawa, JAPAN, Jan 12, 2024.

3. **T. Gas-osoth**, T. Kageyama, K. Hayashi, D. Prananto, and T. An, *Observation of Single NV Center on An Electronic Grade Diamond*. 2022 JAIST International Symposium of Nanomaterials and Devices Research Area, KS Lecture Hall, JAIST, Ishikawa, JAPAN, Dec 14, 2022.

Oral presentations

1. **T. Gas-osoth**, Y. Wang, S. Lamichhane, R. Kumar, T. Li, T. Delord, C. D. Cress, J. F. Vega, X. Hong, T. An, C. A. Meriles, and A. Laraoui, *Widefield Nitrogen-Vacancy Magnetometry of Pristine and Fe-Implanted WS_2*, The 71^{st} JSAP Spring Meeting 2024, Setagaya Campus, Tokyo City University, JAPAN, Mar 19, 2024.

2. A. Laraoui, **T. Gas-osoth**, Y. Wang, R. Kumar, T. Delord, A. Erickson, T. Li, C. D. Cress, J. F. Vega, X. Hong, T. An, C. A. Meriles, S. Lamichhane, and S. H. Liou, *Ferromagnetism and Magnetic Edge Effects in Fe-Implanted WS_2 Layers*, The American Physical Society's March Meeting 2024, Minneapolis & Virtual, Minnesota, USA, Mar 4, 2024.